Development of Trajectory-Based Techniques for the Stereotactic Volumetric Modulated Arc Therapy of Cranial Lesions

by

Byron Wilson

BSc Physics, University of Toronto, 2013

A THESIS SUBMITTED IN PARTIAL FULFILLMENT
OF THE REQUIREMENTS FOR THE DEGREE OF

Doctor of Philosophy

in

THE FACULTY OF GRADUATE AND POSTDOCTORAL STUDIES
(Physics)

The University of British Columbia
(Vancouver)

December 2018

The following individuals certify that they have read, and recommend to the Faculty of Graduate and Postdoctoral Studies for acceptance, the dissertation entitled:

Development of Trajectory-Based Techniques for the Stereotactic Volumetric Modulated Arc Therapy of Cranial Lesions

submitted by Byron Wilson in partial fulfillment of the requirements for

the degree of Doctor of Philosophy

in Physics

Examining Committee:

Ermias Gete, Senior Medical Physicist, BC Cancer
Supervisor

Stefan Reinsberg, Physics
Supervisory Committee Member

Cheryl Duzenli, Physics
Supervisory Committee Member

Arman Rahmim, Radiology
University Examiner

Septimiu Salcudean, Biomedical Engineering
University Examiner

Additional Supervisory Committee Members:

Vesna Sossi, Physics
Supervisory Committee Member

Supervisory Committee Member

Abstract

Introduction: Stereotactic Radiosurgery is the delivery of a large, highly focused radiation dose to well defined targets. This thesis explores linac-based inverse planning algorithms that can be implemented to improve the dosimetric and delivery performance of volumetric modulated arc therapy treatments for these indications.

Methods: In this work, algorithms for couch-gantry and collimator-gantry trajectory optimization were developed. Treatment plans calculated with these algorithms were compared dosimetrically to conventional methods used for treatment planning. Additionally, the clinical feasibility of the methods developed were tested by performing end-to-end patient-specific quality assurance on prospective treatments and by developing machine specific quality assurance for the intra-treatment movement of the couch and collimator.

Results: This thesis introduces a robust method for optimizing the trajectory of the couch by delivering treatments along patient generalized trajectories. These treatments were able to dosimetrically outperform dynamic conformal arcs, and had higher delivery efficiency than multi-arc volumetric modulated arc therapy. Similarly, collimator trajectory optimization was shown to reduce the dose bath when compared with the clinical standard of care. These methods were shown to be safe for delivery using phantom verification studies.

Conclusion: This thesis outlines methods for stereotactic radiosurgery which show dosimetric improvement over previous methodology and are clinically feasible.

Lay Summary

Linear accelerators are used to irradiate cancerous tissue in the brain with the hope of slowing or removing the disease. During radiation treatments, the radiation has to travel through healthy tissue before it can effect the tumours which can be deep seated within the brain. This work tries to mitigate the exposure of healthy brain tissue to unnecessarily high levels of radiation by exploring two methods. The first method optimizes the angles of entrance with the hope of avoiding sensitive healthy tissue. The second method explores optimizing the rotation of the radiation field shaping device so that the radiation beam can conform to the tumour as much as possible. The methods developed were shown to reduce the amount of radiation to the healthy brain tissue while decreasing the delivery time and maintaining the delivery accuracy.

Preface

A version of Chapter 2 has been published in the journal Medical Physics and is being republished with permission from Wiley. The original publication can be found here:

- Wilson B, Otto K, Gete E. A simple and robust trajectory-based stereotactic radiosurgery treatment. Medical physics. 2017 Jan 1;44(1):240-8.

I am the first and corresponding author of this research. I completed this research under the supervision of Ermias Gete, who provided research guidance, assistance in the measurements, and clinical expertise. Karl Otto provided technical support of the codebase which underlies the Varian Eclipse Treatment planning system. This work was featured in:

- Ian Randall, TVMAT enhances stereotactic radiosurgery. Medical Physics Web, 2017 Jan 24; http://medicalphysicsweb.org/cws/article/research/67593

Additionally, a version of Chapter 3 has also been published in the journal Medical Physics and is being republished with permission from Wiley. The original publication can be found here:

- Wilson B, Gete E. Machine specific quality assurance procedure for stereotactic treatments with dynamic couch rotations. Medical Physics. 2017 Dec 1;44(12):6529-37.

I am the first and corresponding author of this research. I completed this research under the supervision of Ermias Gete, who provided research guidance, designed the phantom, assisted in the measurements, and co-developed the mathematical analysis.

Chapter 4 has not yet been published. The work represented in it was completed by myself under the supervision of Ermias Gete. I conducted the numerical simulations and developed the mathematical models. Gete provided clinical expertise which guided the project and assisted in the linac measurements.

Table of Contents

List of Tables

List of Figures

Glossary

AAA anisotropic analytical algorithm

AAPM American Association of Physicists in Medicine

AN accoustic neuroma

ASTRO American Society for Therapeutic Radiation Oncology

BB ball bearing

CI conformity index

CP control point

CT computed tomography

CTV clinical target volume

DAO direct aperture optimization

DCA dynamic conformal arc

DICOM digital imaging and communications in medicine

DR dose rate

DVH dose volume histogram

EBRT external beam radiation therapy

EPID electronic portal imaging device

FMEA failure mode and effects analysis

FFF flattening filter free

FO fall off

GTV gross tumour volume

HI homogeneity index

ICRU International Commission on Radiation Units and Measurement

IMAT intensity modulated arc therapy

IMRT intensity modulated radiation therapy

linac linear accelerator

MC Monte Carlo

MLC multi-leaf collimator

MRI magnetic resonance imaging

MU monitor unit

OAR organ at risk

OD optical density

PBC pencil beam convolution

PCA principal component analysis

PDD percent depth dose

PET positron emission tomography

PTV planning target volume

QA quality assurance

QC quality control

QUANTEC Quantitative Analyses of Normal Tissue Effects in the Clinic

RTOG Radiation Therapy Oncology Group

SBRT stereotactic body radiotherapy

SPECT single photon emission computed tomography

SRS stereotactic radiosurgery

SSD source skin distance

TVMAT trajectory volumetric modulated arc therapy : VMAT which incorporates trajectories formed by dynamic movements of the couch

VMAT volumetric modulated arc therapy

WBRT whole brain radiotherapy

Acknowledgements

I would like to first and foremost thank my supervisor, Ermias Gete, for his continuous support throughout this project. For every stage of this degree, he went above and beyond the expectations of a supervisor and in doing so, has become a valued friend and collaborator. In this last half-decade, he has helped me work through my weaknesses and taught me many things about medicine and radiation therapy. I hope to one day be as great a teacher and role model as he has been to me.

I would like to thank my family for their love and for talking me through many existential crisis's that I encountered while I completed this degree. I would also like to thank the friends that I have made in BC and for the many sketch-ball mountain adventures we have shared.

I would also like to thank Cheryl Duzenli for cajoling money from the BC Cancer agency for this project. Her relentless support of medical physics research and for the training of the next generation of medical physicists is one of the many things which make the Vancouver medical physics program world class. She has saved many lives, not only through her own actions, but by enabling and inspiring those around her.

Chapter 1

Introduction

Brain metastases (a secondary malignant growth) affect up to one-third of patients with cancer [77]. A viable treatment strategy for brain metastasis is stereotactic radiosurgery (SRS) [4] which is the delivery of high intensity, focussed radiation to targets within the brain. However, in radiotherapy, the radiation needs to travel through healthy tissue before it can deposit energy in the cancerous tissue. This creates a challenging optimization problem: creating treatments which minimize the radiation exposure of normal tissue while delivering a sufficient amount of radiation to control the disease. This thesis focuses on improving SRS treatments of brain metastasis.

As linear accelerators (linacs) are the most accessible SRS delivery devices used worldwide, this thesis focuses on linac-based SRS treatments. The introduction will give the reader an overview of photon-based radiotherapy, the physics which underpin dose deposition and measurement, biological considerations when treatment planning, and the optimization methods that are used to create linac-based SRS treatments. Section 1.1 to Section 1.4 (inclusive) provide the reader with background knowledge of medical physics and can likely be skipped by readers with a background in radiation therapy. Section 1.6 provides the reader with a quick introduction to optimization in radiotherapy, and puts the body of this work into context with previous SRS optimization research. This thesis presents optimization techniques that increase the dosimetric quality and delivery efficiency of linac based SRS treatments. An overview of the work presented in this thesis is

given at the end of this introduction (Section 1.7), after the relevant background concepts have been introduced.

1.1 Radiotherapy

Radiotherapy is the delivery of ionizing radiation to tissue with the goal of killing the diseased subunits of the tissue. The cells within the tissue become diseased by accumulating mutations in their deoxyribonucleic acid (DNA) code which affect their biological function (see [34, 35] for a comprehensive review on cancer). Radiation kills cells by causing irreparable DNA damage [66]. The main predictor on the amount of DNA damage to tissue recieving ionizing radiation is the mean energy absorbed by the medium per unit mass. This quantity is measured in joules per kg (unit Gray), which for its significance in treatment outcomes in radiotherapy, is also referred to simply as ”dose”.

In photon-based external beam radiation therapy (EBRT), radiation dose is delivered by directing a beam of high energy photons at the treatment site. These photons have typical energies of 4 MeV to 18 MeV [3]. They are delivered with a linac which produces a focused beam of high energy photons which are directed at the target from multiple directions. The control of a medical linac to produce the desired dose distribution in a patient is a complex problem: there are multiple entrance angles, intensities, and beam apertures which affect the optimization of the delivery sequence. Furthermore, there are many considerations which need to be accounted for, such as machine performance, physical dose deposition and radio-biological effects.

1.2 Radiotherapy Physics

The photons used in radiotherapy do not deliver dose directly, but instead impart their energy to electrons which subsequently deposit their energy in the tissue, causing DNA damage. There are four modes of photon interactions in the energy range used in radiotherapy. These are: coherent scattering, Compton scattering [20], photoelectric effect, and pair/triplet production.

1.2.1 Interaction of Photons with Matter

As a photon of a particular energy moves through matter, there is a constant probability of the photon interacting for a given path length. If there are N photons travelling in a medium, then the number of particles that are removed from the primary beam as they travel through the medium is given by:

$$\Delta N = -\mu N \Delta x \tag{1.1}$$

where μ is the linear attenuation coefficient, N is the number of photons in the beam, ΔN is the change in the number of photons in the beam, and Δx is the path length. Letting Δx tend to the infinitesimal path length dx and solving this equation by the method of separation of variables yields:

$$N = N_0 e^{-\mu x} \tag{1.2}$$

where N is the number of photons that has passed through an absorber of thickness x without interacting. This equation models the intensity of the primary beam as it travels through a medium. As can be seen, it has the form of an exponential decay.

The linear attenuation coefficient μ is dependent on the photon energy and the medium type and density. It can be calculated by summing over the linear attenuation coefficients for each individual interaction type:

$$\mu = \sigma_{coh} + \sigma_{inc} + \tau + \kappa \tag{1.3}$$

where the respective attenuation coefficients from different types of interactions are σ_{coh} (coherent scattering), σ_{inc} (compton scattering), τ (photoelectric effect), and κ (pair or triplet production).

The mass attenuation coefficient ($\frac{\mu}{\rho}$) is defined as the ratio of the linear attenuation coefficient to the mass density of the medium. It is more commonly presented in data tables and plots as it removes the density dependence from the tabulated data. Mass attenuation coefficients for two of the most common biological materials (water and bone) are shown in Figure 1.1.

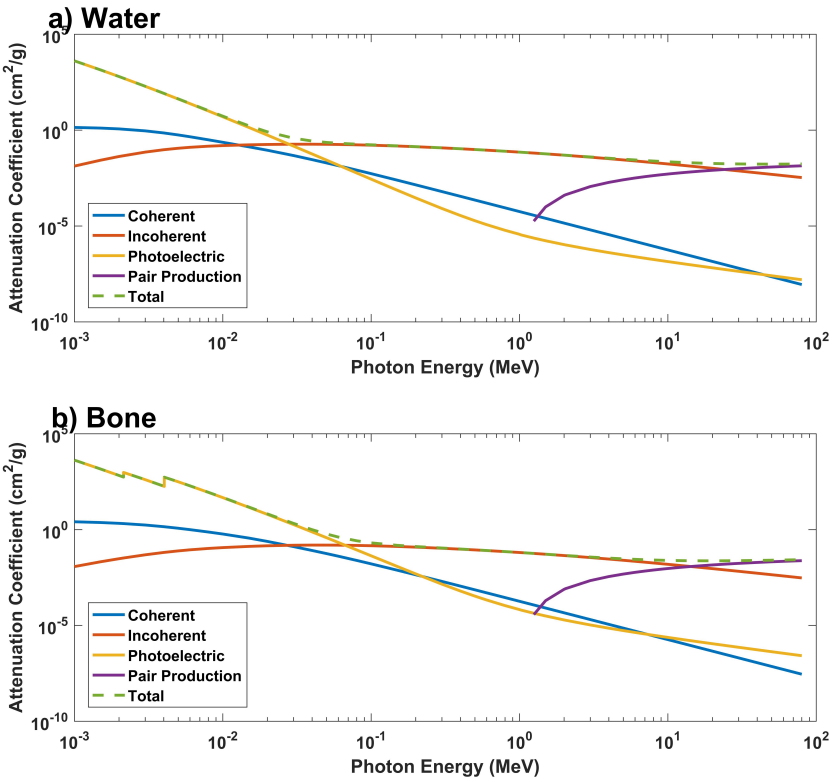

Figure 1.1: A plot of photon attenuation coeficients for water and bone. a) The attenuation coeficients of photons in water (shown here) has very similiar properties to human tissue. At low energies ($<$ 100 keV), the photoelectric effect is dominant, at intermediate energies (1-10 MeV), Compton scattering is dominant, and at high energies ($>$ 10 MeV), pair production is dominant. b) The attenuation coeficients of photons in bone. At low energies the photoelectric effect is much stronger due to the higher effective atomic number of bone. This phenomenon is responsible for the contrast of x-ray scans. At higher energies, Compton and pair production dominate, which depend less on the Z of the material. Therefore dose calculations at these energies under the assumption of water equivalence are more accurate. Data for figures (a) and (b) were collected from The National Institute of Standards and Technology database [10, 70]

Coherent Scattering

Coherent scattering is the elastic scattering of photons with molecules (Rayleigh) or the elastic scattering of photons with electrons (Thomson). Neither of these processes impart any energy to the medium, but instead change the direction of the photon. As can be seen in Figure 1.1, coherent scattering is not a dominant mode of interaction at the energies and in the materials of interest in radiotherapy physics.

Incoherent Scattering

Incoherent scattering, or Compton scattering, is when a photon inelastically collides with a valence electron. The photon imparts some of its energy to the electron and is scattered at an angle. The energy of the scattered photon can be calculated using conservation of energy and momentum and depends on the scattering angle:

$$E'_\gamma = \frac{E_\gamma}{1 + (E_\gamma / m_e c^2)(1 - cos\theta)} \tag{1.4}$$

where E_γ is the energy of the incoming photon, E'_γ is the energy of the photon after the interaction, m_e is the mass of an electron, c is the speed of light constant, and θ is the scattering angle of the photon. The rest of the energy is imparted to the electron as kinetic energy:

$$KE'_e = E_\gamma - E'_\gamma - E_{binding} \tag{1.5}$$

where KE'_e is the kinetic energy of the scattered electron, and $E_{binding}$ is the binding energy of the electron to the atom. The probability of interaction for a given solid angle is given by the Klein-Nishina [49] cross section which has the form:

$$\frac{d\sigma}{d\Omega} = \alpha^2 r_c^2 \frac{\lambda^2}{\lambda'^2} [\frac{\lambda}{\lambda'} + \frac{\lambda'}{\lambda} - \sin^2(\theta)]/2 \tag{1.6}$$

where α is the fine structure constant, r_c is the reduced Compton wavelength of the electron, λ is the wavelength of the incoming photon and λ' is the wavelength of the photon after the interaction. This equation dictates that when the incident photons have high energy, most of the outgoing photons and electrons will be forward directed.

Photoelectric Effect

The Photoelectric effect is the interaction of a photon with an atom which results in the ejection of a bound electron from the atom. This electron absorbs the entire energy of the incoming photon:

$$KE'_e = E_\gamma - E_{binding} \tag{1.7}$$

where $E_{binding}$ is the energy required to eject the electron from the nucleus, and KE'_e is the kinetic energy of the scattered electron after the interaction. The photoelectric cross section depends on the energy of the incident photon and the atomic number of the material. It peaks at energies which are in resonance with the binding energies of the electrons and has a general trend which decreases as E_γ^{-3}. Additionally it is highly dependent on the atomic number (Z) of the materials with a general trend of $Z^{3.8}$.

Pair and Triplet Production

Pair production is a process in which the photon interacts with an atom creating an electron-positron pair. The photon is completely absorbed and the kinetic energy is shared between the outgoing electron and positron:

$$E_\gamma - 2m_e c^2 = KE_+ + KE_- \tag{1.8}$$

where $m_e c^2$ is the rest energy of an electron and KE_+,KE_- are the kinetic energies of the positron and electron respectively. For a photon to undergo interaction through pair production, it must have a minimum energy of $2m_e c^2$, the energy required to produce the electron positron pair. Beyond the threshold energy, the cross section increases rapidly and it is the dominant cross section for high energies. The cross section also depends linearly on the atomic number of the medium of interaction.

1.2.2 Linear Accelerators

Linac's are the most common treatment device for EBRT worldwide [91]. The most common medical linac is the C-arm linac (an example of which is shown in

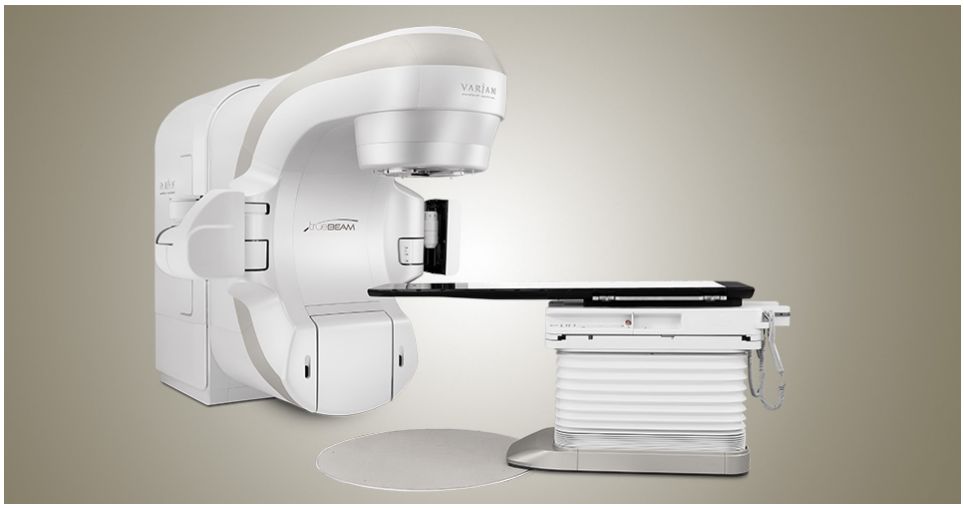

Figure 1.2: A linac with the gantry in the vertical position and treatment couch (the black carbon-fibre board) is rotated from its home position which is in-line with the gantry. Photons are produced in the gantry and are used to irradiate the patient who usually lies on the couch. The gantry can be rotated $\pm$ 180 degrees while the couch can be rotated $\pm$ 90 degrees provided that collisions are avoided. Image courtesy of Varian Medical Systems, Inc. All rights reserved.

Figure 1.2). linacs generate a pencil beam of high energy electrons by accelerating the electrons in a microwave cavity. Depending on the length of the microwave cavity, the microwave cavity can be placed in-line or at a (typically) 90 degree angle with the final beam. If mechanical considerations do not allow the microwave cavity to be in-line with the beam, then the electrons are steered using a bending magnet. The electrons are then directed to either a scattering foil to create a broad electron beam or to a tungsten target to create photons via bremsstrahlung. Modern medical linacs typically can produce electrons in a range 4 MeV to 20 MeV. However, the majority of EBRT treatments are based on photon beams. Photons are produced by placing a target in front of the electron beam line. Inside the target, photons are produced from bremsstrahlung radiation, the production of photons from the slowing down of the electrons as they travel through a medium. The spectral distribution of photons produced by monoenergetic electrons hitting a target is

given by Kramer's Law:

$$I(\lambda) = K(\frac{\lambda}{\lambda_{min}} - 1)\frac{1}{\lambda^2} \tag{1.9}$$

where I is the irradiance at a wavelength λ, K is a constant, and λ_{min} is the minimum wavelength possible when all of the kinetic energy of the electron is transformed into a single photon. The actual spectrum that is produced by this interaction deviates from the above formula, as low energy photons are preferentially absorbed by the target and characteristic radiation is preferentially produced by the target.

Linac Beam Collimation

A schematic diagram of a typical linac head is shown in Figure 1.3. High energy electrons from the microwave cavity are allowed to strike a tungsten target to produce photons. These photons are collimated by the primary collimator so that only the photons emitted in the desired direction leave the linac assembly. The photons are then attenuated by the flattening filter, whose function is to optimize the fluence of the beam so that it produces a boxcar function shaped lateral dose profile at 10 cm depth. In modern treatments where a variable aperture collimator can be used to modulate the intensity of the beam, the flattening filter may be removed for achieving higher dose rates.

Beam fluences are monitored by the dual-ionization chamber which is located below the flattening filter. The beam then enters the secondary-tertiary collimator assembly which can be rotated around the central beam axis to provide an extra degree of freedom. The secondary collimator is comprised of the x-jaw and y-jaws which define the rectangular edge of the photon beam. The x-jaws and y-jaws are matched with the divergence of the beam and are sufficiently thick so that the beam is practically confined to the opening of the jaws (attenuation of 99.98% for modern Varian linacs). Next, the photons enter the MLC (a form of tertiary collimator) which is placed perpendicular to the axis of the beam and is comprised of 5 - 7.5 cm thick tungsten blocks which attenuates approximately 98-99% of the beam (depending on the MLC model)[19]. The MLC leaves are typically between 2.5 mm wide to 10 mm wide when their shape is projected to the isocentre correcting for divergence of the beam. The Varian HD120 MLC used in this dissertation has

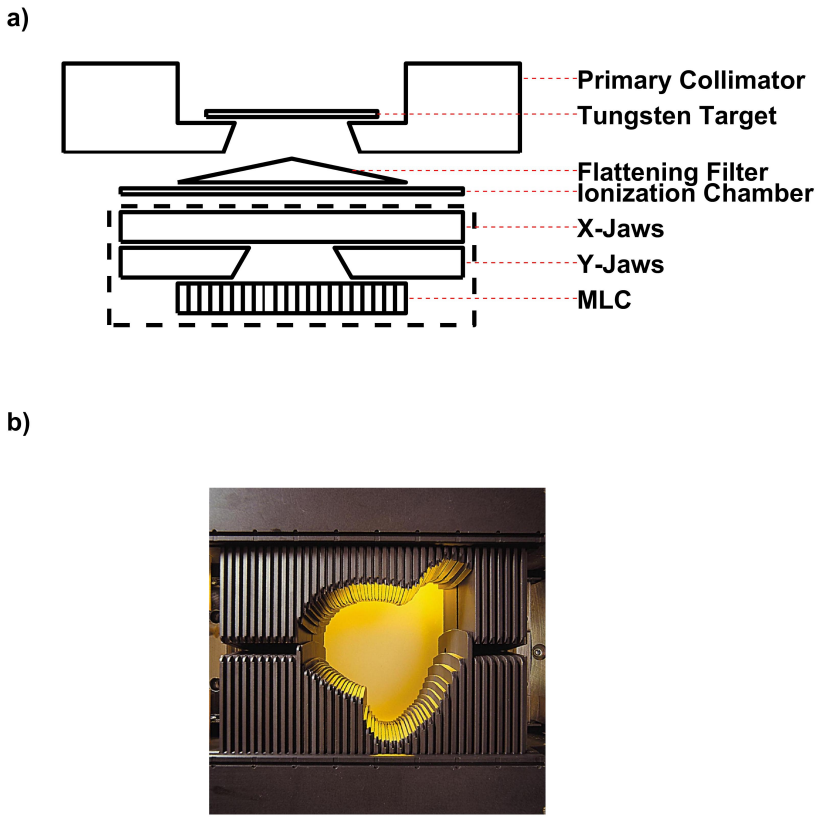

Figure 1.3: a) Cross sectional schematic diagram of a typical linac head. The secondary collimator and MLC illustrated with a dashed box, is attached to a sliding ring which allows it to be rotated with respect to the central axis of the beam. Diagram not to scale. b)External view of the multi-leaf collimator (MLC). The MLC can form customized beam apertures by retracting or extending the individual leaf components. Image courtesy of Varian Medical Systems, Inc. All rights reserved.

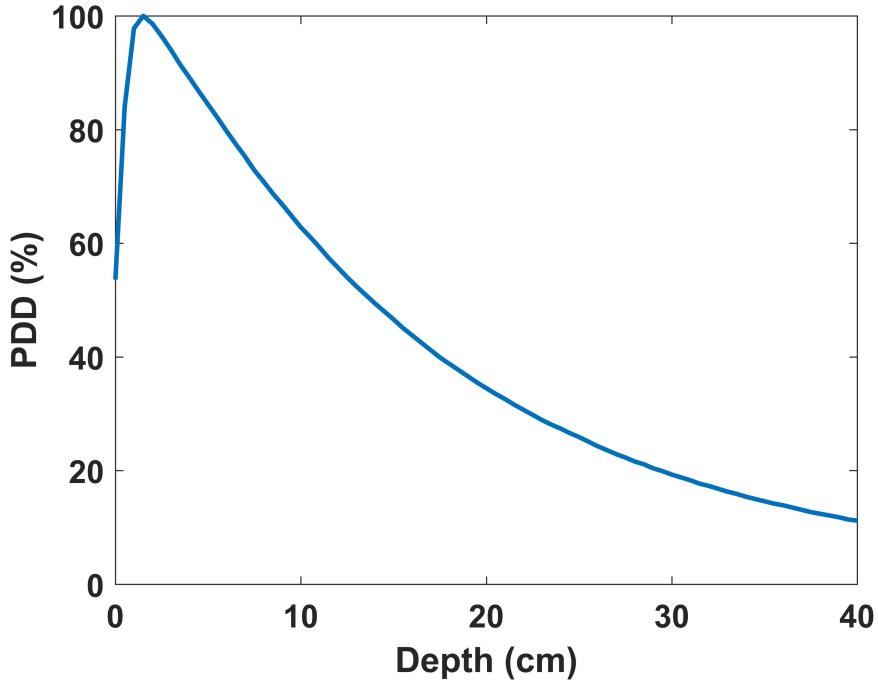

Figure 1.4: The PDD curve of a 6MV, 10x10 cm^2 photon beam measured in a water phantom placed 100 cm from the source. The PDD is normalized to 100 at the depth of max dose d_{max} along the central axis.

64 central leaves (32 leaf pairs) of 2.5 mm width, and 56 outer leaves (28 leaf pairs) of 5 mm width. It can rotate at 15 degrees/second and can linearly move each leaf at a max speed between 2.5-5 cm/second [64].

Linac Beam Characteristics

The human body is very similar in density and composition to water. This makes water the medium of choice for dosimetric measurements. The dose profile of the central axis of a 6 MV 10x10 cm^2 photon beam in water is shown in Figure 1.4. As can be seen in the figure, the dose builds to its maximum at a fairly shallow depth (around 1.5 cm depth). Tumours can be seated close to the surface, but are frequently at a deeper depth (5-30cm). In the majority of radiotherapy treatment situations, a single radiation field will deliver more dose to normal tissue than to

the diseased site since most tumours are located at a depth deeper than the depth of maximum dose. It is only by summing the dose contribution from multiple fields that the tumour is made to receive a larger dose than the surrounding tissue. This results in viable control of the disease while reducing the normal tissue toxicities. However, each beam by itself typically delivers more dose to healthy tissue than to diseased tissue, which contribute to a low dose bath to the surrounding tissue.

In addition to attenuation of the beam, there is also lateral scatter of the beam which spreads the dose beyond the photon beam field edge. This is caused by two processes:

1. The lateral scatter of the photons.

2. Multiple scatter of the secondary electrons.

These factors produce a beam which is spread out in the lateral directions. Profiles produced by a 6 MV 10x10 cm^2 photon beam are shown in Figure 1.5

1.2.3 Monte Carlo Simulation

In Monte Carlo (MC) simulations [80], the transport of photons are simulated by sampling from stochastic distributions which underlie the interactions of particles in matter. The dose deposited by these photons is calculated by simulating large numbers of these interactions. Using this method dose distributions can be calculated on a patient-to-patient basis. MC simulations can also be used to calculate the dose deposition of a pencil beam of photons (the simulation of a small beam of photons incident on a medium). This can be used to approximate the dose from an arbitrary linac aperture using mathematical methods discussed in the next section. Figure 1.6 shows a typical dose deposition pencil beam kernel from a 6 MV beam calculated using a MC simulation.

Pencil Beam Convolution

The pencil beam convolution (PBC) algorithm is a model-based method for finding the dose from photon beams. It works by summing the dose contribution from

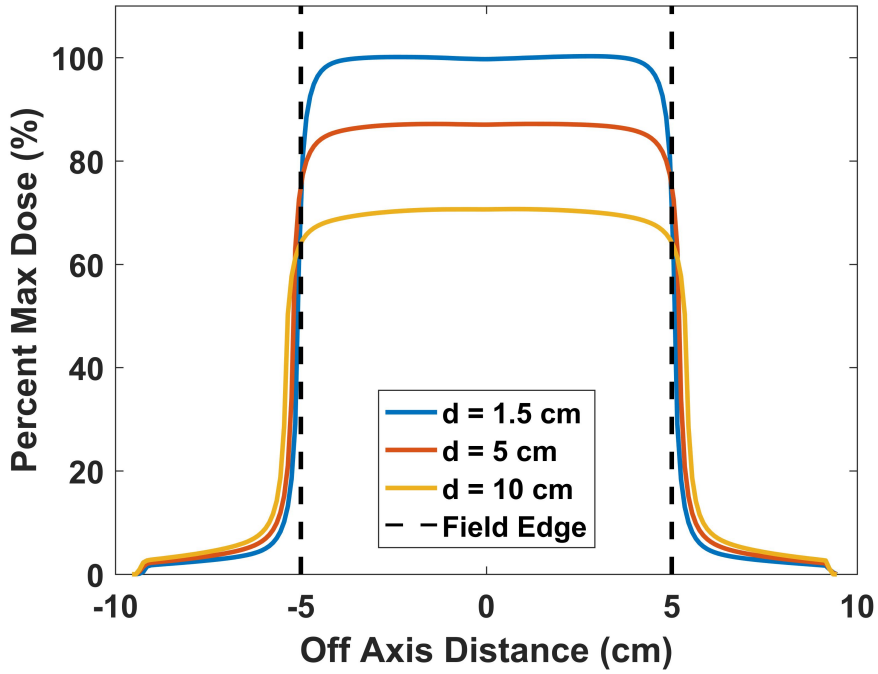

Figure 1.5: Beam profiles for a 6MV 10x10 cm^2 photon beam. The blue, red and orange lines correspond to the cross axis beam profiles at depths (d) 1.5, 5 and 10 cm respectively. The dotted line represents the geometric field edge defined at the isocentre by the secondary collimator.

smaller subsets of the beam. This is accomplished using the following equation:

$$D(x,y,d) = \frac{(SSD+d_{ref})^2}{(SSD+d)^2} \int\int F(x',y')K(x-x',y-y',d)dx'dy' \tag{1.10}$$

where source skin distance (SSD) is the distance from the target to the patient skin, d_{ref} is a reference depth used in the calculation of the kernel and intensity, F is fluence of the beam (the number of particles passing through a unit area perpendicular to the beam line), and K is the dose deposition kernel (shown in Figure 1.6).

The first ratio, $\frac{(SSD+d_{ref})^2}{(SSD+d)^2}$, is known as the inverse square correction factor. It corrects for the falloff of the fluence as the radiation source is moved away from the dose calculation point. At typical treatment distances, the radiation can be

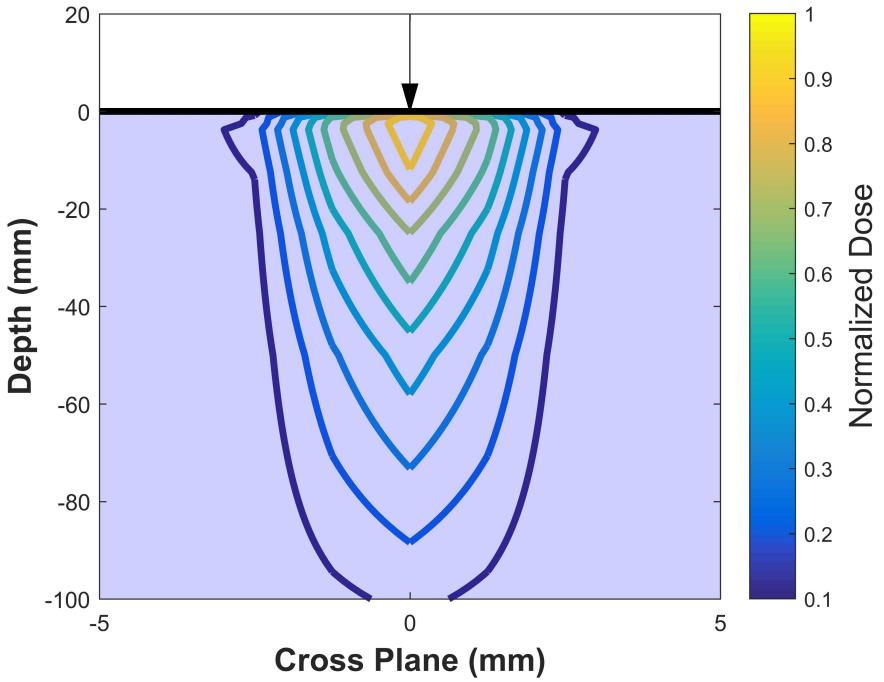

Figure 1.6: Level set diagram of the dose deposition kernel of a 6MV photon beam. Doses are normalized to the max dose delivered by the kernel. A pencil beam of photons (shown as a black arrow) incident on the water phantom (shown by blue shading) at (0,0). The photon interactions result in high energy electrons which subsequently deposit their energy in both the forward and lateral directions.

modelled diverging from a point-source with the particle fluence spread across a spherical surface area. This area depends on the square of the distance from the source, so the correction factor is a ratio of squared distances.

The second part of the equation (the integration) represents a convolution of the particle fluence with the dose deposition kernel. The particle fluence represents the number of particles per unit area in the beam cross section. Practically, this method relies on breaking the beam down into subsets. The name ”pencil beam” comes when the calculation grid size is on the order of mm, for which the linac beam is modelled as the sum of multiple pencil-sized beam subsets. The dose deposition kernel models the dose deposited by a each of these beam subsets.

Therefore total dose is the number of particles incident on an x-y coordinate in the beam crossplane (fluence) multiplied by the dose deposited by the beam subset and summed in aggregate.

As this equation takes the form of a convolution, it can be conducted in the fourier domain for faster calculations, and this forms the basis for time efficient treatment calculation algorithms [12, 33]. The computational efficiency of this method lends itself to iterative optimization problem solving methods which require many dose computations throughout the optimization process.

1.3 Treatment Planning

Treatment planning is the process by which a viable EBRT treatment is constructed. The first step in the process is to acquire a computed tomography (CT) scan of the patient. CT scans are 3D images produced by x-ray imaging a subject from multiple directions and then determining the 3D attenuation of the subject using mathematical methods. This provides anatomical information (as different tissues have different attenuation coefficients) for planning and dose calculations.

The International Commission on Radiation Units and Measurement (ICRU) defines standard ways of reporting doses recieved by tumour and normal tissue volumes [41, 67]. The organ at risk (OAR) and tumour target (called the gross tumour volume (GTV)) are contoured either from the CT images directly or on images from other modalities, such as magnetic resonance imaging (MRI), positron emission tomography (PET), single photon emission computed tomography (SPECT). Two margins are typically added to the GTV, the first of which is the clinical target volume (CTV) margin which accounts for microscopic spread of the tumour which cannot be visualized on the imaging scan. A second margin known as the planning target volume (PTV) margin is added to account for treatment uncertainties such as setup error and patient movement. The PTV margin will depend on the treatment site, the linacs mechanical accuracy, the accuracy of the patient immobilization, and positioning system. A typical GTV to PTV expansion for SRS brain metastasis is 1-3 mm [45].

1.3.1 organ at risk (OAR)

An organ is a group of tissues that perform a specific function. Toxicity refers to the disruption of the biological function of an organ in some way. The goal of treatment planning is to create a radiation delivery plan which manages the probability of normal tissue toxicity while still delivering enough dose to the diseased tissue to control the disease. The Radiation Therapy Oncology Group (RTOG) defines a toxicity rating quantified on a 5 point scale, with 0 being no symptoms, and 5 being death directly related to the radiation effect on the organ [32]. This toxicity rating system is the most commonly used system in North America.

The functional subunits within an organ can act with two types of architectures to achieve the overall function of the organ. The first is a serial architecture which requires each subunit of the organ to function for the entire organ to maintain its function. An example of a serial organ is the spinal cord, where if a single subunit of the spinal chord breaks, motor control for a sector of the body can be lost. The radiation dose to toxicity relationship for serial organs will depend on the maximum dose delivered to the organ because in these cases if one part of the organ is lost, the entire organ fails. The second architecture is a parallel organ where the organ is made up of subunits which each perform the same function. If one subunit fails, the others can still perform the function of the organ. For these architectures, the organ can tolerate large doses to a small subsets of the organ. The radiation dose to toxicity relationship sometimes depends on the mean dose received by the organ.

Not all organs fit into these two discrete categories, so a mathematical model is used:

$$gUED = (\frac{1}{N}\sum_{i=1}^{N} d_i^{\frac{1}{n}})^n \tag{1.11}$$

where $gUED$ is the generalized uniform equivalent dose, N is the number of voxels that make up an organ, d is the dose to a particular voxel, and n is a polynomial factor ($\in (0,1]$) which varies depending on whether the organ behaves in a serial or parallel fashion. When $n \to 1$, $gUED$ simplifies to the mean dose, and when $n \to 0$, the $gUED$ formula simplifies to the max dose formula. More information on biological modelling in radiotherapy can be found in a review by Marks et al.

Table 1.1: QUANTEC dose constraints for single fraction cranial SRS. V12 is the volume that recieves 12Gy and D_{max} is the max dose to an organ. Data collected from [9]

Critical Structure	Constraint	Toxicity Rate	Toxicity Endpoint
Brain	V12 <5-10 cc	<20%	Symptomatic necrosis
Brain stem (acoustic tumors)	$D_{max} < 12.5$ Gy	<5%	Neuropathy or necrosis
Optic nerve/chiasm	$D_{max} < 12$ Gy	<10%	Optic neuropathy
Spinal cord (single-fx)	$D_{max} < 13$ Gy	1%	Myelopathy

[61].

1.3.2 Quantitative Analyses of Normal Tissue Effects in the Clinic (QUANTEC)

While the discussion given in the previous section is important for understanding the basis for clinical practice (and therefore the basis for improvement), there are also guidelines set in place to assist and guide clinicians in evaluating radiotherapy treatment plans. These guidelines are mainly based on clinical outcomes data and are enumerated in a publication refered to as Quantitative Analyses of Normal Tissue Effects in the Clinic (QUANTEC)[9]. The small subset of these dosimetric constraints which are applicable for single fraction cranial SRS are shown in Table 1.1. As can be seen, one of the main considerations in SRS cranial treatment planning is to decrease V_{12Gy} of normal brain, the volume of brain that receives 12 Gy of radiation, which has been correlated with symptomatic radionecrosis.

1.3.3 Treatment Plan Evaluation

There are many quantitative methods by which radiotherapy treatment plans are analysed. Furthermore, there are different ways to represent the same information with little standardization. This can sometimes make the process of treatment plan evaluation difficult. This section will focus on the definition of the dose metrics which are used in this work.

Dose and Volume Statistics

One of the most commonly used metrics in treatment plan evaluation is the dose and volume statistics. As discussed in Section 1.3.1 and Section 1.3.2, sometimes the max dose delivered to a structure (D_{max}) or the mean dose delivered to a structure (D_{mean}) is correlated with organ function. Similarly, sometimes toxicity can be correlated with the volume that receive a certain amount of radiation. These volumes are represented with the notation V_x, which corresponds to the total volume which receives "x" radiation or more in Gray.

In SRS, the intention is to give the treated volume an ablative dose (a dose so high that it kills any tissue recieving the dose), so a treatment plan's effectiveness is measured by the degree to which the prescription dose overlaps and does not extend from the treated volume. This property is measured with the quantity known as the conformity index. There are several ways to calculate this metric, but here we will present Paddick's conformity index [73]:

$$CI = \frac{(T \cap V_P)^2}{T \times V_P} \tag{1.12}$$

where CI is the conformity index, T is the target volume (which can be the PTV or GTV depending on the application), $\cap$ is the geometric overlap function, and V_P is the volume that receives the prescription dose or more. Mathematically, the conformity index is bounded by 0 and 1. If the conformity index is equal to 1, then T aligns perfectly with V_P ($T \cap V_P = T = V_P$). The conformity index can be less than 1 for two types of deviations: either under-dosage of T (which would imply $\frac{T \cap V_P}{T} < 1$), or from dose spillage beyond the target volume (which would imply $\frac{T \cap V_P}{V_p} < 1$) .

Another metric used to evaluate treatment plans is the homogeneity index (HI), which measures the dose homogeneity across the PTV. While multiple different measures of homogeneity are used in radiotherapy [44], the formulation used in this thesis was:

$$HI = \frac{D_{max}^{PTV}}{D_{min}^{PTV}} \tag{1.13}$$

where D_{max}^{PTV} is the max dose to the PTV and D_{min}^{PTV} is the min dose to the PTV. Recent work has relaxed the goal of homogeneous treatment dose to the PTV in

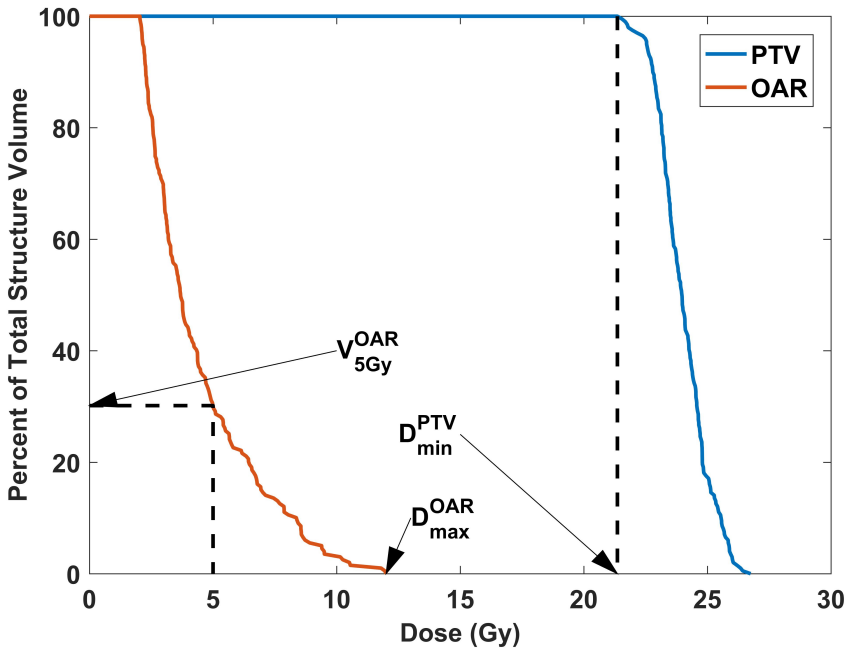

Figure 1.7: A typical dose volume histogram for an OAR and PTV is shown in red and blue respectively. Using this illustration, dose statistics can be read off the figure axes. A few examples such as V_{5Gy}^{OAR}, the volume of the OAR that receives 5 Gy ($\approx$ 30 %), D_{min}^{PTV}, the minimum dose of the PTV ($\approx$ 21 Gy), and D_{max}^{OAR} , the maximum dose of the OAR ($\approx$ 12 Gy) are shown on the plot.

favour of incorporating dose escalation to subsets of the PTV that are correlated to a higher probability of tumour recurrences [8].

dose volume histogram (DVH)

The DVH is a widely used tool for evaluating dose distributions. DVHs provide visual representations of the dose statistics. Figure 1.7 shows an illustration of a typical DVH for an OAR and PTV structure. The figure shows how dose volume statistics, such as V_{5Gy}^{OAR}, D_{max}^{OAR}, and D_{min}^{PTV}, are visualized. The DVH is versatile as multiple OAR, PTV, or normal tissues can be plotted and visualized at the same time (only two are shown in Figure 1.7 for simplicity). Additionally, a summary of

all tissues, sometimes referred to as the ”body” contour, can be plotted to show the dose received by the whole body.

1.4 Stereotactic Radiosurgery

Cranial SRS is the delivery of highly conformal ablative dose to small, well-defined targets in the brain. In recent years, linac-based SRS has gained increased relevance in the management of cranial lesions due to improvements in machine precision and delivery techniques that allow precise delivery of a highly conformal dose to the target. The high degree of dose conformity with SRS is achieved with either dynamic conformal arc (DCA) [87] (treatments where the MLC is set to the conform to the PTV and the beam line is rotated around the patient), volumetric modulated arc therapy (VMAT) [90] (treatments where the MLC, dose rate, and gantry rotation are optimized using mathematical methods and these aspects of the device move intra-treatment), or through static beams such as intensity modulated radiation therapy (IMRT) [25] (a treatment where multiple static beams with varying MLC apertures and dose rates are used to create viable treatments). Typically these treatments take between 7 minutes (single isocentre VMAT) to 40 minutes (IMRT). Treatment time mainly depends on how many couch positions are required, while treatment quality depends on how adequately the possible delivery entrance angles are sampled.

1.4.1 Small-Field Dosimetry

Small fields provide unique dosimetric challenges in radiotherapy. There are two main contributors to these challenges. The first of which is high dose gradients across the treatment field. Dosimetric measurements of small fields that exhibit high dose gradients require specialized detectors with a very small active volume so that readings do not suffer from the partial-volume effect (when readings are averaged over a volume with inhomogeneous dose distribution).

Secondly, lack of electronic equilibrium makes small field dosimetry challenging. Electronic equilibrium is achieved when the electrons leaving a detector’s active volume are balanced by the same number of electrons of the same kinetic energy entering the volume. However, near the edges of a field, the electrons that

are laterally scattered out of the field edge are not matched by electrons entering the active volume. Therefore lateral electronic equilibrium does not hold and corrections need to be applied for accurate dosimetry. This can be corrected for by using the appropriate correction factors [28] or by having a detector with a sufficiently small active volume when compared to the field size.

Considering these limitations, there are only a handful of measurement devices which are well suited under small field conditions. The two devices used in this thesis were small volume ionization chambers and radiochromic film. Film provides spatial dose information but are prone to introduced human error. Conversely ionization chambers provide accurate point doses, but are not that well suited for dose distributions. There are also numerous flat panel dosimeters which provide moderate spatial information (scale usually in mm to cm). This work relied upon an electronic portal imaging device (EPID) detector which is made out of amorphous silicon which can provide 2 mm spatial resolution and relative dose information.

Radiochromic Film

Radiochromic film refers to sheets of plastic-like material which is sensitive to radiation and changes colour and hence optical density (OD) when exposed to radiation. The OD is measured as the log ratio of the radiant flux transmitted by the material (I) divided by the radiant flux received by the material (I_0):

$$OD = log(\frac{I}{I_0}) \tag{1.14}$$

The OD-to-dose relationship is non-linear and different for each photon energy transmission measurement. Film is typically scanned with a modern flatbed scanner (for example, the Epson 10000XL was used in this study) which provides measurements of the absorbance of the film to red green and blue light.

Radiochromic film can be used as a form of relative dosimetry: the dose response curves cannot be derived from first principles and instead need to be approximated by measurements and non-parametric models. The process of calibrating the film involves measuring the dose response by exposing subsections of the film to known doses of radiation and measuring the optical density of the irradiated film with a flatbed scanner. The main sources of error which can be introduced with

dose measurement with film are:

1. Inconsistency between film batches.
2. Different optical properties depending on orientation of the light relative to the film.
3. OD depends on the time since irradiation.
4. The scanner has varying sensitivity scan-to-scan.
5. The scanner has varying sensitivity laterally intra-scan.

If these issues are mitigated, accurate dosimetry with radiochromic film is feasible. For example, the protocol suggested by Fuss et al. [29] quotes that a dosimetric accuracy of 1% [29] can be achieved. This thesis used GafChromic film (a commercial implementation of radiochromic film) using the protocols suggested in the manufacturer's white-paper [52].

1.4.2 Patient Immobilization

Due to the large, ablative doses delivered to small targets, SRS deliveries require small margins. In order to ensure accurate treatment within these small margins, patient immobilization and intra-treatment imaging are vital. Before intra-treatment imaging was available, patient immobilization was achieved using rigid frames in which an immobilization frame was screwed onto the patients skull by a neurosurgeon (as shown in Figure 1.8a). The rigid frame is attached pre-CT scanning and the patient is scanned with the localization box (shown in Figure 1.8b) fastened to the frame to provide fiducial markers for registration.

However, the use of rigid frames is time and resource intensive, and is uncomfortable for patients. Modern treatments use aquaplast moulding which is made of a plastic mesh, which when warmed can form to the patients anatomy and becomes rigid upon cooling. This technique when applied to SRS is known as frameless immobilization (shown in Figure 1.8c). However, by itself frameless immobilization does not have the same setup accuracy or reproducibility as the rigid frames because they are not attached to patient's bony structures. This is overcome by setting up the patient using image guidance and then aligning the patient to the

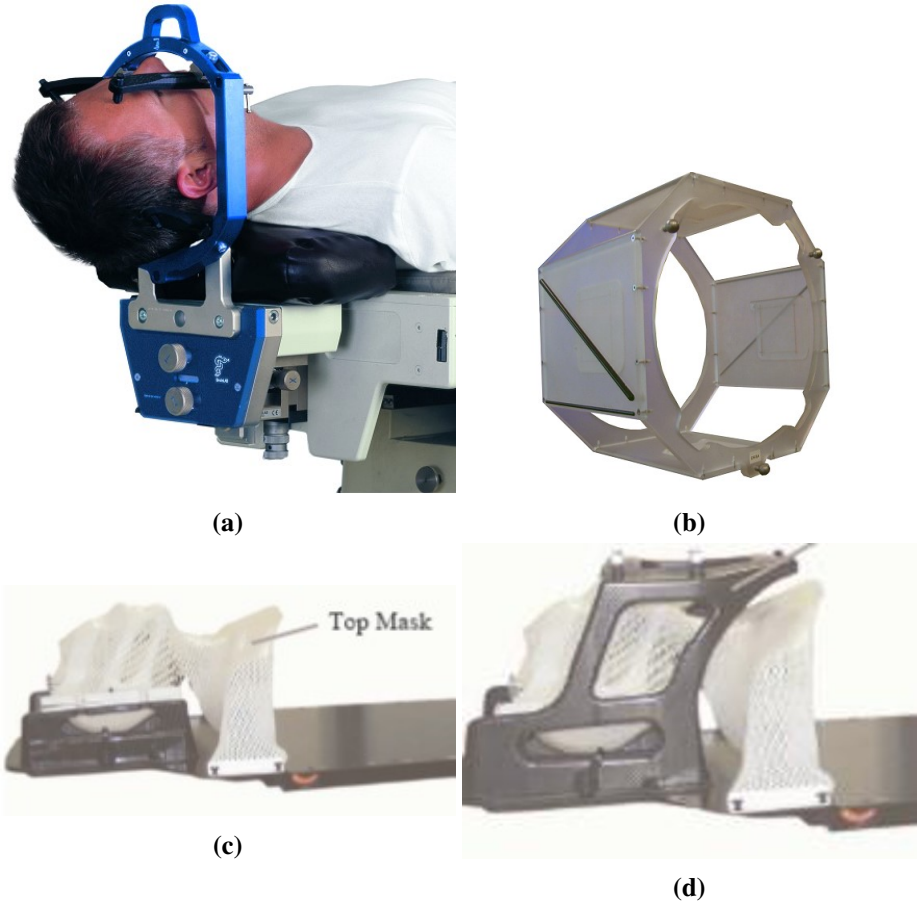

Figure 1.8: a) Rigid frame used for SRS deliveries. The frame is affixed directly to the skull. b) A positioning box is attached to the frame during imaging and patient set up. It provides fiducial markers and visual alignment markers to ease process of aligning CT information with the delivery isocentre. c-d) Brainlab frame-less mask used in modern day treatments.

treatment position with a motorized couch that can precisely move the patient in all six degrees of freedom of motion. Used properly, this technology can provide accuracy of less than 1 mm [79].

1.5 Quality Management in Radiation Therapy

A significant consideration in radiation therapy is how to ensure safe and consistent treatments on a patient to patient basis. Radiotherapy planning and delivery is a complex process and there are multiple points of failure that need to be managed to ensure treatment quality. For this reason, quality management is conducted throughout the radiotherapy planning and delivery process (termed end-to-end quality management). When changes are made to the planning process, methods need to be developed to combat the modes of failure which have been introduced.

The American Association of Physicists in Medicine (AAPM) has set guidelines for quality management in the radiotherapy setting. The AAPM report from task group 100 [39] (so called TG 100) provides an overview of the application of risk analysis methods to ensure treatment quality. It presents various methods such as failure mode and effects analysis (FMEA), which can be used to find modes of failure which may cause clinically significant events. Once identified, these modes of failure can be mitigated with quality management tools. TG 100 provides rank order lists of effective tools to use for these applications (listed in descending order of effectiveness):

1. Forcing functions and constraints (such as interlocks, berriers, computerized entry forms).

2. Automation and computerization (such as computerized verification, bar codes, automated monitoring).

3. Protocols, standards, and information (such as check-off forms, alarms, establishing protocols).

4. Independent double check systems and redundancies (such as redundant measurements, independent review, comparison with standards, acceptance testing).

5. Rules and policies (such as establishing a communication line, mandatory pauses, and establishing and performing quality control (QC) and quality assurance (QA) on hardware and software).

6. Education and information (such as training, experience and instruction).

The rank order of these methods provides guidelines for developing QA processes. While some aspects of QA occur closer to the bottom of this list (e.g. education and information) all methods are important in the management of radiotherapy quality. In particular, lower rank methods are implemented in situations where the higher order interventions are infeasible or impractical.

The AAPM report on Task Group 142 [48] (so called TG 142) set guidelines for the quality assurance of a linac. This document sets achievable lower limits on the accuracy of a linear accelerator for various types of treatments. An abridged summary of the mechanical specifications required for SRS VMAT and IMRT deliveries, and the recommended frequency of quality control is given in Table 1.2.

While TG 142 sets guidelines for the mechanical specifications, it does not make recommendations on how to test for these mechanical specifications. Furthermore, as expanded in TG 100, clinical processes are unique to each centre, and quality management should be tailored to the clinical processes which are implemented. A rough starting point for the quality management of VMAT treatments was presented by Ling et al. [54]. In this work, various methods are introduced for testing the aspects of the linac enumerated in Table 1.2. Some methods from this publication were expanded upon in this work so that the methods developed by Ling et al. could applied to treatments with intra-treatment motion of the couch and collimator.

1.5.1 The Picket Fence Test

The picket fence test was developed by Bayouth et al. [6] as a method for ensuring MLC performance for IMRT deliveries (although it is also applicable to VMAT deliveries [54]). In this method, the field jaws are opened and the MLC is set to create a 1 mm gap across a 2D dosimeter (film or EPID). This gap is moved across the film in 1.5 cm gaps, with the radiation field turned on when the MLC is static. The irradiation pattern on the 2D dosimeter looks like a picket fence and deviations in MLC can be identified using visual inspection or computer aided methods.

Yu et al. [101] expanded this method to ensure the synchrony of the couch and MLC. In this method, radiochromic film is placed on the treatment couch and a 1

Table 1.2: Summary of the mechanical specifications required for IMRT and VMAT deliveries with a linac. Data was collected from recommendations made by the AAPM task group 142 [48]

Quality Test	Accuracy
Daily	
X-ray output constancy	3 %
Laser Localization	1 mm
Distance indicator (ODI)	2 mm
Collimator size indicator	1 mm
Monthly	
Photon beam profile constancy	1 %
Light/radiation field coincidence (asymmetric)	1 mm or 1 % on a side
Jaw poosition indicators	1 mm
Dose Rate Constancy	2 %
Treatment couch position accuracy	1 mm translational, 0.5 degree rotation
Localization lasers	$<$1 mm
Gantry Collimator angle indicators	1 degree
Annual	
X-ray flatness change from baseline	1 %
X-ray symmetry change from baseline	$\pm$ 1 %
X-ray output calibration (TG-51)	$\pm$ 1 %
Spot checks for field size dependent output factors	2 % for field sizes $<$ 4x4 cm^2, 1 % $>$ 4x4 cm^2
X-ray beam quality	1 % from baseline
X-ray output constancy vs dose rate	$\pm$ 2 % from baseline
x-ray output constancy vs gantry angle	$\pm$ 1 % from baseline
Arc Mode (expected MU per degree)	$\pm$ 1 % from baseline
Collimator rotation isocenter	$\pm$ 1 % from baseline
Gantry rotation isocenter	$\pm$ 1 % from baseline
Couch rotation isocenter	$\pm$ 1 % from baseline
Coincidence of radiation and mechanical isocentre	$\pm$ 1 mm from baseline

mm gap is produced with the MLC. The gap is then scanned across the field while the couch moves concurrently at the same speed. Throughout the movement, the radiation field is turned on. This can be used to ensure the simultaneous movement of the couch and collimator.

1.5.2 Coincidence of the Treatment Isocentre

A medical linac is comprised of many mechanical subsets that act in synergy to deliver a treatment. Each degree of freedom is usually in spherical or cylindrical geometry with rotations about a single axis. This introduces two forms of error into the delivery process: misalignment and wobble of the isocentre. There have been various QA methods to measure the sources of error introduced by rotation of the couch, gantry and collimator.

Winston-Lutz Test

Mechanical accuracy of the isocentre rotation was a major hurtle for the use of a linac in SRS treatments. Lutz et al. [58] developed an accurate and robust system for measuring the relation of the radiation isocentre with the treatment position system. At the introduction of this technique (and when TG 142 was first authored) the laser localized isocentre was used as the treatment position system. Modern linacs use an on-board imaging defined isocentre, and the methods developed by [58] has been adapted to these techniques.

The method developed by Lutz et al. [58] is now commonly referred to as the ”Winston-Lutz Test”. It involves accurately aligning a ball bearing (BB) with the treatment isocentre, placing a 2D radiation measurement device under the BB, and then irradiating the phantom with a well defined small field. The location of the BB can be quantified as it is radio-opaque. The 2D dosimeter needs to have enough spatial resolution to quantify the location of the BB to less than a mm. Initially, film dosimetry was best suited for this purpose, but modern EPID also provide enough spatial resolution. From these images, the centre of the BB is found (treatment isocentre), which is compared to the centre of the radiation field, as defined by the centre point between the half max of the field edges. The Winston-Lutz test can be used to measure the mechanical accuracy of the couch, collimator, and gantry.

An up-to-date and more in-depth protocol for the Winston-Lutz test with a modern linac is provided by Rowshanfarzad et al. [82].

Starshot Method

While the Winston-Lutz test measures the interaction of the radiation isocentre with the respective errors of the mechanical degrees of freedom of the linac, the starshot method tests the mechanical error individually. In this method, the MLC (or sometimes the secondary collimator) is set to form a 1 mm gap along the central axis of the field. A 2D dosimeter (previously film, however the EPID can be used for the collimator measurement) is irradiated by the linac. Next the degree of freedom under study is rotated by 30 degrees, and the dosimeter is re-irradiated. This is consecutively conducted for 180 degrees of rotation (or 6 irradiations). Next a line fitting algorithm is used to fit the strips of irradiation (produced by the 1 mm collimated beam). The intersection point between each of the 6 lines is calculated and the size and centre of the largest circle encapsulating all of the points is reported. This provides a measurement of the true isocentre of rotation for the method under study. The centre of the circle or centre of mass of the intersection points can be compared to the treatment positioning system defined isocentre.

1.5.3 Patient Specific Quality Assurance

The QA of dose distributions presents a challenging problem: dose distributions present 3D data and there are many ways in which the expected dose can differ from the delivered dose. the goal of analysis is to find gross deviations from clinically acceptable treatment plans with one simple to calculate metric. There are two main deviations which can occur in radiotherapy: inaccuracy of dose (i.e. the dose is some percentage different than the expected value) and positioning inaccuracies (i.e. the dose distribution is misaligned). Positioning accuracy is very important as un-irradiated tumour tissue will significantly decrease the efficacy of the treatment. Similarly, dose inaccuracies can manifest unexpected toxicities for structures which are close to their limits, and lower the probability of disease-free survival if the tumour is under-dosed. Low et al. [57] developed a method that tries to explicitly account for these types of errors, and it is called the gamma pass met-

ric. In this method ideal accuracy specifications, such as the dose value accuracy and positioning accuracy, are specified. In the original publication, an accuracy of 3 %, 3mm in the dose value and position were used respectively. Modern SRS treatment QA uses 2%, 2 mm or 2 %, 1 mm as positional accuracy is of greater importance when tight margins are used.

Each dose value in the reference distribution is compared to the spatially close doses of the measured distribution (within δr mm of the point, where δr is the accuracy previously chosen). For each point, the gamma criterion is calculated as :

$$\Gamma = \sqrt{(\frac{\Delta r}{\delta r})^2 + (\frac{\Delta D}{\delta D})^2} \tag{1.15}$$

where Δr is the distance between the reference voxel and the measured voxel, δr is the specified positional accuracy (i.e. 1 mm), ΔD is the dose difference between the reference voxel and the measured voxel (measured in % of the prescription dose), and δD is the specified dose accuracy. This is conducted for each voxel within δr of the specified point and amongst these points, the minimum Γ value is quoted. If the Γ value is less than 1, then the voxel passes, otherwise it fails. This analysis is conducted across an entire image and the percentage of voxels which have gamma value lower than 1 is referred to as the gamma pass rate.

1.6 Optimization

Optimization is the process by which a given function is minimized or maximized for a set of variable inputs. For the remainder of this introduction, the function to be minimized (also known as the ”cost” or ”objective” function) will be referred to as $f(w)$, and the variable w refers to a set of input variables. Mathematically, the goal of optimization is to find the value of w which satisfies:

$$w = \underset{w}{argmin}[f(w)] \tag{1.16}$$

Often times there are further constraints on w, for example if w represents beam intensity, then the value of w cannot be negative.

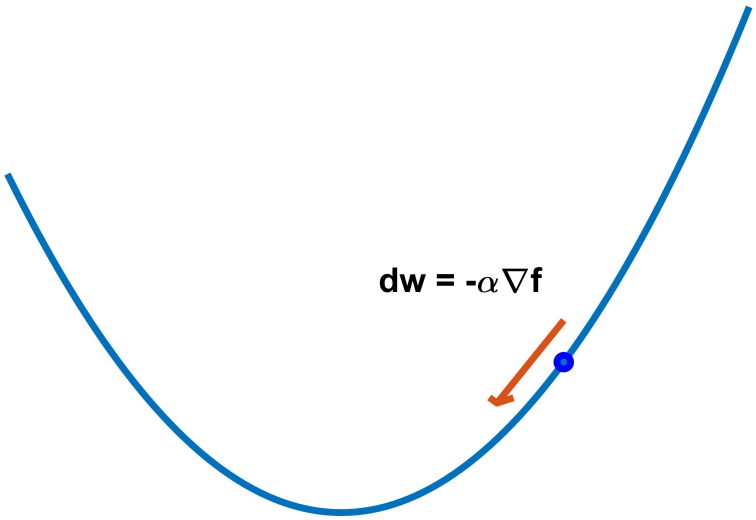

Figure 1.9: For functions that are convex, there is one minimum which is the global minimum. The gradient points in the direction of functional increase, so by searching in the opposite direction, the function minimum can be found.

1.6.1 Optimization Methodology

Gradient Descent

Gradient descent is a method used in the optimization of convex functions. In gradient descent, the variables are initialized at some value (typically 0, but if better estimates of the variables exist, they can be used), and the function minimum is found by iteratively correcting this guess by moving the solution in the direction of the negative gradient (illustrated in Figure 1.9). This iterative correction of the solution can be represented as:

$$w^{t+1} = w^t - \alpha\nabla f(w) \tag{1.17}$$

where w^t is the variables at iteration t and α is the step size: One example step size is

$$\alpha = \frac{1}{max(eig(\nabla^2 f))} \tag{1.18}$$

which denotes the inverse of the maximum eigen value of the Hessian of the cost function. While this approach guarantees convergence, it usually under-predicts the magnitude of the step size which results in longer optimization times. A more robust strategy is an adaptive step size using a backtracking line search method. In this method, the stepsize α_i (subscript i corresponding to the step size's dependence on iteration count) is initialized to a large value, and then it is exponentially decreased (iteratively multiplied by a number less than 1) until the Armijo-Goldstein condition [5] is met:

$$f(w - \alpha_i \nabla f(w)) < f(w) - \alpha_i c ||\nabla f(w)||^2 \tag{1.19}$$

where c is a control parameter set between (0,0.5].

Newton-based Methods

Newton-based methods rely on the Hessian of the function to find the perturbation. It relies on fitting a quadratic function to the local gradient and Hessian, and then minimizing the quadratic. The quadratic fit is accomplished by Taylor expanding the function about the given iteration's variables:

$$f(w + \Delta w) = f(w) + \nabla f(w)\Delta w + \nabla^2 f \Delta w^2 \tag{1.20}$$

This function is quadratic in the variable Δw and yields the minimized value when

$$\Delta w = [\nabla^2 f(w)]^{-1} \nabla f(w) \tag{1.21}$$

This method is faster than gradient descent when computing the inverse Hessian of the function is computationally feasible. For quadratic systems without boundary conditions, this method converges in a single optimization step.

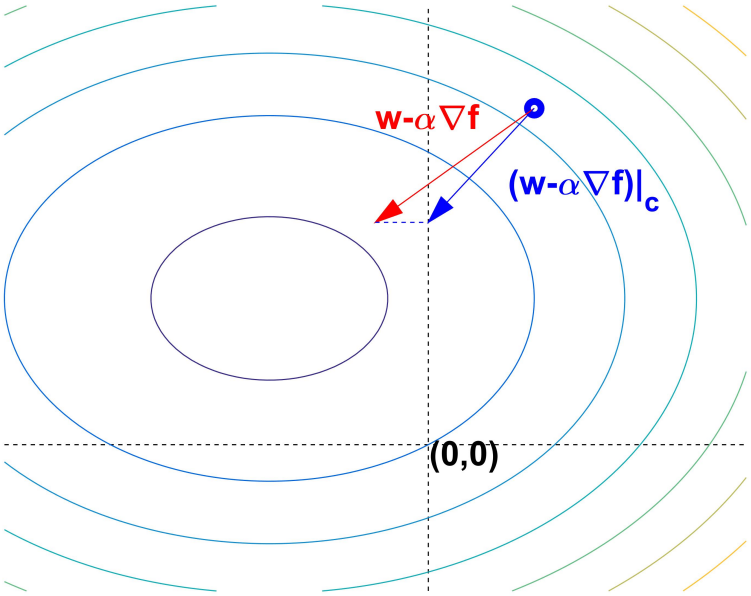

Figure 1.10: This figure shows the level set diagram of a function with inputs. In this example, the global minimum is outside of the contained set w ≥ 0. The gradient is calculated (in red), however the solution lies outside of the solution set. This is corrected by projecting the solution onto the closest point within the solution set. The minimum value that achieves the constraints lies on the boundary of the constraints (in this example, the y axis) and the gradient moves along the y axis until the minimum is achieved. For these optimizations, the variable α has increased importance as the projected gradient can be much smaller than an optimal step.

Constrained Optimization

There are multiple ways to deal with constrained optimization, the simplest of which is called the projected gradient method. In this method (illustrated in Figure 1.10), the gradient is calculated and then applied to the optimization variable of the iteration w_i. The solution is then projected onto the set of allowed values of w, and the optimization continues. The projected gradient method does not work for

Newton-based methods. One method to overcome this problem is to add a barrier function to the cost, which increases the cost when the optimization is outside the solution set.

Stochastic Optimization

In the optimization of non-convex functions, non-global minima exist and gradient methods produce solutions which tend to the local minima that is closest to the initial condition. For computationally simple problems, this feature can be overcome by sampling multiple initial conditions, allowing the solutions to find the local minima, and then reporting the minimum of the candidate solutions. However, in radiotherapy optimization this strategy is frequently computationally infeasible.

A competing strategy to find the global minimum is to use a process known as simulated annealing [46]. In this method, the function is initialized (w_0) and the variables are optimized using a stochastic iterative process. In each iteration, a perturbation (dw) is sampled from a distribution and applied to the function input variable of that loop (w_i). The function is then evaluated at $w_i + dw$ and the cost at this new variable input is calculated. The change in the function (Δf) is calculated using the formula $\Delta f = f(w_i) - f(w_i + dw)$. If the function decreased when compared to the previous iteration, then $w_{i+1} = w_i + dw$, while if the function has increased from the previous iteration, then the perturbation dw may still be accepted with a probability given by the Poisson-Boltzman equation.

$$P(i) = \exp(-\frac{\Delta f}{k_b T(i)}) \tag{1.22}$$

where i is the iteration number, $P(i)$ is the probability of accepting the deleterious perturbation, and $T(i)$ is the "temperature" of the solution at a particular iteration. This process allows solutions to "tunnel" out of local minima the same way as happens to non-globally optimal configurations in potential wells. During optimization, temperature is initially high, but as optimization progresses, the temperature is decreased so that the solution tends to a stable minimum. This temperature modulation is called the annealing schedule.

This method is sometimes unsuccessful at overcoming local minima. For methods such as simulated annealing, optimization convergence is slow and warm start-

ing the solution is of increased importance. Warm starting is the concept of choosing an initial function input (w_0) which is close to the desired minimum. Usually w_0 can be chosen from previous solutions or from heuristic initialization. In radiotherapy optimization, apertures are warm started using fluence-based optimization (Section 1.6.1) or with apertures defined by a conformal treatment plan.

Fluence-Based Optimization

For fluence-based optimization, the linac beam is subdivided into gridded sections. Photons incident on each of these section will, on average in aggregate, contribute different amounts of dose to different voxels within the patient (which may be designated as an organ or a target). These dose contributions, denoted as D_{ij}, where D is the dose deposited to voxel i from subsection j, is illustrated in Figure 1.11. D_{ij} depend solely on the energy spectrum of the beam, and on the geometry of the patient. While these dose contributions cannot be readily modulated, the fluence intensity of the beam, w, can be. This is accomplished by changing the shape and intensity of the photon beam using the MLC. The modulated fluence intensity of a subsection can be denoted as w_j. There will be bs total fluence weights w_j, where b is the number of beams, and s is the number of subsections in a linac beam. The number of subsections used in this study was 6,400, which represents a 20 cm by 20 cm wide beam subdivided into 2.5 mm sections (the width of the MLC). Using the above notation, the dose delivered can be calculated as:

$$D_{total} = Dw \tag{1.23}$$

where D is a matrix of dimension bs by v (the number of voxels), and w a column vector of length bs. One possible cost function is to define the optimal dose that should be delivered at each voxel. This can be represented as:

$$C = ||Dw - d_{con}||^2 \tag{1.24}$$

$$w_j \geq 0 \qquad \forall j \tag{1.25}$$

where C is the objective function and d_{con} (which is a vector that is is v x 1) are the optimization constraints which define a dose for each voxel being calculated.

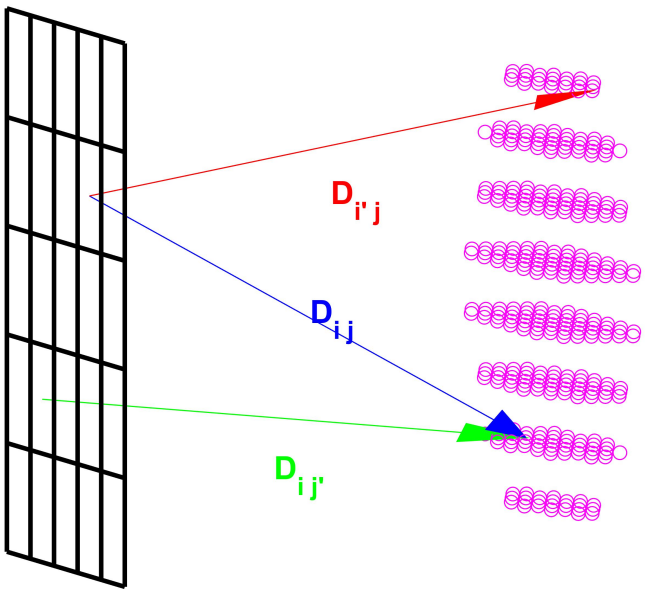

Figure 1.11: Illustration of dose contribution of fluence subsets of a linac beam. On the left, the linac beam is subdivided into fluence contributors. Photons travel through subsection j of the beam and deliver a dose of D_{ij} to voxel i (in blue). Photons from subsection j' can also deliver dose to voxel i, but in a different amount denoted by $D_{ij'}$. Similarly, photons from subsection j also deliver dose to other voxels such as i'. These dose contribution factors build a matrix D which has size bs by v, where bs is the number subsets in the beam times the number of beams, and v is the number of voxels

While the matrix D and vector d_{con} are constants set by geometry and the user respectively, w is a variable which can be optimized. This cost function has a well defined gradient and Hessian and can be optimized with constrained gradient descent or a Newton-based method (Section 1.6.1). While this cost is simple from an optimization standpoint, it does not provide a simple way for practitioners to convey their desires to the optimization system. Therefore other cost functions have been developed, which are further explained in Section 1.6.2. Optimal fluences

are found by some optimization process, and then these fluences are converted into deliverable beams using MLC sequencing algorithms.

The conceptually simplest MLC sequencing algorithm is a step-and-shoot algorithm for which deliverable fluences are considered on a MLC-pair by MLC-pair basis. Each MLC-pair defines a row in the fluence grid (the grid shown in Figure 1.11). The row will define a linear function of optimal fluences. These fluence values can be discretized into level sets. These level sets can be delivered sequentially, delivering the low dose levels first, and then constricting the size of the aperture and delivering the higher level sets. The level of discretization will affect the accuracy of the conversion, however over-discretization of the function will require many level sets to be delivered and increases time of delivery and exposes the patient to leakage dose as the MLC does not completely block the beam. There are many competing methods to MLC sequencing, but these are beyond the scope of this work as this work mainly focuses on direct aperture optimization.

1.6.2 Cost Functions used in Radiotherapy Planning

Radiotherapy cost functions are created to convey the desires of the treatment planner to the optimization software. The simplest possible cost function is one where the desired dose of every possible voxel is specified to a particular value (given as Equation 1.24). While this equation is easily understood by optimization software, it is difficult to convey the desired treatment parameters in the defined constraints D_{con}. In particular, defining the best possible dose to a particular voxel is a complex function of cancer type, target location, OAR location, photon beam energy of the treatment beam, and the capabilities of the optimization software. There has been recent progress in this regards using atlas-based learning methods to produce voxel-based automated dose prescriptions [63]. Previous to this recent progress, other cost functions (explained in the following paragraphs) have been developed to convey the desires of the treatment planner.

Another convex function which can be used for dose optimization is the generalized p-norm which takes the form:

$$||d||_p = (\sum_{i=1}^{N} d_i^p)^{\frac{1}{p}} \tag{1.26}$$

This function is convex and differentiable for $p > 1$ and is conveniently identical to the gUED for serial and parallel organs with $p = \frac{1}{n}$ and multiplied by the scaling factor $(\frac{1}{N})^{\frac{1}{p}}$.

Another physically meaningful dose criteria is the dose-volume objective [11]. These criteria are widely used in radiotherapy and for this reason they are incorporated into some optimization methods. One can express dose-volume objectives in a cost function as:

$$C = \sum_{organs,targets} k_i \int \times (D(v) - c \times D_0(v))^2 dv \tag{1.27}$$

In this equation, the dose contribution to each organ is approximated by point cloud representations and calculating the dose to to each point from each beam in the treatment. Point clouds can be used to approximate dose to OAR, PTV, or normal tissue. The dose delivered to these point clouds can be used to calculate the DVH, which is designated as $D(v)$.

However, this cost function does not account for the particular dose effects on different types of tissue. For example, an OAR receiving less dose than the constrained dose does not deleteriously affect the quality of the treatment. Therefore no cost should be assigned if the OAR receive less than the constraint dose. ICRU report 50 [41], and more recently ICRU report 83 [36], provide guidelines for prescribing doses in radiotherapy. These guidelines state that for the purposes of finding a direct correlation between delivered dose and patient outcome, doses to the PTV should be close to uniform. In particular, ICRU report 50 states that doses to the PTV should be no less than 95 % of the prescribed dose and no more than 107 % of the prescribed dose [41]. This can be achieved in the cost function with two parameters: one which penalizes under-dosing, and another term which penalizes over-dosing. Typically, there are no further constraints set on the PTV, however, there have been clinical trials which have explored varying the dose inside the PTV guided by biological imaging [8].

These features can be mathematically expressed as

$$C = \sum_{structures_i} w_i \int H_1 \times (D(v) - c \times D_0(v))^2 dv + \sum_{targets_i} w_i [\int H_2 (D(v) - P_{min})^2 dv - \int H_3 (P_{max} - D(v))^2 dv] \tag{1.28}$$

Where P_{min} is the prescribed minimum dose to the target, P_{max} is the maximum dose to the target, H_1 is the Heaviside function which equals to 1 when $D(v) - c \times D_0(v)$ is positive and 0 when $D(v) - c \times D_0(v)$ is negative. H_2 and H_3 is similarly the Heaviside function, but with $D(v) - P_{min}$ and $P_{max} - D(v)$ as their respective inputs. While this function is not convex, it has been shown that local minima are sufficiently close to the global minima such that the they can be used in radiotherapy optimization [97].

1.6.3 Volumetric Modulated Arc Therapy

VMAT was initially called intensity modulated arc therapy (IMAT) and was pioneered by Yu [100] as an inverse planning method in which the MLC and gantry dynamically move while the beam is on. A complete history of the development of VMAT is provided in [15]. At the initial introduction of this method, it was dosimetrically inferior to static field IMRT. These difficulties are understandable as VMAT is a difficult optimization problem due to the additional degrees of freedom introduced by the linac gantry rotation. Additionally, these degrees of freedom have complex constraints due to the continuous movement of the MLC and gantry while the beam is on. However, these have since been over-come and VMAT is regarded as dosimetrically equivalent for the treatment of many indications.

VMAT trajectories are continuous gantry trajectories when they are delivered. These continuous trajectories can be modelled as static beams (control points (CPs)) along the trajectory. For a treatment plan to have accurate dosimetry, CPs need to be spaced every 1-5 degrees depending on the location and shape of the treated indication. A set of physical constraints is imposed at each CP due to the physical limitations of the linac and its components. In particular, as the gantry can be rotated at 6 degrees/second, the time interval between two successive control points can be as small as 0.2 seconds. Furthermore, the MLC is only able to move be-

tween 2-3 cm/second (depending on model), which imposes a tight constraint on the allowed MLC positions between successive control points. If MLC_i^j is the j^{th} MLC position of the i^{th} control point, then this constraint means that:

$$\begin{aligned} \frac{\delta MLC}{\delta t} dt &> |MLC_i^j - MLC_{i+1}^j| \\ \frac{\delta MLC}{\delta t} dt &> |MLC_i^j - MLC_{i-1}^j| \end{aligned} \tag{1.29}$$

where $\frac{\delta MLC}{\delta t}$ is the MLC velocity and dt is the time between each control point. A typical value for this product in 0.5 cm. Additionally, MLC positions cannot collide with one another when they move. A safety buffer distance is added which can be expressed as

$$b < MLC_i^{2n+1} - MLC_i^{2n} \tag{1.30}$$

where n is the number of MLC pairs and b is the size of the buffer (e.g. 1 mm).

There are two approaches that have found the widest adoption. The first solution was the progressive sampling alogorithm [71] which is a direct aperture optimization (DAO) strategy. Other approaches have incorporated fluence-based optimization [7, 14], and both approaches have been found to provide clinically suitable dose distributions. The majority of this work is based on the progressive resolution algorithm which is described in [71].

Direct Aperture Optimization VMAT

An overview of the progressive sampling algorithm is summarized in Figure 1.12. The gantry arc is initially approximated by a small number of discrete control points. These control points are sufficiently spaced out so that the MLC is able to form any mechanically feasible MLC aperture. These control points have the initialized MLC positions of a conformal treatment plan: the projection of the MLC is set to conform with the beam line projection of the PTV (plus a margin which depends on treatment site). A typical conformal aperture is shown in Figure 1.13. The dose deposited by each of the control points' apertures to the OAR and PTV are calculated using the PBC algorithm. The initial beam weight is set so that the mean PTV dose is equal to the prescription dose.

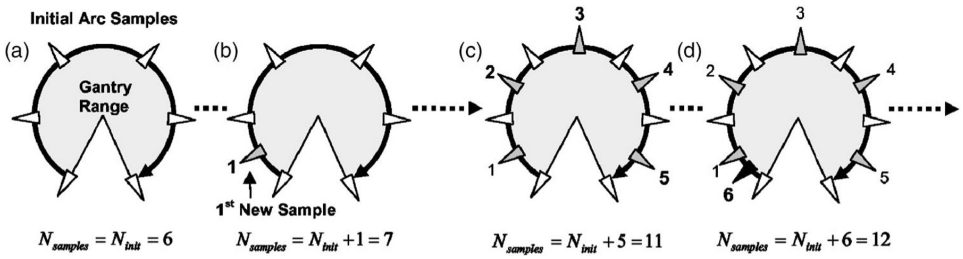

Figure 1.12: Illustration of the progressive sampling algorithm. a) the initial trajectory is sparsely and discretely sampled as a collection of control points which are evenly spaced along the gantry trajectory. The MLC apertures and MU of the beam are optimized using stochastic optimization. b) New control points are added in-between two adjacent control points and initial MLC positions are set to be the linear interpolation of the adjacent control points. d) This procedure is continued until there are enough control points along the trajectory to approximate a continuous delivery. This figure was reproduced from [71] with permission from Wiley Publishing Group.

Next, the MLC positions and MU are subsequently optimized using stochastic optimization (Section 1.6.1) to meet the dose constraints (cost function) of the particular plan. This process is continued for a sufficient amount of time until the cost reduction from each optimization loop plateaus around zero.

In the next step, CPs are inserted in-between the previously defined CPs as the linear interpolation of the beam parameters. This includes MLC position, gantry angle, and number of MU delivered. Adding control points in this manner serves two functions. Firstly, the new control points provide extra freedom for the dose deposition as the beam can form new MLC apertures and deliver dose from new directions. Secondly, they increase the accuracy of the dose calculation, which is approximated by representing the continuous VMAT delivery as an interpolation of a number of static beams defined at each control point. This approximation is less accurate for sparsely spaced control points, but, as the control points are spaced closer and closer together, the approximation sufficiently models the delivered dose.

The set of control points formed by the initial CPs and the added CPs are again perturbed using simulated annealing, however, now the apertures are held

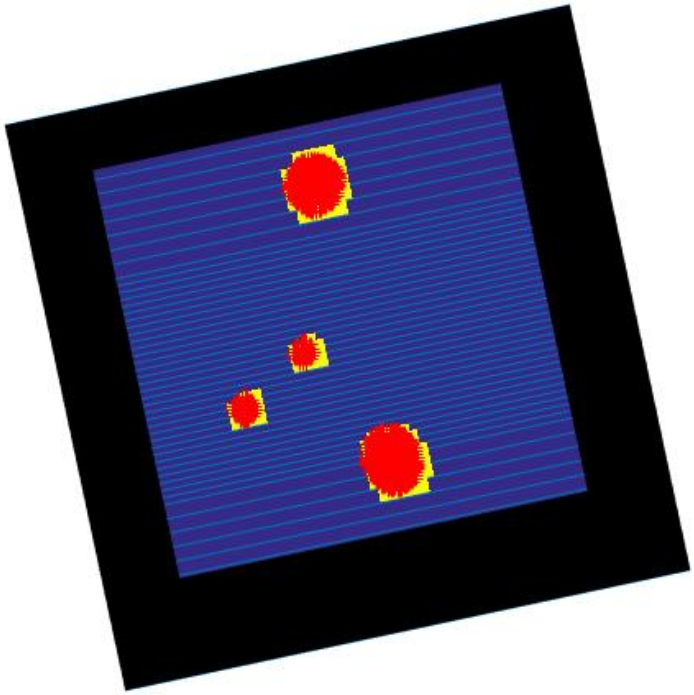

Figure 1.13: A beams-eye-view of a typical conformal aperture. The blue lines signify the edges of the MLC leaves, the red blobs are PTVs projected along the axis of the beam, the yellow designates open fluence. The MLC positions are found by taking the minimum and maximum extent of the PTV contours.

to the constraints defined by the mechanical specifications of the MLC (such as in Equation 1.29). The cost is again evaluated between each perturbation, and when a minimum is met, further CPs are added. This process is continued until the continuous trajectory is accurately approximated. A CP spacing of 2 degrees in the gantry angle is sufficiently accurate for clinical applications.

1.6.4 Treatment Planning for stereotactic radiosurgery (SRS)

SRS with a linac was pioneered in 1988 by Lutz et al. [58]. At the onset, Lutz et al. realized the importance of multiple entrance angles for these deliveries, and treatments were made up of dynamic gantry arcs at various couch angles (around four

non-coplanar arcs per treatment). These treatments were conducted with collimation cones, which limited treatments only to small, regularly shaped targets. With the introduction of the MLC, the arc technique was improved to include tumors of irregular shape. This was achieved by dynamically changing the MLC leaf positions so that the beam aperture conforms to the target as the gantry rotates [87]. This technique was named as dynamic conformal arc (DCA) and is still used to this day. While DCA can produce highly conformal treatment plans, it is a forward planning method which becomes overcomplicated when treating multiple targets, which is often the case with the treatment of brain metastases.

As computer-aided planning became more streamlined, inverse planning methods were developed to utilize the new technology. The first of which was IMRT, however, for this method to have enough entrance positions in the SRS setting, seven or more static fields were typically needed. VMAT treatments allow fluences from multiple angles while having time efficient deliveries and are well suited for SRS deliveries. The inverse planning methods developed by various groups [16, 37, 90] allow for complex treatments which treat multiple targets simultaneously.

Single isocentre treatment planning has been shown to be an effective way to create highly time-efficient treatments for treating multiple metastases with SRS. Inverse planning methods lend themselves especially well to this technique as high conformity can be achieved through MLC and dose rate modulation (which ensures that the amount of healthy tissue which recieves ablative radiation dose is minimized). Lau et al. [51] reported comparable clinical outcomes, but with drastically reduced treatment times, for patients treated with single isocentre VMAT technique containing one to two arcs when compared to patients treated with conventional multiple isocentre treatments. Thomas et al. [90] performed a retrospective treatment planning study on patients with multiple metastases previously treated with Gamma Knife. They found that their single isocentre VMAT plans with 4 non-coplanar arcs produced dose distributions of comparable quality to other methods that used specialized equipment (such as Gamma Knife).

1.6.5 Couch-Gantry Trajectory-Based Deliveries

While multiple non-coplanar arcs can produce highly conformal dose distributions, they increase the delivery time. The extra time needed to accommodate patient repositioning for multiple non-coplanar arcs can be mitigated by the use of dynamic couch motion. This style of treatment was introduced in 1988 by Podgorsak and his colleagues at McGill University [75]. While this method was found to have dosimetric and treatment time saving benefits, it did not gain a wide acceptance as none of the major linac manufacturers adopted this technology. This method was also limited to SRS cones (circular tertiary collimators of varying diameter which are matched to the divergence of the beam) only as it pre-dated MLCs.

With the release of the TrueBeam linac in 2010, Varian introduced a non-clinical Developers Mode [1] that allows trajectory-based delivery. When operated in Developers Mode, the TrueBeam linac is capable of dynamically moving the gantry, collimator, MLC, jaws, and the couch while the beam is on, allowing complex three dimensional trajectory beam delivery. This development has sparked new interest in the development of an optimization framework for trajectory volumetric modulated arc therapy (TVMAT) deliveries of cranial [59, 86, 99] and extra-cranial treatments [53, 84, 102] as well as in the development of QA methods for this mode of delivery [93, 95].

Soon after the release of the TrueBeam, Yang et al. [99] devised an optimization framework to create optimal dynamic couch-gantry trajectories by implementing an algorithm to minimize doses to Organs at Risk (OARs) using an OAR overlap metric along the delivered trajectory. MacDonald and Thomas [59] and Smyth et al. [86] applied this method in cranial SRS and found that the method successfully improved target dose conformity and lowered doses to OARs when compared with standard VMAT plans. However, the trajectories were not necessarily time optimal and involved sporadic couch movements, which may be uncomfortable or may result in intra-fraction motion.

The effect of treating with highly co-planar treatments was explored by Nguyen et al. [68] when they developed an unconstrained IMRT optimization process for cranial delivery. In this method (which was named 4π radiotherapy), fluences were allowed from candidate beams which were uniformly distributed across the deliv-

erable phase space (couch-gantry angle contributions which would not result in collisions of gantry and patient). The fluences were optimized to produce the globally optimal treatment. Next, fluences directions were removed based on which delivered the lowest fluence and the plans were re-optimized. This was continued until there were only 20 candidate beams left which was chosen as a trade-off between delivery efficiency and quality. Delivery sequence of these candidate beams was optimized using a travelling salesman optimization algorithm. This approach was extended to couch-gantry arc treatments by Langhans et al. [50] who delivered VMAT treatments which connected the phase space points of the delivered IMRT beams.

Due to the complexity of the TVMAT technique, machine specific QA protocols need to be developed prior to its implementation. There has been preliminary work in this field both within our group and externally. Victoria et al. [93] developed QA methods to tests the synchrony of motion of various components of the TrueBeam linac (couch, gantry, and MLC). However, their work did not include synchrony tests for dynamic gantry-couch motion including variable dose rate. To our knowledge, the only reported work in this respect comes from our group.

1.6.6 Collimator-Gantry Based Trajectories

The collimator and MLC act in synergy to form optimal apertures. However, the mechanical specifications of an MLC (defined in Section 1.2.2) set limits on the apertures which the linac can form. Firstly, the MLC provides a rotationally asymetric forms of collimation as the leaves only protrude into the beam from two directions. Therefore the shapes which can be produced by the MLC depend on the angle of the collimator. Secondly, the MLC does not completely block the beam. The body of the MLC only blocks approximately 98% of the beam while radiation leakage between parallel leaves (known as inter-leaf leakage 2%) and end leaf gap leakage (the leakage between abutting MLC leaves (1 mm minimum gap size)) is even greater. Collimator angle optimization can potentially minimize the effects of these mechanical shortcomings.

Historically, there has been little conclusive study on the effect of collimator rotation on the efficiency and quality of radiotherapy delivery. The reason for this

is that the collimator angle will affect MLC sequencing algorithms differently. Initially, when conformal therapy was the standard of care, the collimator angle would be selected using treatment planner experience and a trial-and-error approach. This strategy has continued into modern technology. However, some groups have explored strategies which may out-perform and automate this method.

Otto and Clark [72] explored the effect of rotating the collimator at a constant angular velocity intra-treatment during static field IMRT delivery with the hopes of increasing the accuracy and efficiency of fluence map delivery. Milette and Otto [65] tested this method and found that it provided an increase in the accuracy of the delivery of concave fluence shapes (such as a shoehorn shape) and a spreading of the dose contribution from inter-leaf leakage which reduced intensity of the hot-spots due to leakage by a factor of two.

Webb [94] explored whether collimator rotation intra-treatment would reduce the frequency and effect of "parked gaps" (end-to-end leaf leakage) by considering the collimator angle during the optimization process. In this work, a method was developed to minimize the number of parked gaps for the delivery of fluences which were convex shapes. This work also explored collimator angle optimization for the delivery of multiple concave fluence shapes.

Zhang et al. [102] developed methods for the optimization of the collimator angle to block the spinal cord in stereotactic body radiotherapy (SBRT) treatments. In their work, Zhang et al. [102] found the principal long axis of the spinal cord by decomposing contours using principal component analysis (PCA), and then aligning the collimator so that the MLC leaves were perpendicular to the spine, so as to best protect it from radiation.

Yang et al. [99] expanded on the work of Zhang et al. [102] by incorporating collimator-couch-gantry trajectories in VMAT deliveries. This work used a heuristic OAR-overlap cost function to optimize the couch-gantry trajectory and then further optimized the collimator angle using methods derived from Zhang et al. [102]. The couch trajectory was optimized so that fluences would minimize PTV overlap with OAR, while the collimator was optimized so that the MLC leaves would be perpendicular to the long axis of the OAR.

Locke and Bush [55] explored the effect of collimator optimization on the progressive sampling algorithm (described in Section 1.6.3). They developed a

PTV connectivity metric which could be used to initialize DAO-VMAT for complex torus-shaped PTVs so that optimization would not get stuck in local minima. Their method also incorporated collimator angle optimization using a graph search method.

As single isocentre treatment of multiple metastasis is a relatively new treatment modality (pioneered independently by two groups in 2010 by Clark et al. [16] and Hsu et al. [37]) there has been no publications on the effect of intra-treatment collimator rotation for VMAT treatments of multiple brain metastasis. However, Wu et al. [98] explored the optimization of static collimator angles for VMAT treatments. In this work, a heuristic cost function was developed which was the area of open fluence for a conformal treatment plan. This function was minimized for static collimator angles and treatment plans were optimized using Varian Eclipse. They found a significant decrease in the low dose bath, with the most drastic improvement in the volume that receives 5 Gy of radiation.

MacDonald et al. [60] independently developed a similar cost function to the one explored by Wu et al. [98]. In their formulation, the whitespace was calculated by adding the open fluence (defined by the jaws) and subtracting the area of overlap with the MLC, PTV alone and PTV overlapped with OAR. This added extra weighting terms which could be modulated to incorporate various aspects not considered by Wu et al. [98] such as MLC leakage and avoidance of OAR. MacDonald et al. [60] optimized the collimator trajectory in DCA treatments using a cost-valley tracing algorithm. Using this approach they performed a treatment planning study of 15 simulated treatment cases which had three and four metastases. They found that the dynamic collimator DCA treatments had lower monitor units and dose bath than the VMAT treatments, but failed to find any significant differences between the trajectory-optimized and static-collimator-optimized DCA treatment plans.

1.7 Thesis Overview

This project is aimed at combining the successes of previous treatment modalities, to achieve an optimal cranial SRS treatment plan that could be delivered in a time-efficient manner. We explore several algorithms in which the couch and the collimator are allowed to move dynamically to achieve these goals.

The first strategy that is considered in Chapter 2 is allowing a complete 4π sampling of the allowable phase space by implementing trajectories of the couch and gantry. The optimization strategy that was found to be most efficacious was a patient-generalized trajectory in which the couch rotates across its full range of motion while the gantry delivers partial arcs. This trajectory can be modulated to increase sampling of the phase space by allowing gantry to sweep more times, or the sampling can be reduced if the treatment quality is not improved so as to reduce treatment time.

This work additionally shows that these methods can be delivered safely by performing end-to-end patient specific quality assurance for a series of test cases. Delivery verification is further developed in Chapter 3, which presents a machine-specific quality assurance for accurate characterization of the couch rotational accuracy.

In Chapter 4, this thesis explores the effect of allowing the collimator angle to be a free parameter in the optimization. This is accomplished by implementing an altered version of the heuristic cost function developed by [98], and minimized with a constrained Djikstra graph search method. Additionally, the QA methods developed in Chapter 3 are extended to the collimator.

In Chapter 5, the work in the main results of this thesis are briefly summarized and directions of further inquiry are suggested.

Chapter 2

Couch-Gantry Trajectory-based Stereotactic Radiosurgery Treatments

2.1 Introduction

In cranial SRS, highly conformal ablative radiation is delivered to small, well-defined targets in the brain in a single fraction. For an SRS technique to be successful, dose to the target should be highly conformal with rapid dose falloff outside the lesion. Commonly used treatment modalities for these deliveries include specialized devices such as Gamma Knife and CyberKnife [43], as well as conventional C-arm linear accelerators. In conventional C-arm linacs, the high degree of target dose conformality and rapid dose falloff are achieved with multiple beam entrance angles that are typically accomplished with non-coplanar arcs. Two arc techniques, DCA [58, 87] and VMAT [21, 90], are used to achieve these dosimetric objectives.

The DCA technique is a forward planning method that becomes increasingly complicated to plan and deliver when there are multiple targets, as is typical in the treatment of brain metastases. Recently, VMAT is becoming increasingly adopted for treating multiple metastases with SRS [21, 90] as it uses an inverse planning strategy. However, non-coplanar VMAT can be cumbersome to plan and deliver

since multiple couch re-positionings are required and the number of arcs and the planes of inclination of the arcs are not considered during optimization. This work tries to mitigate these shortfalls by the use of simultaneous couch and gantry motion that enables a time-efficient delivery while affording the planning algorithm a large portion of the couch-gantry phase space.

The use of simultaneous couch and gantry motion for SRS was first introduced in 1988 by Podgorsak and his colleagues at McGill University [75]. While their method was found to have dosimetric and treatment time saving benefits, it did not gain a wide acceptance as none of the major linac manufacturers adopted the technology. As linac manufactures opened up the degrees of freedom of the device, there came a renewed interest in this field. The first of which was conducted by Yang et al. [99] who devised a method to create dynamic couch-gantry trajectories by implementing an algorithm which minimizes beam overlap with OARs. This was accomplished by creating a beam overlap metric for each couch and gantry combination, and then finding smooth paths through phase space which minimizes this metric. MacDonald and Thomas [59] and Smyth et al. [86] applied this method in cranial SRS and found that the method successfully improved target dose conformality and lowered doses to OARs when compared with standard VMAT plans. However, these trajectories were not necessarily time-efficient or dosimetrically optimal as they were predefined before MLC and dose rate modulation. Additionally, they involved sporadic couch movements, which may be uncomfortable, and potentially result in intra-fraction motion.

In this work, we propose and validate a method that uses a patient-generalized trajectory that approaches 4π geometry, and thus approximates a fully sampled trajectory. We also present preliminary analysis on creating time optimal trajectories, while still maintaining the treatment plan quality, by developing methods that systematically remove portions of the beam trajectory while not significantly contributing to the dose delivery. These treatments were compared to the dynamic conformal arc method and were dosimetrically validated by delivery on the TrueBeam linac via Developer Mode.

2.2 Methods

2.2.1 Optimization

The developed optimization protocol has three main components (illustrated in Figure 2.1). First (Figure 2.1a), a patient-generalized trajectory is constructed which is well suited for cranial indications. Next (Figure 2.1b), this trajectory is fed into an optimization framework which optimized MLC and dose rate configurations along the input trajectory. Finally, the spatial sampling frequency is optimized to ensure a time-efficient delivery (Figure 2.1c-d). These three features combine to produce both a dosimetrically optimal and time-efficient trajectory. The details will be discussed below.

The Couch-Gantry Trajectory

The central feature of this method is the couch-gantry trajectory in which the couch rotates through 180 degrees while the gantry makes 2-8 partial arc sweeps across the cranium (illustrated in Figure 2.1). As the number of partial arcs increases and the beams begin to overlap, this trajectory increasingly samples 4π geometry. The trajectory is patient generalized and has a reproducible beam geometry for patient specific QA. Additionally, while this trajectory allows complete sampling of the phase space, plans are optimized to be patient-specific by variable MLC positions and dose rates that are calculated to provide maximal OAR sparing and conformity to the target.

The couch-gantry trajectory is formed using a trajectory generating function:

$$G = \begin{cases} -85\cos(N \times C) + 90 & \text{if } C < 0 \\ 0 & \text{if } C = 0 \\ 85\cos(N \times C) + 90 & \text{if } C > 0 \end{cases} \tag{2.1}$$

where G is the gantry angle, C is the couch angle (on the interval [-90,90]), and N is the number of partial gantry arcs (coordinates defined in IEC 61217 [18]). For illustration of this technique, refer to Figure 2.1. When N is set to three, the trajectory in Figure 2.1 c,d is produced, while when N is set to eight the trajectory in Figure 2.1 a,b is created. The amplitude of the sinusoid was set to 85, which was

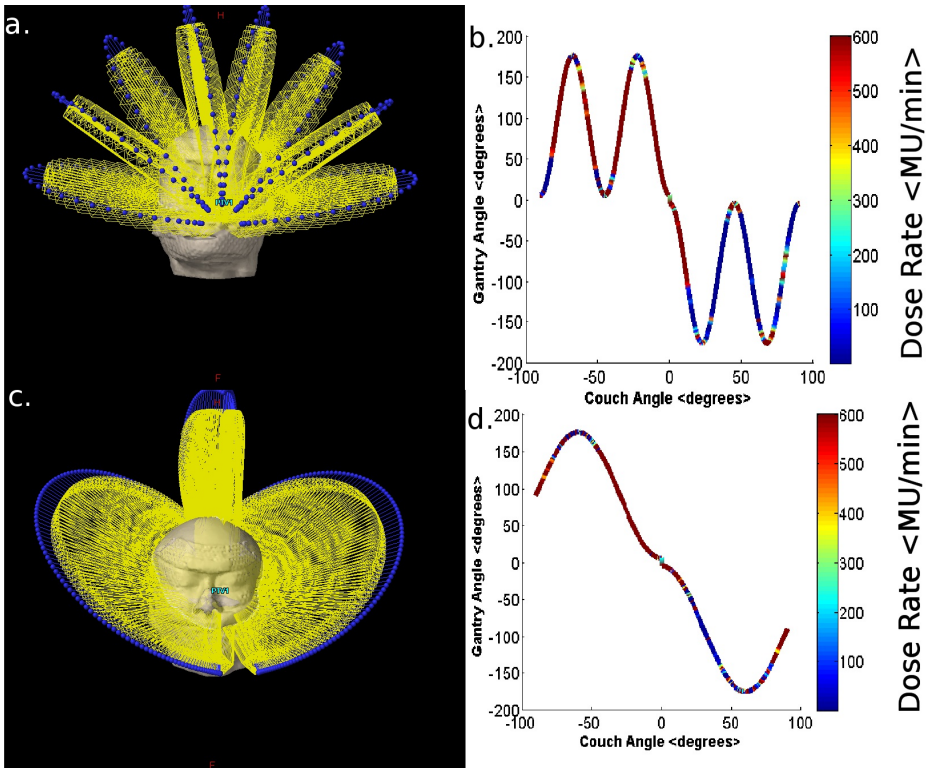

Figure 2.1: An overview of the Optimization Process. a)A predefined trajectory which fully sampled 4π geometry is fed into the optimizer. b) In-house optimization algorithms find the most optimal MLC and dose rate combinations for a given patient geometry and cost function. c)The sampling of the phase space is reduced as much as possible without reducing plan quality metrics or cost. d) New MLC sequences are selected using the optimization algorithms in b.

set lower than 90 because at gantry angle 90, all of the beams would overlap as the gantry would be positioned vertically. In this chapter, one couch gantry trajectory was centred on each of the lesions.

Dose Rate and MLC modulation

Treatment plans were optimized using in-house software that was written in MATLAB and based on the direct aperture optimization progressive sampling algorithm

described by Otto [71]. The base trajectories were loaded into the optimizer as a set of static control points that designate couch and gantry positions. The optimizer set up the initial condition of optimization by sparsely sampling the trajectory at a reduced set of control points, which were evenly spaced by 40 degrees. At these control points, the MLC (Varian HD120) was set to conform to the target with a 0 mm margin. Doses for each control point were calculated using an in-house MATLAB implementation of the pencil beam convolution algorithm. Doses were calculated only for critical structures and normal tissue within a 3 cm margin around the PTV so as to reduce computation time. Control point doses were uniformly scaled such that the target was covered by the prescription isodose. Once each control point was initialized, a scalar cost function (Equation 2.2) was evaluated which related the dose delivered to clinical variables of interest.

Next, the initial control points were perturbed stochastically in MLC position and dose rate (DR). Initially, perturbations were large to ensure the plans avoided local minima, however as optimization progressed, perturbation sizes were linearly decreased so that minimal cost values could be found. After each perturbation, the cost function was re-evaluated, and if the perturbation was found to reduce the cost function, it was kept. Otherwise the previous value was retained, and a subsequent perturbation was resampled. As optimization progressed, new control points were introduced as linear interpolations of the adjacent control points so as to ensure a continuous delivery [71]. Additionally, the physical limitations of the device were taken into consideration for the sampling of the perturbations: only MLC and DR perturbations which could be physically achieved in a continuous gantry-couch arc were sampled from. For MLC positions, this was defined by the max velocity and for DR, this was the maximum DR given the beam settings. The optimization was conducted for 20 minutes with additional control points being added in evenly spaced increments of 3 couch-gantry degrees.

Delivery Time Optimization

Delivery time was optimized by variably sampling the phase space and calculating competing plans. If the plans redundantly sampled the phase space due to the beam trajectories overlapping, then the treatment time would be increased unnecessarily.

To find the time optimal sampling of the phase space, couch-gantry trajectories with varying numbers of partial arcs were constructed. At first, eight partial arcs were used, as this corresponds to a near complete sampling of the phase space and gives the treatment planning algorithm a benchmark to compare other plans against. Next, the number of partial arcs (N) were varied between eight partial arcs (Figure 2.1a, a near-complete sampling of the phase space) to two partial arcs (a Podgorsak trajectory [75]) in an increment of 0.5 arcs. Each of these plans were optimized and then compared. The plan which provided the most sparse sampling of the phase space while producing the same dosimetric result was selected.

Cost Function Calculation

The cost function was designed to include the most clinically relevant variables for SRS delivery: doses to OAR, PTV dose conformity, and dose falloff. Doses to OARs were represented as user-assigned dose-volume constraints and relative importance factors. The calculation of the cost (C) was conducted using the following equation:

$$C = [0.5 + 0.25(CI - CI_{Con})^2 + 0.25(H(FO - FO_{Con})^2] \times \sum_{i=1}^{n} w_i (DVH_{Con_i} - DVH_{Ach_i})^2 \tag{2.2}$$

where CI is the calculated conformity index; CI_{Con} is the optimal conformity index (which was set to 1.0); FO is the calculated dose falloff; FO_{Con} is the constraint falloff, which was set to 2.0; and w_i is the weight for a particular DVH constraint which was set to unity for this treatment planning study and judicially changed if needed.

Doses to OAR and PTV as a function of DVH values were assigned a weight of 0.5 of the cost associated with a particular plan, while conformity and dose falloff were each assigned a weight of 0.25. These weighting parameters (0.5, 0.25, 0.25) were found by manual manipulation to find consistent and high quality optimizations. These calculations used Paddicks conformity index (CI) [73] (Equation 1.12)

and a dose falloff (FO) [74] variable that was defined as:

$$FO = \frac{V_{50\%}}{T}$$

where T is the volume of the target and $V_{50\%}$ is the volume that receives 50% of the prescription dose.

If the achieved DVH, conformity index (CI), or fall off (FO) value was below the constraint value, then it was removed from the cost function. This formulation of the cost function allows one to control the relative importance of CI and FO objectives, while the DVH constraints are of unconstrained magnitude. The CI and FO difference terms represented in equation 2.2 will be of order unity so they each have approximately 25% contribution of the total cost. While there are other ways of achieving this goal (ie. adding the conformity index in quadrature, but with variable weighting terms, or various methods described by [42]), we found this method successfully and consistently produced plans of sufficient quality without any need of extra variables or complex methods.

2.2.2 Plan Comparisons

Patient Selection

Ten patients (summarized in Table 2.1) that were previously treated in 2014 with DCA (6 MV beam, planned using iPlan BrainLab AG) at our institution were selected for this study. These patients were anonymized and re-planned with the TVMAT method. Patient selection was designed to encapsulate a wide variety of cases to account for different planning considerations. There was diversity in disease sites with three accoustic neuroma (AN), three single metastasis (met) and four multiple met cases. Lesion size varied from 0.3 cm^3 to 12 cm^3 with a median volume of 3.4 cm^3. Tumor dose varied between 12 Gy to 24 Gy delivered in a single fraction treatment. The original DCA plans were planned using the iPlan TPS (BrainLAB AG) with one isocentre at the centre of mass of each PTV. The DCA plans were exported to the Varian Eclipse treatment planning system, and dose calculations were performed using Varian anisotropic analytical algorithm (AAA) without homogeneity correction. Each plan had between three and nine partial arcs

per plan which took approximately 15 to 40 minutes to treat. For comparison purposes, plans were also replanned using the "4 Arc" VMAT geometry presented in [90] with the same optimization methodology (cost function, treatment planning algorithms) of this study.

Table 2.1: Patient summary couch trajectory optimization study

Patient	Site	Number of PTVs	PTV Volume (cc)	Number of DCA Arcs	Prescription Dose (Gy/Fraction)
1	AN (R)	1	3.3	3	12/1
2	AN (L)	1	5	4	12/1
3	AN (R)	1	4.6	3	12/1
4	Met	1	0.9	3	18/1
5	Met	1	6.4	3	18/1
6	Met	2	7.7, 12.5	3	15/1
7	Met	2	4.6, 3.4	5	18/1
8	Met	2	5.8, 2.2	6	18/1
9	Met	3	2.6, 2.5, 1.7	9	18/1
10	Met	3	4.7, 0.4, 0.3	7	15, 24, 24/1

AN $\sim$ Acoustic Neuroma, (R) $\sim$ Right, (L) $\sim$ Left, Met $\sim$ Metastasis

Treatment Comparison

The primary goal in the development of this method was to reproduce the dosimetric results of the DCA method, then judicially try to outperform them in a select subset of clinical variables. To do this, the OAR portion of the cost function were based on the clinically achieved outcomes of the original DCA plans. The OARs DVH of the DCA plans were discretized into a set of constraints which were loaded into the optimizer. DVH dose constraints for the OARs were scaled by 90% of the clinically achieved values, both to account for minor differences between dose calculation engines (our in-house code and Varian AAA) and to ensure an outperformance of the clinical plans. The optimal conformity index, CI_{OPT}, was set to unity, which corresponds to only the PTV receiving the prescription dose. The value for

the most optimal falloff (FO_{OPT}) was set to two.

Treatment Time Comparison

Treatment time was calculated and compared for the acoustic neuroma patients (patient ID 1-3). The delivery was modelled as the linear interpolation of the control points. The assumptions on the gantry mechanical specifications are enumerated in Table 2.2). For each subset of the delivery (defined by two control points), the most constrained degree of freedom would be identified. For example, if between the first and the second control point the gantry rotates 2 degrees, while 30 MU are delivered and the MLC and couch are static, then the time for gantry rotation would be 0.33 seconds, while the MU delivery time would be 3 seconds. Therefore the delivery time would be limited by the dose rate and 3 seconds would be added to the delivery to account for this segment. This was conducted for all control point segments. Two methods were compared: maximal sampling (eight arcs), and the optimal sampling defined as the trajectory which produced a minimal cost value while having the fewest number of arcs.

Table 2.2: Maximum velocity model used to estimate delivery time.

Degree of Freedom	Max Velocity
Gantry Rotation	6 $\frac{deg}{sec}$
Dose Rate	600 $\frac{MU}{min}$
MLC Leaf Velocity	3 $\frac{cm}{sec}$
Couch Rotation	3 $\frac{deg}{sec}$

2.2.3 Validation of Deliveries

The optimized plans were exported as static beams to Varian Eclipse, and doses were calculated using the AAA with dose voxel spacing of 0.1 cm. These control points were spaced every 3 couch-gantry degrees. We tested whether this control point spacing was sufficient by up-sampling the delivery, and comparing the dose

distributions. While control point weights were maintained, plans were renormalized so that the minimum dose to the PTV was the prescription dose (plan quality set to 1). A subset of the patients (patient 1, 2 and 6) were selected for dose measurement verification. Due to the fact that Varian has not yet released dynamic couch motion for clinical deliveries, these measurements were performed in Developer Mode. Prior to delivery, machine commissioning procedures were conducted to ensure the linac was within tolerances for SRS deliveries. Dynamic couch picket fence analysis [101] (Section 1.5.1), as well as an isocentre stability measurement [30] (described in Chapter 3), was conducted. For the dynamic picket fence test, film was placed on the couch, and the couch and collimator were rotated at the same velocity while the MLC produced the picket fence pattern. Next the film was replaced, and the measurement was repeated without movement of the couch or collimator. The film was compared and the picket fence pattern produced by each method were indistinguishable from each other. Using the stability measurement [30], we found a max couch-isocentre wobble error of 0.4 mm with mean value of 0.2 mm.

Plans were exported as control points and translated into xml format. Next, the treatments were delivered on a cube phantom measuring 18.5x18.5x18.5 cm^3 for ion chamber and film measurements. Ion chamber measurements were performed with an IBA CC01 chamber with sensitive volume of 0.01 cm^3. GaFchromic EBT3 film measurements were performed along the sagittal and the coronal planes passing through the isocentre. Gamma analysis [56] was conducted using 2%, 2 mm passing criterion with a 10% minimum dose threshold.

Trajectory log analysis of the delivered plans was conducted and compared to the trajectory beam parameters of the treatment plans. This was done by comparing the expected positions of the beam axes (patient support angle, gantry rotation angle, MLC leaf positions) to the axes position that were recorded in the trajectory log files during the delivery of the plans. We compared the deliveries at each control point of the delivered plan. Each control point had a cumulative MU, couch angle, and gantry angle (and other beam parameters not compared in this study). The cumulative MU of each CP was found in the trajectory-log time series ($\pm$ 0.01 MU), and the recorded gantry and couch angles at these time points were compared to the expected values. The root mean squared error (RMSE) was calculated for

these parameters.

2.3 Results

2.3.1 Treatment Comparison

Treatment Comparison to Dynamic Conformal Arcs

Overall the developed TVMAT method was able to produce plans with similar or better dosimetric indices when compared to the DCA plans. Dose distribution comparisons are shown in Figure 2.4,Figure 2.5, Figure 2.6, and Figure 2.7 which correspond to patients 3,1,6, and 9. One can see that TVMAT produced more isotropic falloff. Additionally, the prescription isodose conformed more closely to the PTV. For this particular plan, dose rate modulation was successfully used to subtly reduce dose to the abutting brainstem structure while not compromising other planning metrics.

An overview of the PTV and normal tissue dose statistics are shown in Table 2.5. Planning metrics varied widely due to the variation in the location, size, and number of PTVs for each respective patient. When comparing TVMAT to the DCA method using the wilcoxon sign-rank (WSR) test, we found an increase in dose conformity from 0.65 to 0.72 ($p<0.01$), with an average improvement (mean $\pm$ 2 SE) of $10 \pm 2\%$. Dose falloff results decreased, but not significantly. TVMAT plans had a mean of 3.12 while DCA plans had a mean of 3.27, which amounted to an improvement of $4 \pm 2\%$ between the two treatment options. Dose homogeneity indices were similar for both techniques with an average value of 1.23 for TVMAT and 1.27 for DCA (% improvement = 3 ± 2 %). If one refers to Table 2.5, one can see the majority of patients had an improvement in V4 ($p<0.05$) and V12 ($p<0.01$) values. This resulted in a relative improvement of 20 ± 10 % for V_{4Gy} and 27 ± 10 % for V_{12Gy}. An overview of the significant improvements are shown in Figure 2.2.

Doses to OAR varied widely between treatments due to location of the indications with respect to the organs. Therefore it was not possible to find any trends in dosimetric values with the sample size used in this study. The DCA plans, VMAT and the TVMAT plans all conformed to QUANTEC [9] values. Additionally there

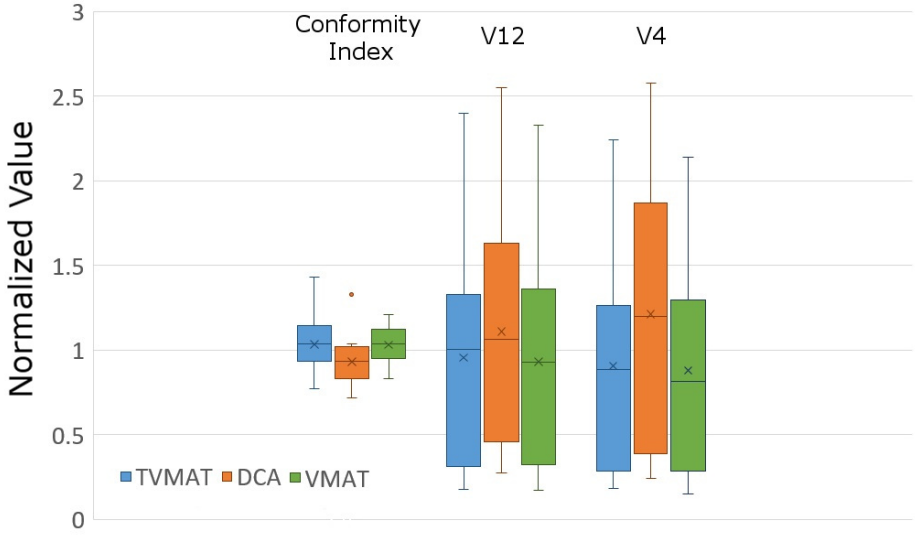

Figure 2.2: Boxplots of the variables of interest (conformity index, V12 and V4) which were statistically significantly different between TVMAT and DCA plans. Boxes show mean, quartiles, maxima, minima and outliers (shown as dots). Variables are normalized to mean values of the pooled data sets. TVMAT plans are shown in blue, DCA in orange and VMAT in green.

was a non-significant improvement in the volume weighted mean dose to OAR of 13 $\pm$ 13 %. Further planning studies with larger patient numbers are required to find if there is a relationship between this method and reduction of OAR doses.

Treatment Comparison: Volumetric Modulated Arc Therapy

The TVMAT technique performed similarly to VMAT when one compares dosimetric indices of Table 2.5. There were no appreciable differences between any of the evaluated quantitative values of the two methodology. The differences are summarized (average % difference $\pm$ standard error): conformity (0.7 $\pm$ 3 %), homogeniety (0.2 $\pm$ 0.7 %) , falloff (2 $\pm$ 2 %) , V12 (2 $\pm$ 2 %) and V4 (5 $\pm$ 3 %). This similarity in dosimetric indices was expected due to the fact that the two methods have very similar beam geometries. This suggests that the main benefits of this technique over VMAT are only in efficiency of delivery.

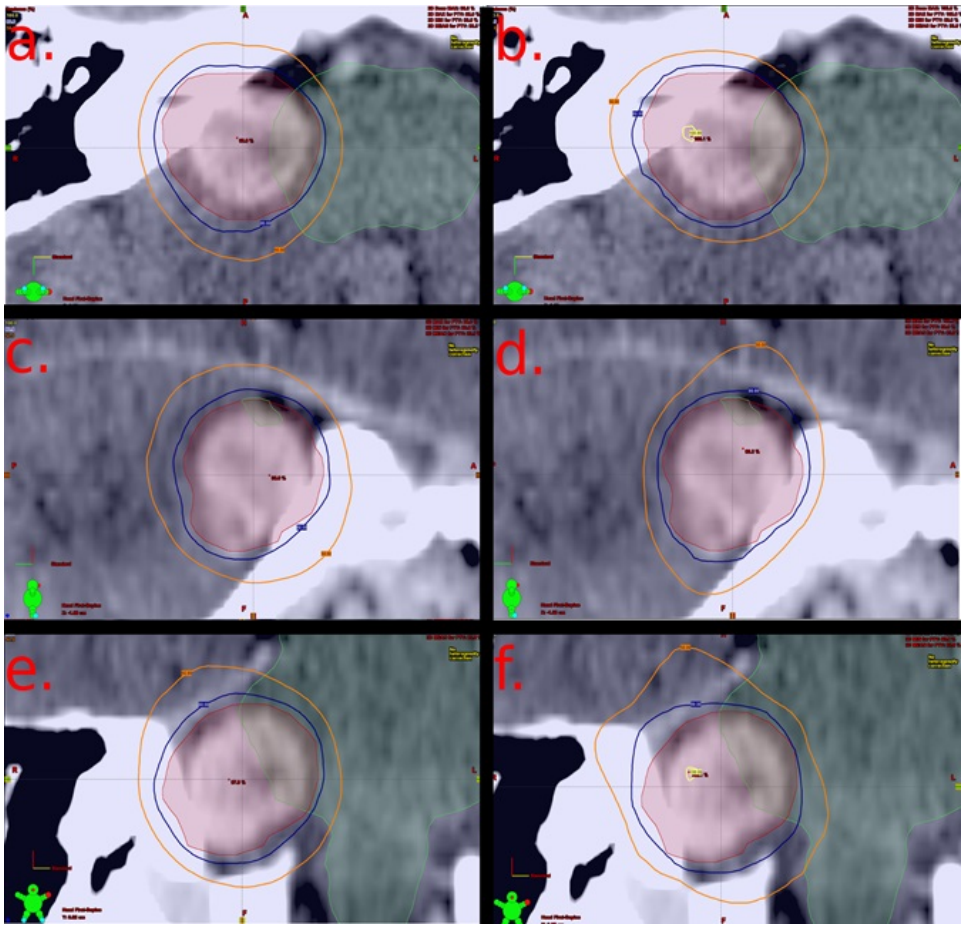

Figure 2.3: Dose distribution for patient 3 (right AN) for TVMAT (left) and DCA (right). The PTV contour (red) and Brainstem (green) are shown. In addition, dose distributions are shown by yellow (100%), blue (80%), and orange (50%) a,b. Transverse slices show the dose distributions look similar, but with the TVMAT plan able to slightly curtail the dose away from the brainsteam. c.d. Sagital slices show both plans were of similar quality. e.f. Frontal slices: both plans have similar falloff, however the DCA plan comes from a smaller subset of angles so one can see the artefacts of more jagged falloff lines.

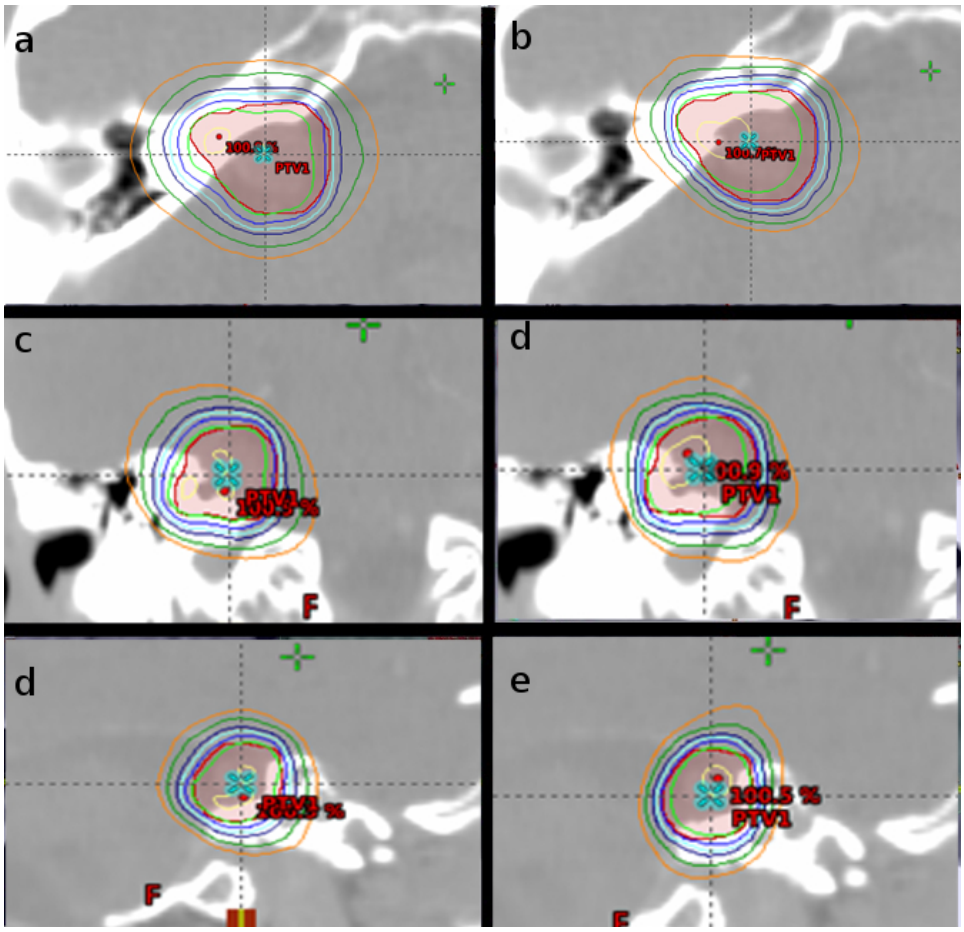

Figure 2.4: Dose distribution for patient 1 (right AN) for TVMAT (left) and DCA (right). The PTV contour is shown in red. In addition, dose distributions are shown by yellow (100%), blue (80%), and orange (50%) a,b. Transverse slices c.d. Sagital slices e.f. Frontal slices

2.3.2 Analysis of Trajectories

Figure 2.8 shows the impact of the number of partial arcs on the optimized cost for selected number of cases. In all test patients, the optimization algorithm found a cost minimum with fewer than eight partial arcs. This suggests that the eight arc plan adequately samples the phase space and fewer arcs can produce the plans with the same optimized cost values. In the case of the three AN patients, fairly

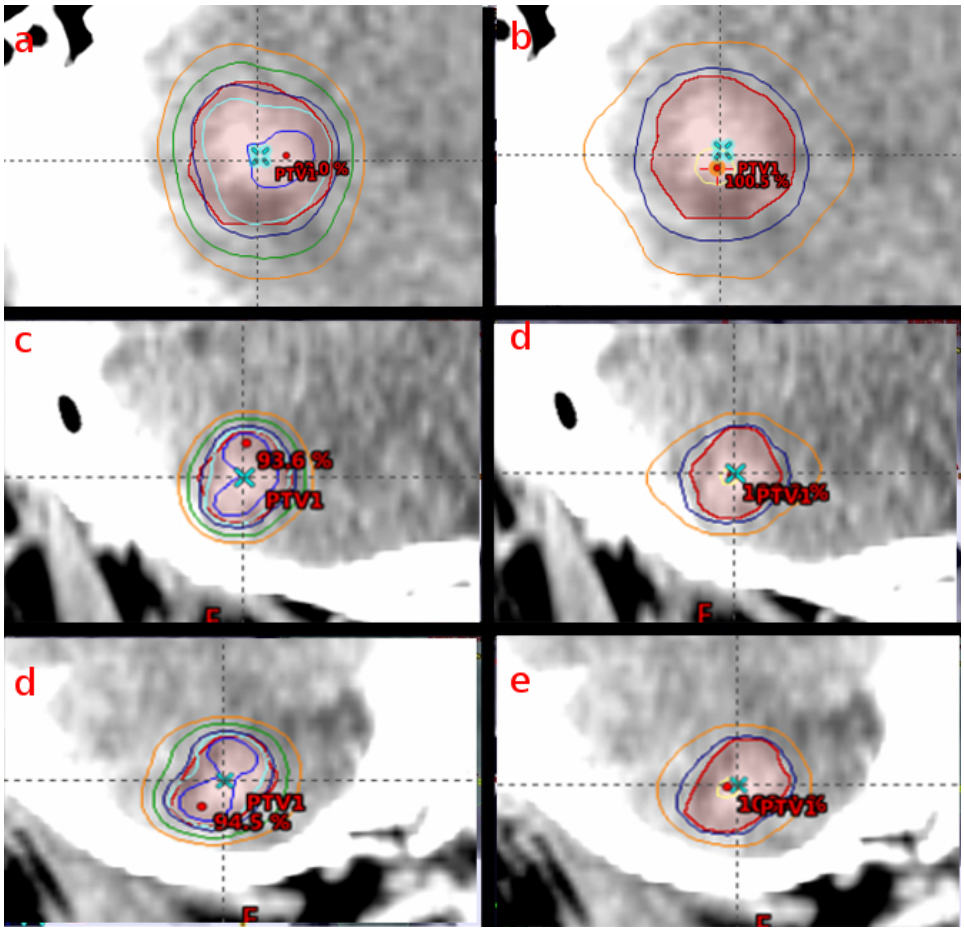

Figure 2.5: Dose distribution for patient 4 (right AN) for TVMAT (left) and DCA (right). The PTV contour is shown in red. In addition, dose distributions are shown by yellow (100%), blue (80%), and orange (50%) a,b. Transverse slices c.d. Sagital slices e.f. Frontal slices

reproducible results were observed patient to patient. In this subset of patients (Figure 2.8a) the cost showed a minimum value at four partial arcs. Certain variables (shown in Figure 2.8 b) were optimized with even fewer partial arcs. The falloff, conformity, and homogenity were minimized at two partial arcs. This trajectory corresponds to the one previously studied by Podgorsak [75]. In this trajectory, the gantry and couch both rotate at a constant velocity producing a baseball stitch pattern across the head. The Podgorsak trajectory reportedly produces a spherical

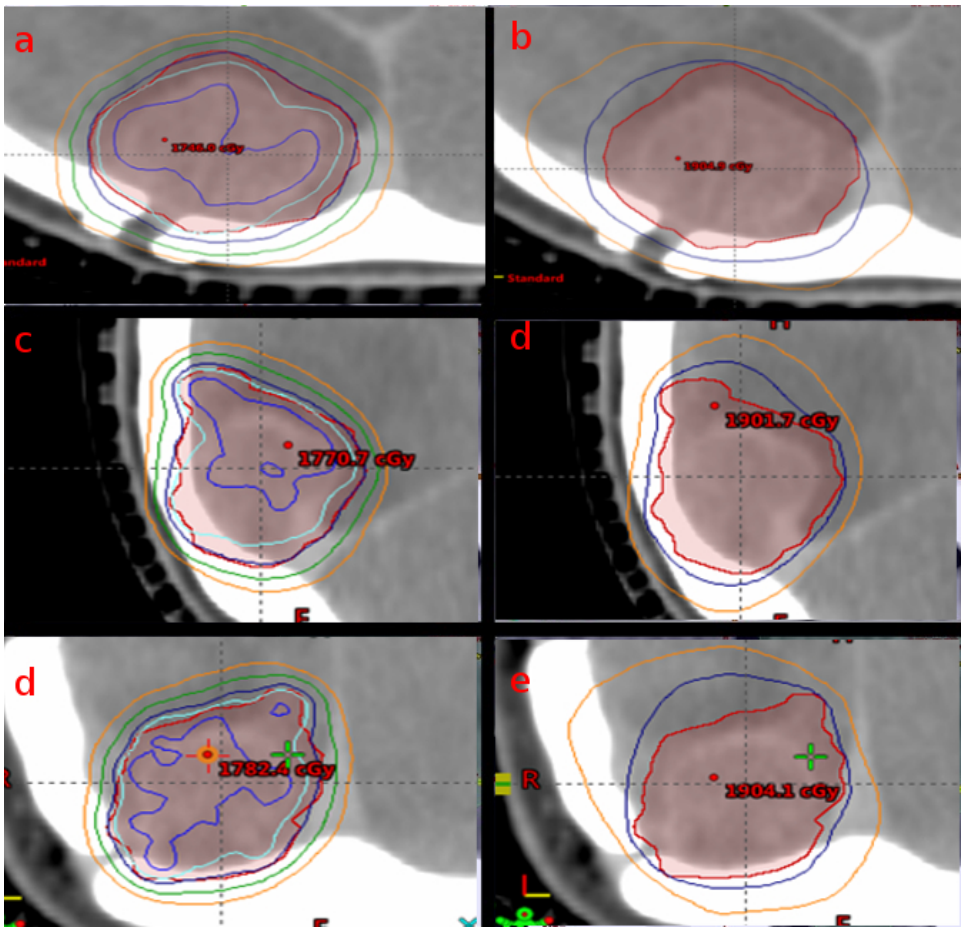

Figure 2.6: Dose distribution for patient 6, met 2 (Multiple Met) for TVMAT (left) and DCA (right). The PTV contour is shown in red. In addition, dose distributions are shown by yellow (100%), blue (80%), and orange (50%) a,b. Transverse slices c.d. Sagital slices e.f. Frontal slices

dose distribution with isotropic falloff [75].

While the falloff, conformality, and homogeneity were optimized with fewer partial arcs, the cost was minimized at four partial arcs for the AN patients. These deliveries had an adequate sampling of the phase space such that they could simultaneously avoid critical structures, while having enough entrance angles to provide falloff, conformity, and homogeneity.

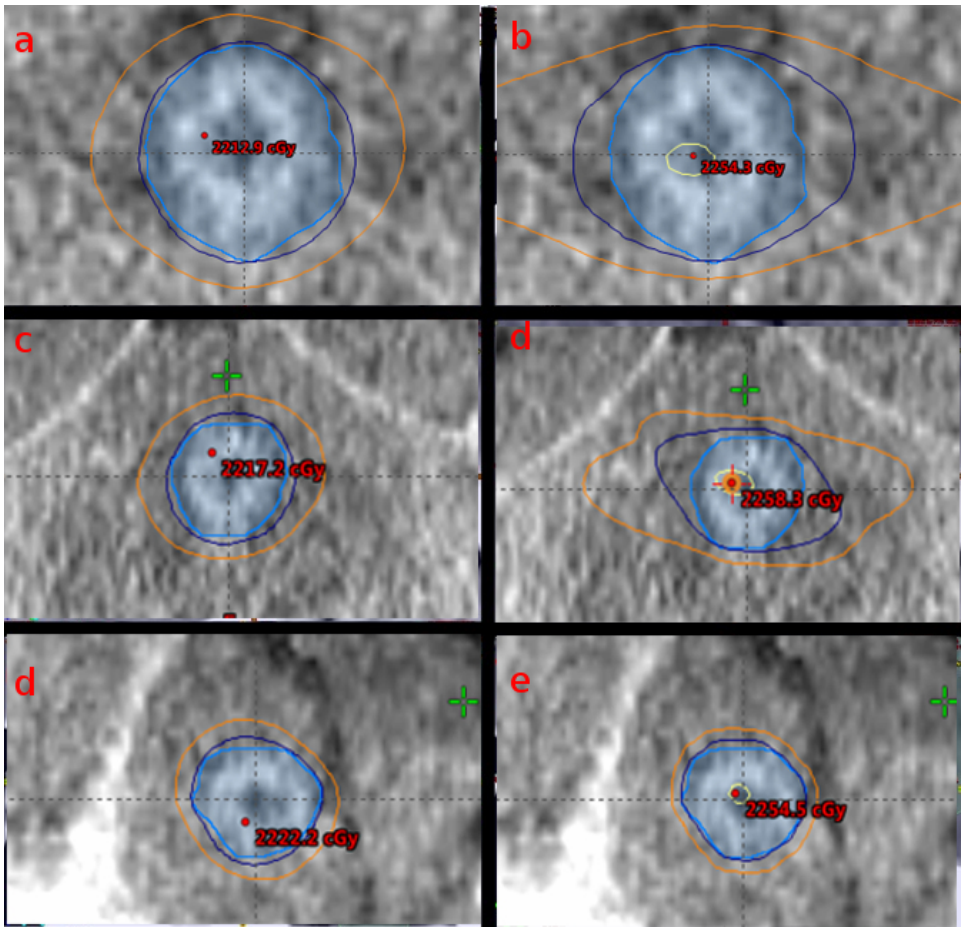

Figure 2.7: Dose distribution for patient 9, met 1 (Multiple Met) for TVMAT (left) and DCA (right). The PTV contour is shown in red. In addition, dose distributions are shown by yellow (100%), blue (80%), and orange (50%) a,b. Transverse slices c.d. Sagital slices e.f. Frontal slices

2.3.3 Treatment Time Comparison

The three AN patients (patients 1, 2 and 3 chosen arbitrarily) were used to compare the treatment time of the various methods. As is shown in Figure 2.8, plans for patients 2 and 3 found the global minimum at only three partial arcs while patient 1 needed four partial arcs. These treatments were used as the "optimized" sampling benchmark. A summary of the delivery time results are shown in Table 2.3. For

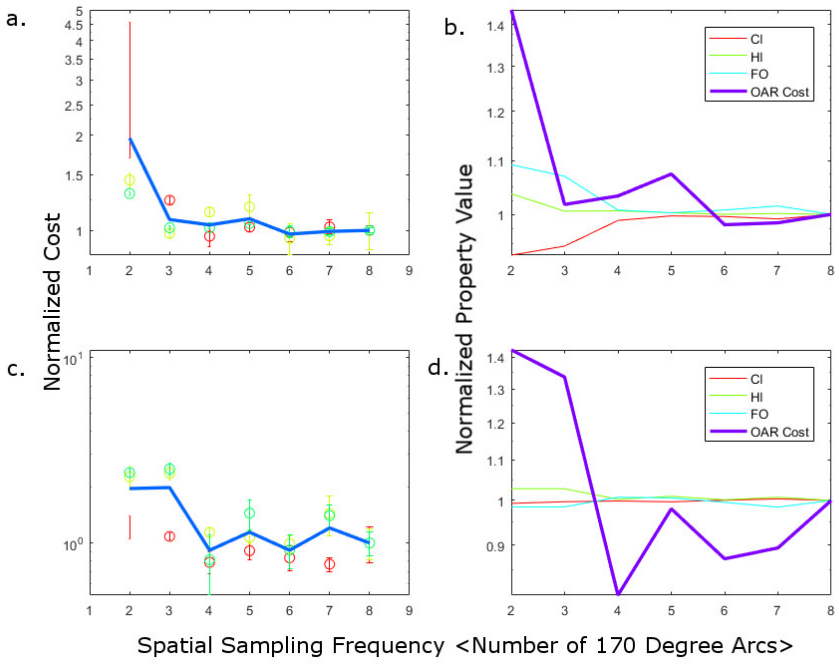

Figure 2.8: Analysis of the importance of trajectory on plan quality. Variables are normalized to the values achieved for the eight arc plans. a) The cost function depence on number of partial arcs for acoustic neuroma plans (patient 1, 2, 3 with data points shown in red, green, yellow respectively). The blue line corresponds to the trend in the TVMAT data and error bars correspond to standard deviations from three rounds of TVMAT optimization. b) Optimization of clinical variables of interest for the AN patients. c) Cost function for 2 Met patients. It showed a similiar pattern as the AN patients, however found a minimum at four partial arcs instead of three. d) Optimization of clinical variables for 2 Met Patients.

the 12 Gy SRS plans, the fully sampled trajectories (those with eight partial arcs) had an average delivery time of 357 seconds. When the sampling of phase space was optimized, we found an average delivery time of 294 seconds. The time to deliver 2 Gy at the maximum dose rate for the fully sampled trajectories was 233 seconds, while the optimized trajectories averaged 109 seconds. For large dose

Table 2.3: Beam-on time for competing optimization strategies.

	Radiosurgery (12 Gy)		Radiotherapy (2 Gy)	
Patient ID	Fully Sampled	Optimized Sampling	Fully Sampled	Optimized Sampling
1	338 s	289 s	232 s	123 s
2	370 s	305 s	233 s	103 s
3	363 s	289 s	233 s	102 s
Mean	357 s	294 s	233 s	109 s

per fraction, the dose rate will have a significant effect on treatment time. Linacs operating in 10 MV flattening filter free (FFF) can achieve a dose rate of 2400 $\frac{MU}{min}$. If the technique developed in this thesis were to be applied with a 10 MV FFF beam, then the relative treatment time reduction would be comparable to what is observed for the 2 Gy, 600 $\frac{MU}{min}$ treatment. Conversely, the DCA and VMAT treatments took between 720-900 s as they involved multiple high dose arcs (which each take approximately 2 minutes, and multiple couch kicks (which also each take 2 minutes).

2.3.4 Validation of Deliveries

The results of the dosimetric measurements for patients 1, 2, and 6 (chosen arbitrarily) are presented in Table 2.4. Isocentric ion chamber measurements were within 2% of measured values for all patients. Uncertainties were mainly attributed to uncertainties in small field delivery and the variation of the chamber response with beam angle. Film measurements provided dose distribution information which agreed well with the expected values. Sample dose distribution and profile data is shown in Figure 2.9. Dose distributions were compared with gamma analysis (Section 1.5.3) (2%, 2mm passing criterion) and achieved a 98% passing rate on average (Table 2.4).

For each of the subsequent deliveries, trajectory logs were collected. The recorded couch and gantry angle were compared with the expected couch and gantry angles. The root mean square deviation of these values were compared. Interestingly, the trajectory log recorded gantry and couch values were an order of magnitude closer to their expected values than the machines set tolerances.

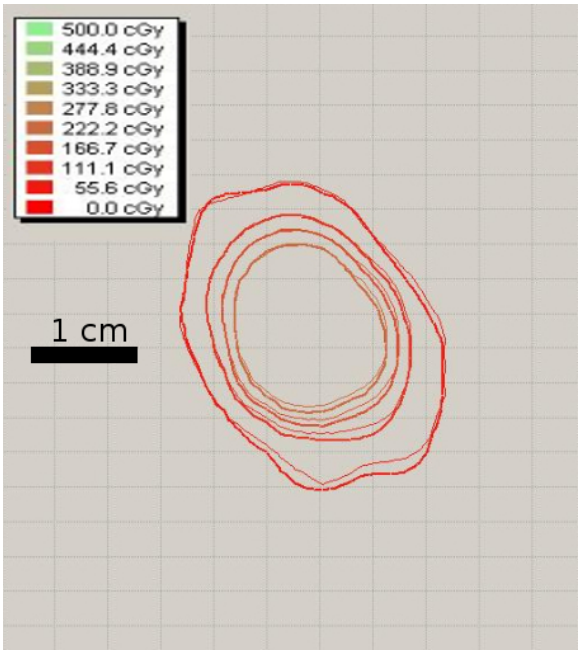

(a)

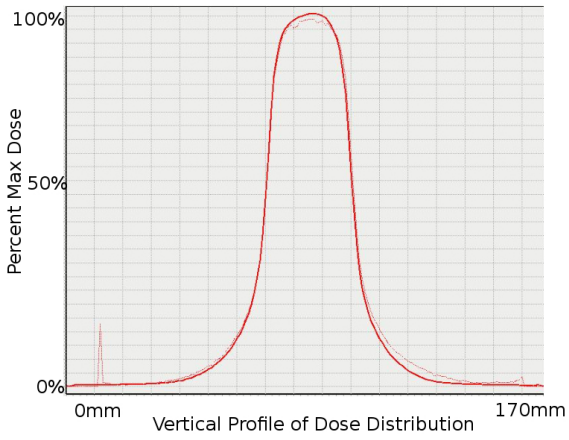

(b)

Figure 2.9: a. Dose distribution comparison in coronal plane (film (dotted line) vs treatment plan (solid line)) for patient 2. Plan was scaled to 1/5 of the actual value to have doses in the most accurate range for film measurements. b. Vertical profile comparison for the same treatment.

Table 2.4: Plan Quality Assurance Metrics

Patient	Isocentre Dose (cGy)			Gamma Analysis		Trajectory Log Analysis	
	AAA	Ion Chamber	% Difference	Coronal	Sagittal	Couch (RMSE)	Gantry (RMSE)
1	1340	1342	-0.1%	96%	100%	0.046	0.049
2	1434	1462	-1.9%	97%	99%	0.052	0.042
6.1	1473	1452	1.4%	96%	99%	0.048	0.050
6.2	1712	1675	2%	99%	98%	0.041	0.048

2.4 Discussion

The TVMAT technique presented here is an inverse planning method that produces an optimal treatment plan by using MLC and dose rate modulation along a pre-defined, over-sampled trajectory. Via dose rate modulation, the optimization technique indirectly determines an optimized beam trajectory by allowing beam delivery only for optimal beam entrance angles. Our preliminary treatment planning study has shown the dosimetric advantages of TVMAT when compared to the DCA technique due to the increase in conformity, homogeneity while maintaining falloff and OAR doses.

This method attempts to minimize patient discomfort and movement by constraining the device and treatment plan to have couch rotations in the same direction and, theoretically, have minimal inertial forces acted on the patient. This will be more comfortable and quicker than multiple static arcs, as the patient will have to undergo shorter treatments with fewer accelerations. However, while the deliveries in this study tried to limit the accelerations of the couch, the linac control system allows only for the specification of the location of the linacs degrees of freedom in the form of control points, leaving velocities and accelerations up to the control of the device. If one wanted to truly limit accelerations felt by the patient, linac manufacturers would need to release control of these features.

The treatment couch-isocentre wobble error can affect the accuracy of the TVMAT delivery technique and should be accurately characterized during commissioning of this technique. The couch-isocentre wobble error of the TrueBeam linac on which this study was conducted was less than 0.4 mm. While this error

is relatively small when compared with patient setup error, it should still be considered in the determination of the PTV margin. If couch-isocentre wobble error is a significant contributor to isocentre localization accuracy, then dynamic couch deliveries should not be conducted due to the inability to correct for these errors as one possibly could in static couch deliveries.

Some of this work is preliminary. Further improvements to the optimization method and a more comprehensive treatment planning study with larger sample sizes are needed to determine the full dosimetric benefits of this technique. Additional improvements of this method will incorporate single isocentre treatment planning for multiple metastases. However, for the single isocentre technique, accurate rotational accuracy in patient setup is of paramount importance as small rotational errors can result in large dosimetric errors when the PTVs are far from the isocentre [81]. Preliminary results presented in this paper in trajectory log analysis suggest that the machine delivery inaccuracies will be insignificant when compared to patient setup inaccuracies, however the accuracy of these trajectory logs have not been indepently verified and these results should only be used as a consistency check. Once implemented, these treatments will allow the treatment of larger number of targets (more than 3) [69] in a time efficient manner.

2.5 Conclusion

We have developed and validated a trajectory-based dose delivery method which has dose distribution improvements while having a treatment time of between 3 to 8 minutes. Additionally, it has the potential to make the way for a more efficient treatment planning process while maintaining an accurate delivery on the Varian Truebeam Linac.

Table 2.5: PTV and normal tissue statistics

Patient	CI			FO			HI			V12			V4		
	TVMAT	IDCA*	VMAT	TVMAT	IDCA	VMAT	TVMAT	IDCA	VMAT	TVMAT	IDCA*	VMAT	TVMAT	IDCA*	VMAT
1	0.80	0.70	0.76	2.8	3.00	2.9	1.19	1.13	1.21	4.03	4.6	4.18	21.7	22.6	22
2	0.65	0.62	0.72	3.2	3.00	3.1	1.29	1.23	1.25	7.8	8.0	6.9	45.5	38.3	39.7
3	0.81	0.70	0.78	2.60	2.90	2.66	1.23	1.26	1.27	5.6	6.5	5.86	28.8	31.4	28.8
4	0.63	0.61	0.69	3.76	4.00	3.55	1.25	1.23	1.22	3	10.0	2.9	17	51.8	14.2
5	0.76	0.70	0.82	2.60	2.66	2.4	1.21	1.34	1.22	15.5	15.7	14.4	67.2	78.6	61.3
6.1	0.67	0.69	0.71	3.17	2.70	2.8	1.26	1.26	1.22	40.0	42.5	38.8	210.9	205.9	201.1
6.2	0.77	0.65	0.73	2.50	3.12	2.52	1.20	1.29	1.21						
7.1	0.64	0.50	0.78	3.30	3.01	2.81	1.30	1.42	1.3	22.3	31.4	20	99.0	155.3	91.6
7.2	0.80	0.71	0.83	2.70	2.62	2.61	1.20	1.27	1.24						
8.1	0.98	0.91	0.71	2.03	2.10	2.7	1.19	1.33	1.22	21.0	20.9	23.37	113.3	147.0	110
8.2	0.64	0.64	0.59	3.50	3.25	3.5	1.18	1.27	1.17						
9.1	0.73	0.59	0.71	3.00	4.52	3.32	1.26	1.31	1.25						
9.2	0.71	0.64	0.62	3.45	3.23	3.33	1.22	1.30	1.23	22.1	25.8	22.5	134.9	242.1	157
9.3	0.73	0.62	0.70	2.99	3.34	2.94	1.20	1.25	1.19						
10.1	0.53	0.53	0.57	4.12	4.12	3.7	1.36	1.29	1.29						
10.2	0.65	0.55	0.68	4.35	4.88	4.00	1.30	1.21	1.27	18.0	19.8	16.6	113.6	165.8	101.1
10.3	0.55	0.49	0.60	5.13	6.06	4.96	1.22	1.27	1.22						

CI $\sim$ Conformity Index, FO $\sim$ Fall off, HI $\sim$ Homogeneity index, V12 $\sim$ The volume that receives 12Gy (in cc). V4 $\sim$ The volume that receives 4Gy (in cc). * shows statistical difference from treatment modalities.

Chapter 3

Machine-Specific Quality Assurance Procedure for Stereotactic Treatments with Dynamic Couch Rotations

3.1 Introduction

Modern linacs require accurate mechanical specifications to meet the needs of evolving precision techniques developed for SRS and SBRT. For SRS and SBRT techniques, the report of AAPM Task Group 142 [47] (TG142) recommends that the accuracy of the linac isocentre to be less than 1 mm and the couch rotational accuracy to be better than 1 degree. However, modern SRS treatments are becoming increasingly complex and leverage features that were not considered when TG142 was written. One such feature is the incorporation of single isocentre treatments for multiple brain metastases [16, 17, 38, 40, 69, 89]. These treatments have PTVs far from the isocentre where positional and rotational inaccuracies of the isocentre will manifest themselves in greater magnitude. Other technology not considered in the TG142 report include the use of dynamic couch rotations [26, 59, 76, 86, 96, 99] which require the accuracy of the linac to be maintained under rotations of the

couch while the beam is on. Additionally, trajectory logs can be used in the clinic to validate treatments [2, 88], however the couch angle recorded in these logs has not been validated in the static or dynamic case. Finally, as the accuracy of image guidance techniques continue to improve, more accurate couch-based QA methods need to be developed to guarantee that machine precision does not become a significant obstacle to the quality of treatments.

There are several methods developed to measure the linac isocentre. One of the most widely accepted methods is the star-shot method [23, 31]. This method involves placing radiosensitive film in the plane of rotation, exposing the film to narrow fields at different angles and measuring the fields' overlap. However, this method is labour intensive and lacks accuracy as field symmetry is assumed in the analysis. Another method is the Winston-Lutz (WL) method [58], in which a metal ball bearing (BB) is mounted on the treatment couch and precisely aligned with the linac isocentre. A series of images (film or portal) are taken at various gantry, couch and collimator positions to ascertain the isocentre localization error. While the WL method is a very reliable way of measuring the overall accuracy of the linac radiation isocentre, it cannot discern couch walkout (isocentre misalignment due to couch rotations) from errors due to mechanical misalignments of the gantry and beam collimation system (jaws or MLCs).

In this work, we present a method in which the isocentre localization accuracy is measured using a phantom which is comprised of five BBs. Using this phantom, we are able to quantify the linac's localization error due to couch walkout, quantify the accuracy of the trajectory logs, and quantify the linac's ability to maintain these accuracies with intra-treatment couch motion. These features will have special relevance in the quality assurance of the next generation of SRS treatment techniques that involve treatments of multiple targets with a single common isocentre and deliveries using dynamic couch rotations.

3.2 Methods

The couch isocentre accuracy of a Varian TrueBeam STx Linac (Varian Inc., Palo Alto, California) was evaluated using its EPID and a specialized phantom constructed for this study. The phantom is a polystyrene slab in which five stainless

steel BBs of 4 mm diameter are placed on the same plane. One BB is placed at the centre of the polystyrene slab, whilst the remaining four BBs are placed at varying radial distances and angles in the same plane (radii = 0, 2.8, 4.4, 5.6, and 6.7 cm for the five respective BBs). This phantom is shown in Figure 3.1. Multiple MV images of the phantom were acquired at varying couch angles. Algorithms were developed to characterize the couch rotational accuracy from the locations of the BBs identified in the images.

3.2.1 Set-up and Measurement

Figure 3.1 shows the phantom setup on the treatment couch with the BrainLab couch mount (BrainLab, Munich, Germany) which can accommodate 5 degrees of adjustment: tilt, roll, lateral, longitudinal and vertical directions. The phantom was positioned such that the plane of the BBs was horizontal, while the central BB was aligned with the room lasers defining the nominal linac isocentre. The gantry was in the vertical position, and a field size of 20x30 cm^2 was used to acquire images with a 6 MV beam operating at 600 MU/min. The EPID was positioned at the furthest distance from the source (182 cm) so as to achieve the highest spatial resolution possible.

Two treatment modes were considered in this study: static and dynamic delivery. For the static case, a total of nineteen EPID images were acquired using the "High Quality" MV imaging mode. This imaging method had a resolution of 1024x768 which translated to an image pixel size of 0.215 mm at the isocentre plane. Images were acquired every 10 degrees as the couch was rotated through its full range of rotation [-90°, 90°]. For the dynamic case, images were acquired using the"Continuous" imaging mode in which the MV image readout is synchronized with the pauses between beam pulses: the image is read out line by line until the entire image is acquired (at an approximate frequency of 7 Hz). This method has the same resolution and accuracy as the"High Quality" method, if one discounts pixel blurring introduced by movement of the phantom intra-image acquisition. In separate measurements, couch rotation accuracy at varying angular speeds was measured: max (3 degrees/s), half-max, and static were considered in this study.

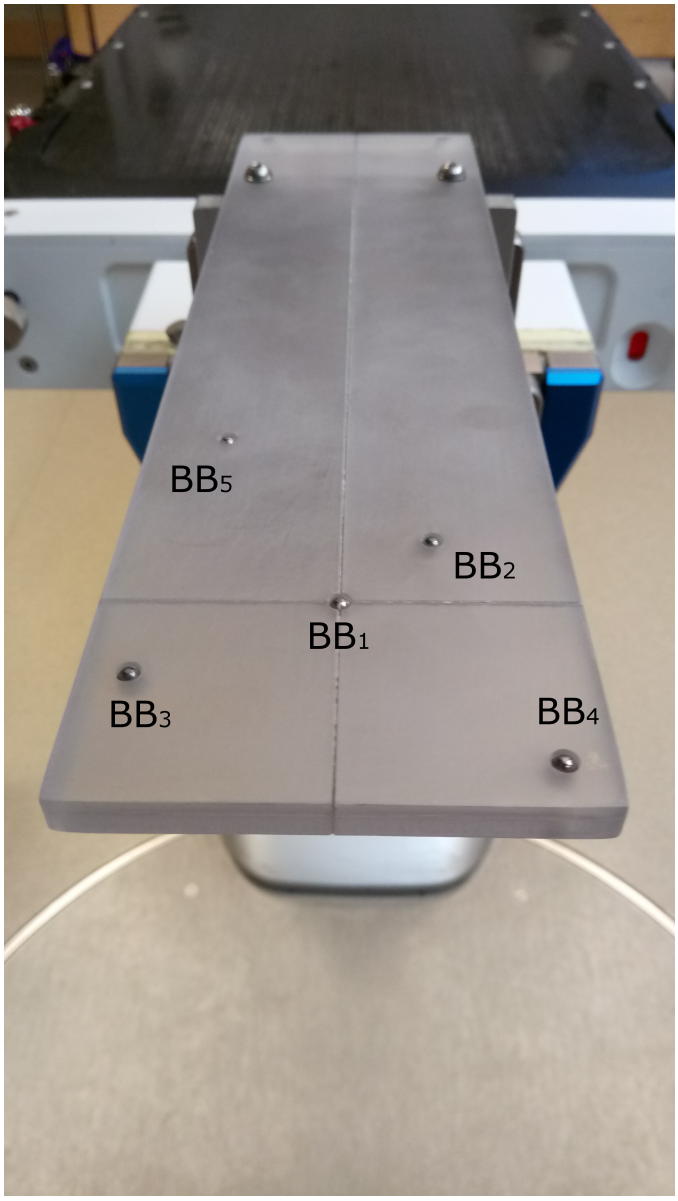

Figure 3.1: Aerial view of the BB phantom mounted to the treatment couch using the Brainlab couch mount. The phantom consists of five BBs ($BB_1 - BB_5$) affixed to a polystyrene slab. Each BB is located at different radial distance from the isocentre, with the central BB located at the isocentre. The linac is oriented vertically with the EPID deployed.

Table 3.1: Glossary of mathematical notation.

Symbol	Definition
A	The transformation matrix which represents the BBs' movement.
θ	The calculated couch angle for a given image.
$\vec{R_o}$	The calculated couch rotation centre in the xy plane.
S	The radial scaling factor which maximizes the overlap of the BBs between rotations.
$\vec{BB}_{i,\theta}$	The x,y coordinate of the i^{th} BB in the reference image for a given angle θ.
dR_x, dR_y and dR_z	The isocentre misalignment in the cross-plane, in-plane and out-of-plane directions.
$\vec{L}$	A horizontal line which extends from the nominal isocentre.
$\vec{L}_{SS}$	A calculated surrogate of the star-shot lines.

3.2.2 Data Analysis

The acquired images were exported in digital imaging and communications in medicine (DICOM) format and were loaded into in-house MATLAB (The Mathworks, Inc. Natick, Massachusetts) analysis software that was developed for this study. The analysis software was used for image segmentation, for localization of the BBs, and for calculation of the relevant geometric quantities. The location of each BB was identified in the collected imaging sets by first applying a threshold to the raw EPID images. The centroid of each BB in the thresholded image was then calculated and represents the BB location in our analysis.

Once BB locations were identified, fiducials were matched to one another using the radius from the centre as a unique identifier. Variables of interest were calculated using the BB locations as inputs. These variables, as well as all other notations, are listed in Table 3.1.

Determination of the Couch Rotation Centre

The location of the five fiducial markers at each couch angle were compared to the fiducial locations in the couch zero position. This comparison was conducted using a MATLAB implemented non-linear least squares optimization (MATLAB's lsqnonlin function) to find a representative transformation matrix (A) which encap-

sulates the rotation and translation information of the fiducials. This transformation matrix was constructed by minimizing the squared error between the fiducials using angle conserving scaling, rotations and translations. Mathematically, these transformations were represented as:

$$\begin{pmatrix} x' \\ y' \\ 1 \end{pmatrix} = A(S,\theta,\vec{R}_o) \times \begin{pmatrix} x \\ y \\ 1 \end{pmatrix} \tag{3.1}$$

$$A(S,\theta,\vec{R}_o) = \begin{pmatrix} 1 & 0 & R_x \\ 0 & 1 & R_y \\ 0 & 0 & 1 \end{pmatrix} \times \begin{pmatrix} Scos\theta & -Ssin\theta & 0 \\ Ssin\theta & Scos\theta & 0 \\ 0 & 0 & 1 \end{pmatrix} \times \begin{pmatrix} 1 & 0 & -R_x \\ 0 & 1 & -R_y \\ 0 & 0 & 1 \end{pmatrix} \tag{3.2}$$

where $\vec{R}_o = [R_x, R_y, 1]$ represents the couch rotation centre, S represents an angle preserving scaling factor, θ represents the calculated angle of couch rotation, $\vec{BB}_{i,0} = [x, y, 1]$ represent the cross-plane (x) and in-plane (y) coordinates of the i^{th} BB at couch angle 0, and $\vec{BB}_{i,\theta} = [x', y', 1]$ represent the cross-plane and in-plane coordinates of the i^{th} BB in the image acquired at a couch angle θ. The variables S, θ, and $\vec{R}_o$ were found such that the following constraint was minimized (an overview of this analysis is illustrated in Figure 3.2):

$$\underset{S,\theta,\vec{R}_o}{argmin} \sum_{i=2}^{5} ||\vec{BB}_{i,\theta} - A(S,\theta,\vec{R}_o)\vec{BB}_{i,0}||^2 \tag{3.3}$$

Once these parameters were found by least squares minimization, they were used to calculate variables of interest. Using the fact that the BBs lie in a plane, and the photon beam can be modelled as a divergent point source, the vertical offset was calculated:

$$dR_z = (1-S)D_{SAD} \tag{3.4}$$

where S is the scaling factor, dR_z is the isocentre vertical offset error, and D_{SAD} is the source axis distance, set to 100 cm for this study. The isocentre localization error in the xy plane can be calculated by applying the formula :

$$d\vec{R}_{xy} = \vec{R}_o - \vec{BB}_{1(\theta=0)} \tag{3.5}$$

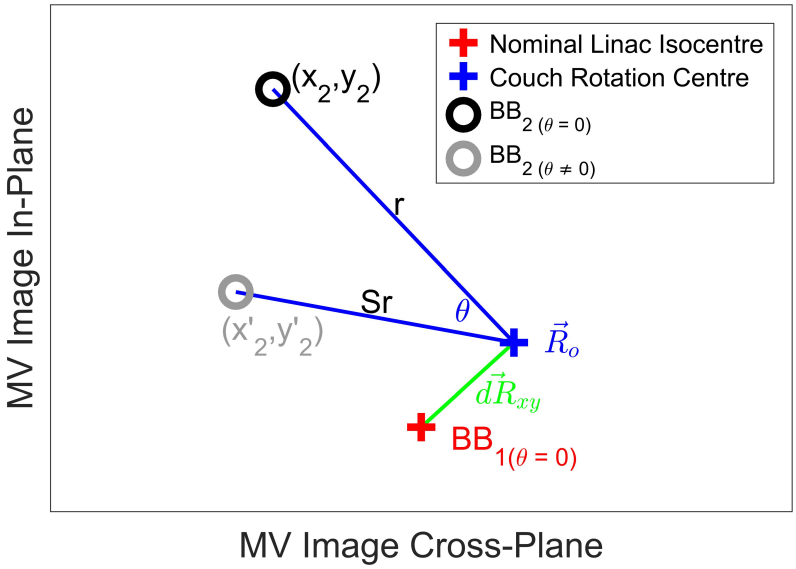

Figure 3.2: Illustration of the mathematical analysis for BBs 1 and 2. The nominal linac isocentre is shown as a cross (labelled $BB_{1(\theta=0)}$) and the initial BB_2 location is shown as a black circle (x_2, y_2). After rotation of the couch by a given angle, the movement of BB_2 (grey circle) can be represented as a rotation by angle θ about the centre of rotation (cross labelled by $\vec{R}_0$). Additionally, a radial scaling S about the centre of rotation accounts for any out of plane movements. $d\vec{R}_{xy}$ represents the difference between the nominal isocentre and the centre of rotation. Illustration not to scale.

where $\vec{R}_o$ is the couch isocentre calculated from the above methodology and $\vec{BB}_{1(\theta=0)}$ is the nominal linac isocentre, defined as the pixel location of the central BB at couch angle zero.

Comparison with Star-shot Method

Additional analysis was conducted in order to present the couch isocentre walkout in the same manner as is typically done in "Star-shot" analysis. We defined a line which projects horizontally from the isocentre:

$$\vec{L} = \vec{BB}_{1(\theta=0)} + [x, 0] \tag{3.6}$$

and then transform this line using the matrix A to find the equivalent "Star-shot" lines:

$$\vec{L_{SS}} = A\vec{L} \tag{3.7}$$

The "Star-shot" lines ($\vec{L_{SS}}$) were calculated for couch rotations in 30 degree intervals, the points of intersection between each line were determined and the circle which encompassed the points was found (see Depuydt et al. [23] for similar analysis). The mean intersection location and the centre and radius of the fitted circle were compared with film-based star-shot analysis using FilmQA Pro (Ashland Inc., Covington, Kentucky).

Winston-Lutz Method

An additional measurement was conducted in which both the WL and the multiple BB data were acquired in a single phantom setup. The WL measurement was performed by collimating a 1x1 cm^2 field with the linac MLC and by acquiring EPID images for every 10 degrees of couch rotation. This process was repeated with the gantry above the phantom (0 degrees), and below the phantom (180 degrees). For the WL analysis, the location of the central BB was compared to the field centre as defined by the midpoint of the field border. These deviations were compared to the couch isocentre misalignment values ($\vec{dR}_{xy}$) measured by the multiple BB analysis method.

Validation of The Trajectory Logs

The rotation angle (θ) extracted by the method discussed in section 3.2.2 provided a method for the validation of the couch angle in the trajectory log. Images were acquired while the couch moved dynamically and were subsequently exported in DICOM format. The DICOM image format provides each image with a time stamp and the expected couch angle in the header of the file. The trajectory log contains couch angle readouts recorded throughout treatment at a sampling rate of 50 Hz, however, it does not contain a time stamp to designate the beginning of data col-

Table 3.2: Accuracy of the developed methods.

Measurement (unit)	Accuracy (95 % CI)
$d\vec{R}_{xy}$ (mm)	0.07
dR_z (mm)	0.8
θ (degrees)	0.05

lection. At the beginning of each measurement, the couch was moved back and forth between positions -80, -90, and -80 degrees to produce a unique movement signature. The relation between the trajectory logs and the collected images was established by finding the time offset, dt, which minimized absolute difference between the couch angle values from the two datasets for this movement. Using this method, the couch angles calculated from the images could be related to the trajectory logs. Errors were quantified by subtracting the calculated couch angle of the acquired images, from the angle recorded in the trajectory log. This analysis was conducted for varying couch velocities: max couch velocity (3 degrees/s), half maximum velocity, and static deliveries.

3.2.3 Accuracy of the Procedures

The error of the BB localization algorithm was $\pm$ half a pixel along each of the imaging axes. The propagation of this source of error was calculated using a bootstrapping approach. Sample data (n = 1000) was created by transforming the setup BB locations about the isocentre by a known angle. These fiducial locations were then displaced by a normally distributed random error with mean zero and standard deviation of 0.25 pixels. The methodology of the previous sections was conducted, and the calculated values were compared to the expected values and the error was reported as the 95% confidence interval of the resultant distributions. The accuracy of each calculated parameter is presented in Table 3.2. As can be seen, this phantom is very well suited for quantifying xy offsets ($d\vec{R}_{xy}$) as well as rotational errors (θ). Conversely, the least accurate measurement is the dR_z, offset which has an accuracy of 0.8 mm.

Table 3.3: Couch rotation centre offsets with respect to the nominal linac isocentre in the cross-plane, in-plane, and out-of-plane directions (mean $\pm$ 2 standard deviations).

Data Set	Cross-Plane (mm) (x)	In-Plane (mm) (y)	Out-of-plane (mm) (z)
Trial 1	0.3 ± 0.2	-0.2 ± 0.3	-0.1 ± 0.6
Trial 2	0.3 ± 0.1	-0.7 ± 0.3	0 ± 0.8
Trial 3	0.3 ± 0.2	-0.2 ± 0.3	-0.1 ± 0.6

3.3 Results

3.3.1 Determination of the couch rotation centre

Measurements were taken at three distinct time points. The cross-plane (x), in-plane (y), and out-of-plane (z) isocentre position errors (section 3.2.2) were quantified for three unique datasets and are plotted against rotation angle in Figure 3.3. Summary statistics such as mean value and standard deviation are summarized in Table 3.3. As can be seen, the three trials have mean and standard deviation that overlap and are therefore statistically indistinguishable, with the exception of the second trial's in-plane measurement, which contained an offset of 0.5 mm from the other two measurements. As the room lasers were not realigned in the measurement period, the most reasonable explanation for this result is an inter-measurement variability of phantom setup.

3.3.2 Comparison with the Star-shot Method

The couch star-shot lines were calculated using the method described in Section 3.2.2. A plot of the treatment couch star-shot lines (Equation 3.7) for dataset 1 is shown in Figure 3.4. The figure also contains a plot of the smallest circle encompassing all the intersection points (blue circles) of the star-shot lines. The minimum inscribing circle had a radius of 0.34 mm, while the deviation of the center of the circle with respect to the nominal linac isocentre had a magnitude of 0.14 mm (0.08 mm and 0.12 mm in the cross-plane and in-plane directions respectively). The film scan, as well as the output analysis, are shown in Figure 3.4 c and d. The star-

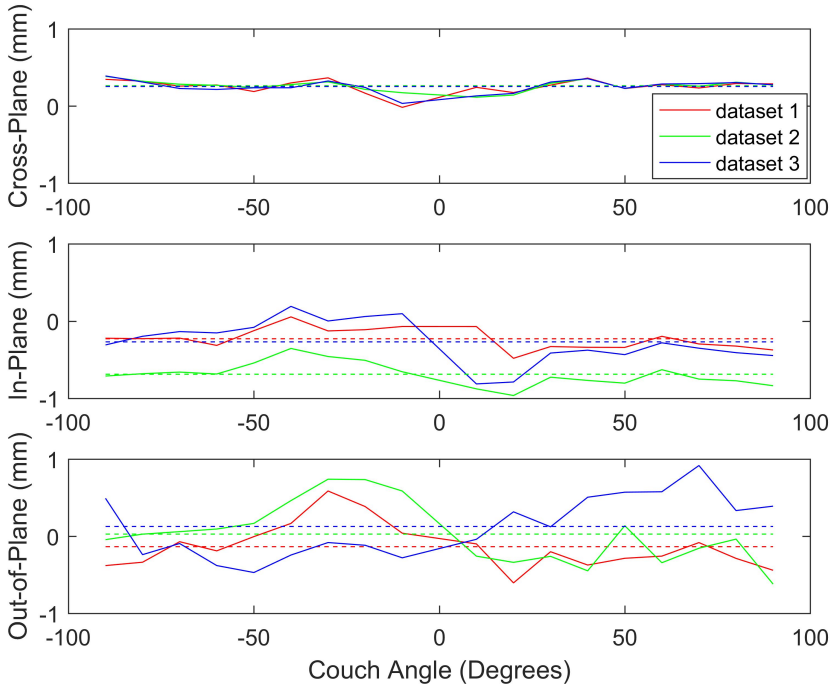

Figure 3.3: Deviation of couch centre of rotation as a function of angle calculated using the analysis in Equation 3.5. Dataset 1, 2 and 3 represent three independent measurements acquired one month apart. The solid line represents the data plotted for each couch angle (sampled every 10 degrees) while the dotted line represents the mean of each dataset, averaged over all of the measured couch angles.

shot measurements summarized in Table 3.4 are given as the radius of the smallest circle inscribing all of the points of intersection of the star-shot lines, the distance between the linac isocentre and the centroid of the intersection points, the distance between the linac isocentre and the centre of the circle and the average rotational errors. As can be seen in Table 3.4, the two methods agreed within 0.2 mm for isocentre localization and 0.3 degrees for rotation calculations.

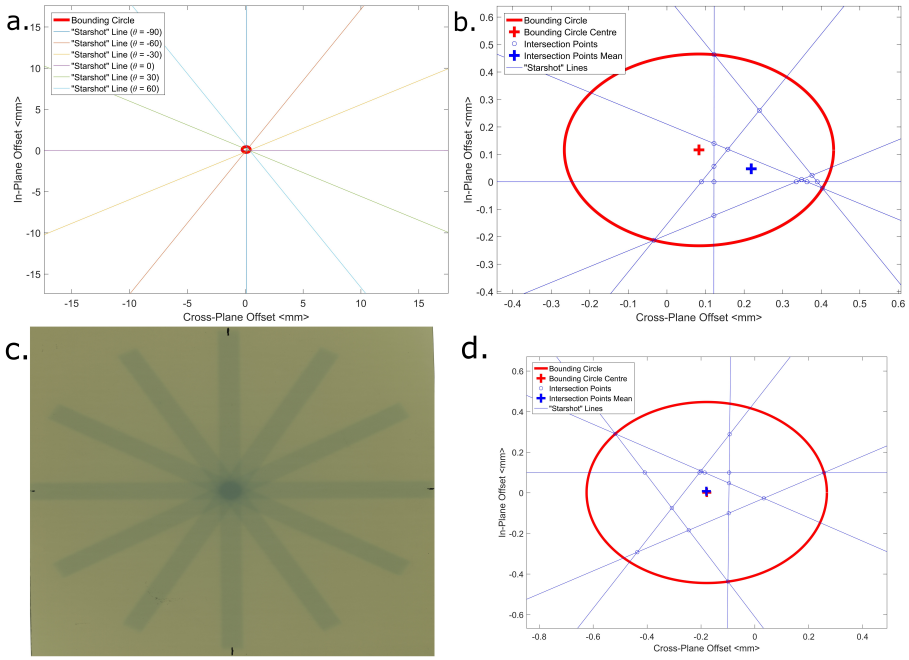

Figure 3.4: a. The lines represent the calculated EPID based star-shot lines sampled every 30 degrees of couch rotation. The circle which bounds the intersection of these lines is shown. b. Magnified version of figure a. The origin (0, 0 mm) represents the nominal linac isocentre. The lines represent calculated star-shot lines, and the intersection points of these lines are shown as circles. The bounding circle is the smallest circle which encapsulates all of the intersection points. The two crosses represent the centre of the circle and the centroid of the intersection points. c. Raw GafChromic film data collected for traditional star-shot analysis. d. Fitted star-shot lines and bounding circle for the film data.

Table 3.4: Comparison of film-based with EPID-based star-shot measurements.

Analysis Method	BB Phantom	GafChromic Film
Radius of Circle	0.34 mm	0.5 mm
Centroid Distance to Nominal Isocentre	0.22 mm	0.20 mm
Centre of Circle Distance to Nominal Isocentre	0.14 mm	0.2 mm
Rotation Error	0.05 degrees	0.3 degrees

3.3.3 Winston-Lutz Method

The in-plane and cross-plane deviations obtained from the WL measurements and the corresponding couch rotation deviations obtained from the multiple BB measurements are shown in Figure 3.5. The WL deviations were (mean $\pm$ 2 standard deviations) -0.4 $\pm$ 0.3 mm and 0.4 $\pm$ 0.3 mm in the cross-plane and in plane directions when measurements were taken with the gantry above the phantom while they had a measure of 0 $\pm$ 0.3 mm and 0$\pm$ 0.3 mm when the gantry was below the phantom (IEC 61217). Conversely, the couch rotation centre deviations from multiple BB analysis were 0.2 $\pm$ 0.1 mm and -0.1 $\pm$ 0.3 mm in the cross-plane and in-plane directions for both gantry orientations (IEC 61217). It is interesting to note that unlike the WL measurements, the multiple BB analysis results were independent of the gantry orientation and measures only the stability of the couch rotation axis, separate from the mechanical features of the gantry.

3.3.4 Validation of the Trajectory Logs

Data were collected with the couch rotated at its maximum velocity (3 degrees per second), half maximum velocity, and static. For the couch moving at its maximum velocity, images were acquired continuously, and 489 data points were collected. There were eight images from which we could not extract BB location information as the intensity of the beam changed intra-image acquisition. These data points are shown as magenta crosses in Figure 3.6. The couch angle recorded in the images were aligned with the trajectory logs in the time domain, and once aligned, the mean absolute difference between the trajectory log recorded couch angle with the angle in the header file was 0.002 degrees. There was no pattern observed between rotational error and couch position, and errors were randomly distributed around zero (Figure 3.6). Figure 3.6 shows the pairwise differences between the trajectory log (θ_T), header file (θ_H), and calculated (θ) couch angle for dynamic couch movement at the couch's max velocity (3 degrees/s). The difference between the trajectory log and the calculated value was within measurement error of $\pm$ 0.05 degrees in the dynamic case. Similarly, for the static case, the difference between the trajectory log and calculated value was 0.02 $\pm$ 0.04 degrees (mean $\pm$ 2 standard deviations). The analysis was repeated for the couch moving at half maximum

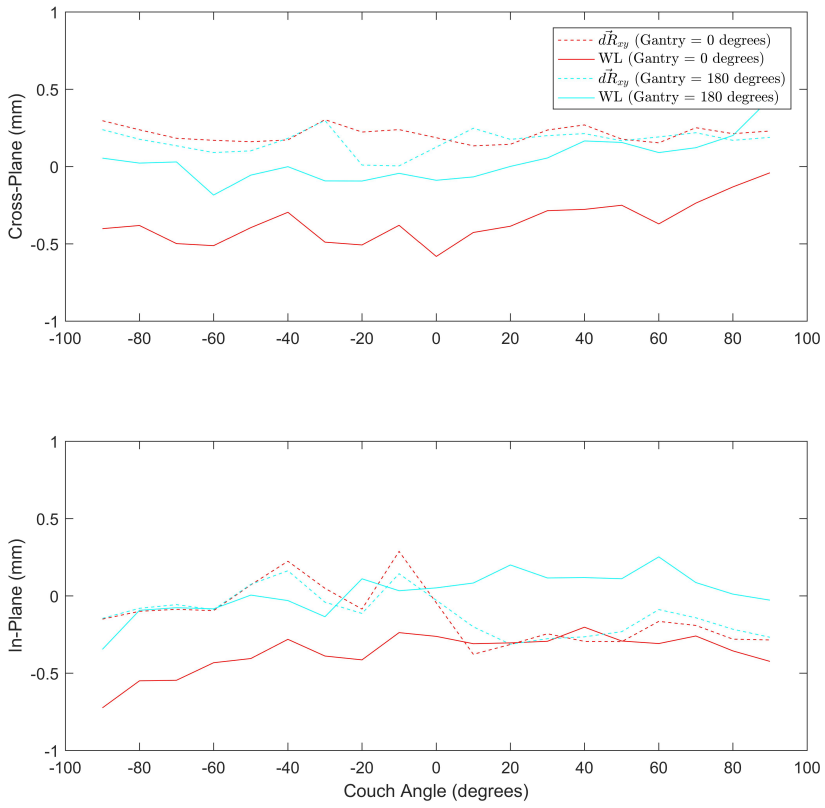

Figure 3.5: Cross-plane and in-plane deviations obtained from the multiple BB method and the Winston Lutz method measured in a single phantom setup. The dashed lines represent the couch rotation centre deviations (dR_x, dR_y) obtained from the multiple BB measurement, and the solid lines represent the Winston Lutz deviations. Measurements were acquired for two gantry positions, 0 degrees (above phantom), and 180 degrees (below phantom).

velocity, resulting in a localization error of 0.05 ± 0.04 degrees. This suggests that the linac was able to maintain its rotational accuracy even while the couch moved intra-treatment for varying couch velocities.

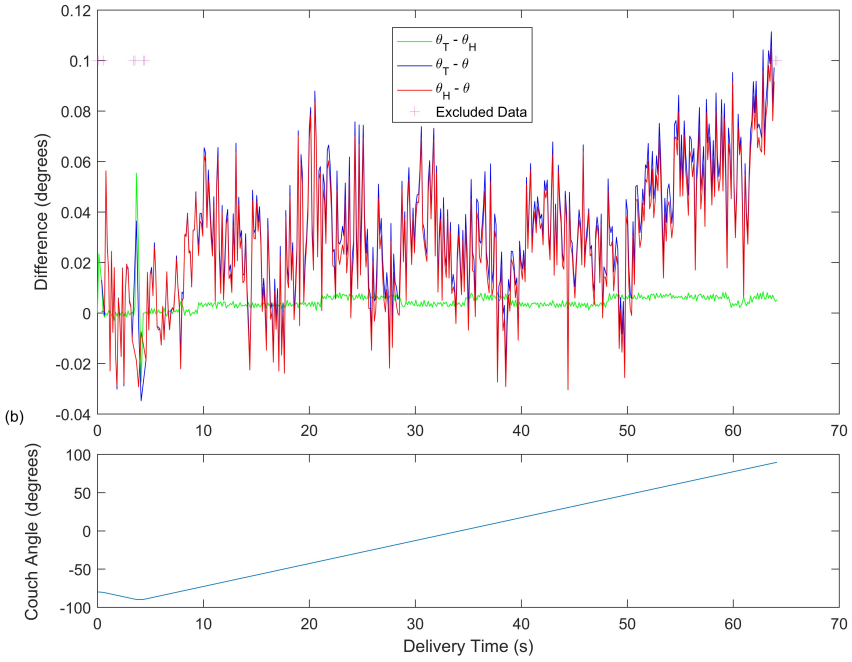

Figure 3.6: (a) A plot of the differences between the couch angles recorded by different methodology as the couch rotated through -80 $\rightarrow$ -90 $\rightarrow$ +90 degrees at its maximum velocity over the course of 64 seconds (y axis) . The trajectory log couch angle values (θ_T) agreed with those recorded in the DICOM header files (θ_H) to the third significant digit. Additionally, the couch values recorded in the trajectory log and DICOM header (θ_T and θ_H respectively) agreed with the calculated values within 0.08 degrees. These errors were normally distributed with mean 0 and standard deviation 0.025 degrees. Crosses show eight data points which were excluded from image analysis due to intra-imaging changes in beam intensity. (b) The couch angle position as a function of delivery time.

3.4 Discussion

In this study, a new EPID-based QA method is proposed for the treatment couch. The method is simple, accurate, and enables the user to access a multitude of complementary data with a single measurement. Of particular interest is this method's ability to simultaneously quantify the couch walkout in three dimensions, as well as the couch rotational accuracy. These tests can be conducted efficiently due to ease of set up and analysis. When compared to the traditional film-based star-shot technique, the method proposed here offers several advantages. First, it is simpler in terms of setup and analysis as it does not require film. Second, it is more accurate since it does not depend on the accuracy of the field symmetry. When comparing this method to the WL method, it provides explicit values of the couch rotational accuracy in three dimensions, and WL measurements can be performed for the same set-up using the central BB. Additionally, while the work presented here is focused on the treatment couch, similar methods can be directly applied to collimator and gantry rotational measurements. These properties will be of increased importance for single isocentre treatment of multiple metastases for which rotational errors can result in untreated regions of the PTV.

Recently, trajectory-based techniques in which there is dynamic motion of the couch and gantry have been developed for SRS and breast treatments [59, 76, 86, 96, 99]. These treatments would require synchronous couch and gantry rotation during delivery. One way of performing patient-specific quality assurance of such deliveries is by comparing the trajectory log data with the trajectory from the treatment plan. Before using the trajectory log data for this purpose, it is important to verify its accuracy. The methods to acquire the accuracy of the trajectory log with regards to MLC [2] and gantry rotation [62] have been developed by other groups. In this work, we presented a method for the validation of the couch angles that are recorded in the trajectory log files. By conducting this method on our centre's TrueBeam linac, we have demonstrated that the couch angular positions recorded in the trajectory logs are accurate to within 0.05 degrees. Furthermore, these errors did not seem to depend on the couch angular velocity. This suggests that the treatment couch tested in this work is accurate enough for dynamic couch treatment techniques reported recently [53, 59, 76, 86, 96, 99].

Some proposed delivery techniques [53, 59, 76, 86, 99] require accelerations of the couch intra-treatment. In our study, when the couch accelerated, the intensity of the beam changed intra-image, resulting in poor quality EPID images. The thresholding method used for locating the BB positions was not able to reliably find all of the BBs in these images, making it impossible to compare the calculated couch angle (θ) with the couch angles from the trajectory log and EPID image header. More robust imaging analysis techniques would need to be developed to extend the analysis for cases when the couch does not move at a constant velocity. Additionally, the difference between the couch angle values extracted from the trajectory log and the EPID image header could be significantly larger in the couch acceleration region ($\sim$0.04 degrees) when compared with those when the couch moved at constant velocity ($<$0.01 degrees). However, this difference is still an order of magnitude smaller than a clinically significant rotational error [81].

The mean treatment couch isocentre offset was localized to be 0.3 $\pm$ 0.2 mm and -0.2 $\pm$ 0.3 mm in the cross-plane and in-plane orientations respectively away from the nominal isocentre. This is due to the nominal isocentre being calibrated to the isocentre of gantry rotations on this particular machine. For smaller errors, the room lasers would need to be recalibrated somewhere in-between the mechanically defined gantry and couch isocentre.

Whilst the measurement of the couch walkout in the z direction is novel, it was shown to be the least accurate measurement in this work (with accuracy of $\pm$ 0.8 mm). However, this method may still be capable of demarcating linacs which would either pass or fail the TG 142 criteria of 1 mm at the treatment isocentre if its accuracy is improved. Future work could improve this accuracy by having more points farther from the beam central axis (which will decrease the standard error on the calculated parameters) or by taking image sets at non-coplanar beam geometry.

3.5 Conclusions

We have developed an EPID based quality assurance method for the treatment couch which is simple, accurate, and enables the user to access a multitude of complementary data with a single measurement. Using this method, we have shown that the TrueBeam treatment couch that was studied is accurate for both static and

dynamic stereotactic deliveries.

Chapter 4

Collimator Optimization for VMAT Treatments of Multiple Brain Metastases

4.1 Introduction

VMAT optimization was introduced by Otto [71] as a DAO approach in which the linac gantry moves intra-treatment. This method was shown to be time-efficient and effective at reproducing dosimetric indices for certain static field IMRT geometries [78]. However DAO is a non-convex optimization approach and is more susceptible than IMRT to incorrectly returning local minima after optimization. One such treatment site where this frequently happens is the treatment of multiple brain metastases with SRS. For these treatments, MLC contention issues (explained in Figure 4.1) provide multiple local minima in the cost function which reduce the fidelity of the optimization[98]. It has been proposed that these shortfalls may be mitigated by incorporating collimator optimization in the form of static collimator optimization [98] or dynamic collimator trajectory optimization [55, 60].

In a landmark clinical trial by Brown et al. [13], SRS alone was shown to have similiar survival outcomes, but better cognitive function when compared with SRS with whole brain radiotherapy (WBRT) adjuvant therapy. Furthermore, American

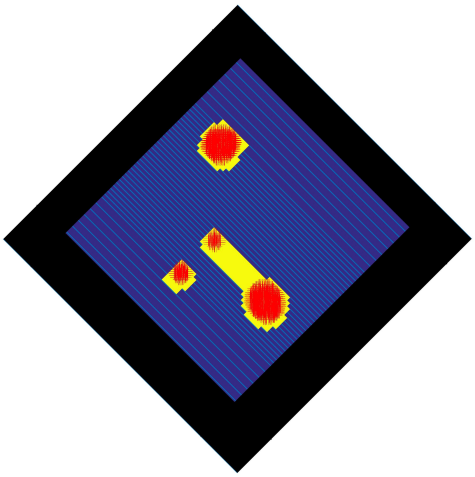

(a)

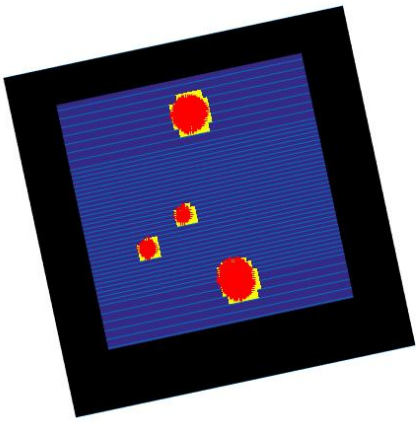

(b)

Figure 4.1: An example of MLC contention issues that may arise in the treatment of multiple PTVs with a single aperture. PTVs are shown in red, normal tissue is shown in yellow, the MLC is shown in blue and the field jaws are shown in black. (a) Collimator is rotated to 45 degrees and the MLC aperture is set to conform to the targets. A sizeable amount of normal tissue is being irradiated. (b) The optimal collimator angle occurs at -12 degrees. When the aperture is set to conform to the targets, the normal tissue is efficiently blocked by the MLC.

Table 4.1: Summary of Patient Statistics

Patient Number	Prescription Dose (Gy)	Number of Mets	Total Volume (cc)
1	40/5	7	5.8
2	40/5	6	3.2
3	35/5	4	7.3
4	40/5	4	3.2
5	35/5	4	5

Society for Therapeutic Radiation Oncology (ASTRO) recommends "to not add adjuvant whole brain radiotherapy for stereotactic radiosurgery of limited brain metastases" [27]. However, SRS without adjuvant therapy increases the probability of recurrence, and through this, the need for an increased number of salvage treatments. These salvage treatments can be difficult to plan due to the constraints set by QUANTEC [9], in particular limits on dose to normal brain, which has been correlated with radionecrosis. Hence, it is important that SRS treatments that do not have added adjuvant therapy should reduce the dose bath as much as is possible to enable future salvage treatments.

This work focuses on this goal by incorporating collimator trajectories into DAO-VMAT treatments. It explores different optimization strategies with the hopes of reducing the dose bath. The strategies explored are (i) treatment planner-selected static collimator, (ii) algorithm-optimized static collimator, and (iii) algorithm-optimized dynamic collimator.

4.2 Methods

4.2.1 Patient Selection

Five multiple brain metastasis patients who were treated at BC Cancer in 2017 were selected for this study. The patients had between 4-7 metastases treated, and an overview is provided in Table 4.1. The patients were treated with a Varian TrueBeam STx linac equipped with a Varian HD120 MLC. The clinical planning protocol uses two-three VMAT arcs planned using Varian Eclipse, with collimator angles selected by the treatment planner.

4.2.2 Collimator Angle Optimization Method

The collimator angle was optimized pre-VMAT optimization using a heuristic objective function function:

$$A_{OpenFluence} = A_{jaw} - A_{MLC} \tag{4.1}$$

where $A_{OpenFluence}$ is the are of open fluence; A_{jaw} is the area of the jaw opening; A_{MLC} is the area blocked by the MLC. The area of PTV would be considered as it was a constant of integration in the shortest path optimization. This function was the area of open fluence when the MLC is initialized to conform to the PTV. For each MLC pair, the MLC would conform to the maximum extent of the projection of the PTV onto the MLC plane.

The area of open fluence greatly depended on collimator angle as shown in Figure 4.1 which shows two conformal MLC configurations for two possible collimator angles. For each possible collimator-gantry combination, the MLC was fit to the structures and the area of open fluence was calculated. The optimal trajectory through collimator-gantry phase space was found using dynamic programming.

The method of trajectory optimization was adapted from Locke and Bush [55], with a few modifications to constrain the collimator movement and to force the gantry motion to be on the typical single 360 degree arc trajectory. During the collimator trajectory optimization process, the collimator rotation velocity was set to be at maximum 6 degrees per second while the gantry's velocity was set to 3 degrees per second. This extra constraint on the collimator velocity (whose hardware limit is 15 degrees per second) was set in order to ensure the operational accuracy of the progressive sampling algorithm (see Section 4.2.4 for more information). The shortest path was found between all collimator angles at gantry -180 to all collimator angles at gantry +180. This was calculated using Dijkstra's shortest path algorithm, where each node of the path were collimator-gantry coordinates (discretized in a grid of 2 degree spacing), and each link between nodes was defined by the the constraints of the linac movement.

4.2.3 Treatment Plan Cost Function

The main goal of this work was to create a cost function whose minima represented a viable treatment plan, and then ascertain the ability of the optimization strategies to produce this treatment. We accomplished this by using a simple cost function that was based on the clinically delivered plans. We formed the cost function by using the original clinical plans as a template for the optimizations, with an added reduction to the dose bath by the expected amount (30% reduction in low dose bath) proposed by implementing collimator optimization [98]. The cost function is given by:

$$\begin{aligned} C = \sum_{structures_i} w_i \int H_1(D(v) - c(v)D_0(v))^2 dv + \\ \sum_{targets_i} w_i [\int H_2(D(v) - P_{min})^2 dv + \int H_3(P_{max} - D(v))^2 dv] \end{aligned} \tag{4.2}$$

where P_{min} is the prescription minimum dose; P_{max} is the prescription maximum dose; $D(v)$ is the DVH achieved in the optimization step; $D_0(v)$ is the DVH from the original plan; c is the clinical out-performance factor, set to 1 for the high dose region and to 0.7 for doses lower than 12 Gy (decided based on insight from [98]); w_i is the weight of each organ, set to the volume of the structure for OAR and to 1000 for targets; and H_1 is the Heaviside function which equals to 1 when $D(v) - c(v)D_0(v)$ is positive, and 0 when $D(v) - c(v)D_0(v)$ is negative. H_2 and H_3 similarly represent the Heaviside function, but with $D(v) - P_{min}$ and $P_{max} - D(v)$ as their respective inputs.

4.2.4 Direct Aperture VMAT Optimization

Single, couch zero, 360 degree arc VMAT plans were optimized using an in-house MATLAB (The Mathworks, Massachusetts) implementation of the progressive sampling method described by Otto [71]. Control points were evenly spaced along the pre-defined gantry trajectory (or gantry-collimator trajectory if it was a dynamic collimator treatment). Initial control points were initialized with conformal apertures and equal MU weighting such that the PTVs received at least the prescription dose. While flattening filter free beams have been shown to be equivalent

to flattened beams for VMAT treatments, a 6 MV beam was used in this study. Doses were calculated for each control point using an in-house implementation of the pencil beam convolution algorithm. Doses were calculated for beam apertures, and these apertures were optimized using perturbation methods. Initially, MLC leaves were individually perturbed and if the perturbation decreased the cost function, then the new position was kept. Perturbations were sampled from the uniform random distribution with a width initially set to the full width of available MLC positions (given mechanical constraints), and was linearly decreased as the optimization progressed. Throughout optimization, additional control points were successively added in-between the initial control points along the designated trajectory. These control points were initialized as the linear interpolation of the MLC and beam-weights of the neighbouring control points. This sampling was continued until the entire trajectory was an accurate approximation of a continuous trajectory (200 control points per 360 degree arc). As a final optimization step, beam monitor units were optimized using projected gradient descent (constrained to positive monitor units).

4.2.5 The Blocking of Fluences Incident on Normal Tissue

In order to measure the dosimetric effect of the MLC contention issues on the optimized treatment plans, we recalculated the trajectory optimized plans using an idealized MLC model. In this idealized model, the MLC would have no leakage and would be able to completely block the radiation to normal tissue that lies between two PTVs. In this calculation, we recalculated the trajectory optimized plans with the PBC algorithm, however we blocked the open fluence when it did not overlap with the PTV (plus a 5 mm margin to ensure target coverage was not affected). Once each beam was recalculated, the beam intensities were re-optimized to ensure that the target dose was sufficiently covered (to account for scatter contribution of the blocked fluences).

This method provided a measurement of the quality of the treatment plan that could be achieved when there were no MLC contention issues. While this a theoretical limit, the plans created by this method would be dosimetrically equivalent multiple single isocentre deliveries with a dynamic collimator set to conform to

each of the PTVs for each pass of the delivery. This style of treatment is technically feasible (and therefore provides a good dosimetric treatment goal), however, it is cumbersome to deliver when there are more than three lesions.

4.2.6 Treatment Plan Comparison

All treatment plans were calculated and compared with the same pencil beam convolution (PBC) calculation algorithm. A randomly selected prospective treatment plan was recalculated using Varian AAA and the dose distributions were compared using (2%, 2 mm) gamma analysis criterion [22] with 20% dose thresholding. The PBC algorithm had a 98 % pass rate and the algorithm was deemed accurate enough for plan-to-plan comparison.

Treatment plans were compared on the basis of optimized cost, Vx, the volume that received x dose or more in Gray, mean brain dose, and Paddicks conformity index (CI) (elaborated in Equation 1.12).

4.2.7 Quality Assurance of Dynamic Collimator Delivery

The feasibility of dynamic collimator treatments was tested by developing a machine-specific QA technique that measured the collimator rotation intra-treatment with the EPID. This technique is similar to the method developed for QA of dynamic couch delivery introduced in Chapter 3. The MLC configuration (illustrated in Figure 4.2) produced a rotationally asymmetric MLC pattern that could be used to calculate the angle of rotation from EPID images. EPID images were acquired in "continuous" readout mode for which images are read out line by line at an approximate frequency of 7 Hz. Our centre's Varian TrueBeam linac (Varian Medical Systems Inc., Palo Alto, USA), operating in developers mode, delivered a 6 MV beam at 600 MU/min, while the collimator rotated intra-treatment.

Similar to the methods developed in Chapter 3, the collimator angle was obtained from three different measurements: the EPID image DICOM header file (θ_{header}), the trajectory log (θ_{log}) and from an EPID based measurement (θ_{calc}). θ_{calc} was calculated by using intensity-based registration between the images collected at a given angle and the EPID image collected at collimator angle zero. The registration was conducted by finding the affine transformation that used ro-

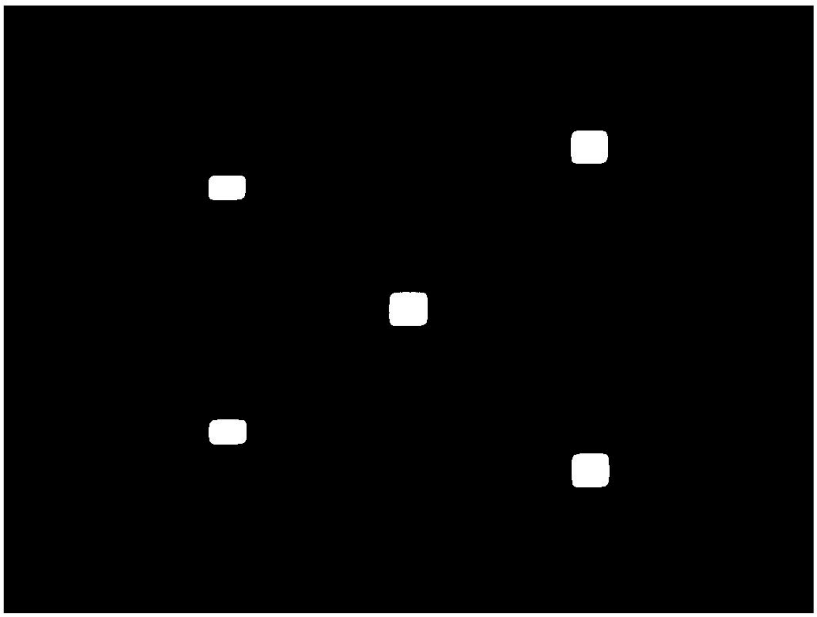

Figure 4.2: MLC aperture used in machine-specific quality assurance of collimator rotation. The MLC forms 5 square openings, three of 1 x 1 cm^2 and two of which are 1 x 0.5 cm^2. The central square provides the location of the isocentre, while the farther spaced openings provide an accurate rotational measurement.

tation and translation to best fit the EPID intensity maps. This registration was conducted using MATLAB's (The MathWorks Inc., Natick USA) lsqnonlin optimization function.

The EPID header and trajectory log provided information which was not aligned in the time domain: The EPID image header contained a time stamp, while the trajectory log collected collimator angles continuously at a 50 Hz sampling rate. These sources of information were aligned by rotating the collimator clockwise and then counter-clockwise to produce a unique movement, and then aligning the two signatures with a time interval dt that minimized the squared error between the data sources. Once aligned in the time domain, the rotational QA data was collected. Comparison between angles was conducted for each EPID image, where

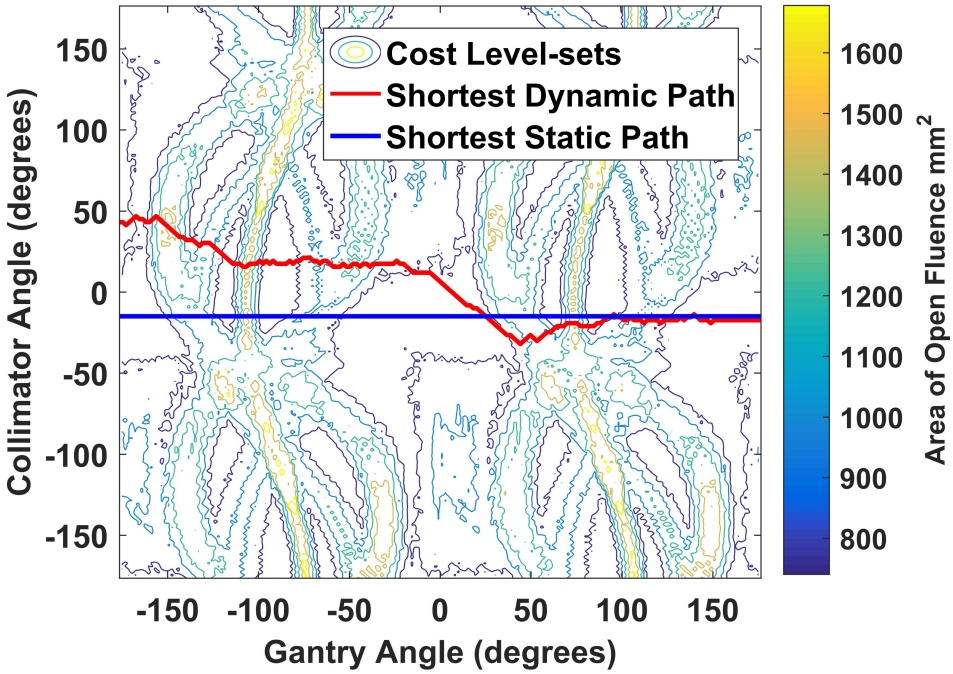

Figure 4.3: A typical area of open fluence level set graph derived from patient 3. The red line shows the global optimal path length through the graph, while the blue line represents the static angle which minimizes the graph (at -15 degrees).

trajectory log values were found by linear interpolation of the time series.

4.3 Results

4.3.1 Collimator Optimization

The area of open fluence function varied with both couch angle and collimator angle. A typical collimator-gantry cost function level set is shown in Figure 4.3 for patient 3. This figure shows both the shortest path found using dynamic programming as well as the optimal static collimator angle (which occurs at -15 degree). As an example (for the same patient), the optimal trajectory had a mean open fluence of 18 cm^2, while the algorithm-optimized static and treatment planner-selected

Table 4.2: Average area of open fluence when optimized with three techniques: optimized moving trajectory, optimized static angle, and treatment planner-selected angle.

Patient	Optimized Trajectory	Optimized Static	Treatment Planner-Selected
1	25 cm^2	29 cm^2	32 cm^2
2	17 cm^2	18 cm^2	24 cm^2
3	18 cm^2	19 cm^2	22 cm^2
4	12 cm^2	13 cm^2	16 cm^2
5	11 cm^2	11 cm^2	12 cm^2

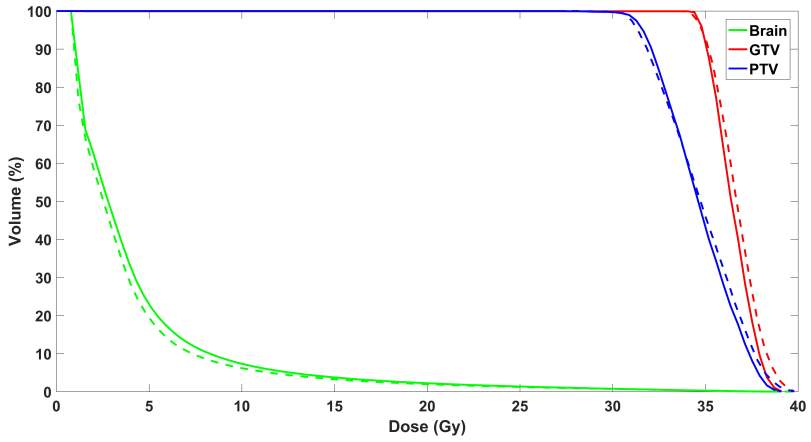

Figure 4.4: A DVH comparison for patient 3, which shows the difference in brain dose (shown in green) between the treatment planner-selected collimator angles (plan shown with solid line) and the trajectory optimized collimator angles (shown as a dashed line). The GTV and PTV doses shown are the summed dose for all four targets.

static angle had a mean open fluence of 19 cm^2 and 22 cm^2, respectively. A summary of the optimized fluence area for the different patients is given in Table 4.2.

4.3.2 Treatment Plan Comparison

A typical DVH comparison between a treatment planner-selected collimator angle and the trajectory optimized collimator angle plan is shown in Figure 4.4. As

Table 4.3: Comparison of treatment of dosimetric parameters for four optimization strategies: algorithm optimized static collimator, algorithm optimized trajectory, planner-selected static collimator (PS-Static) and normal tissue blocked.

	Patient Number	1	2	3	4	5	Mean
CI	Optimized Static	0.73	0.84	0.65	0.91	0.90	0.81
	Trajectory	0.74	0.84	0.76	0.92	0.92	0.84
	PS-Static	0.72	0.80	0.75	0.85	0.88	0.80
	Normal Tissue Blocked	0.76	0.83	0.74	0.92	0.91	0.83
V5 (cc)	Optimized Static	589	152	383	306	141	314
	Optimized Trajectory	637	154	378	307	141	323
	PS-Static	830	157	451	358	155	390
	Normal Tissue Blocked	524	144	295	249	125	267
V12 (cc)	Optimized Static	174	74	73	89	35	89
	Optimized Trajectory	166	75	75	88	33	87
	PS-Static	174	73	88	99	37	94
	Normal Tissue Blocked	148	72	70	84	34	82
Mean Brain Dose(Gy)	Optimized Static	5.6	1.7	4.4	4.1	2.7	3.7
	Optimized Trajectory	5.7	1.7	4.4	4.1	2.8	3.7
	PS Static	6.5	1.7	4.9	4.5	2.9	4.1
	Normal Tissue Blocked	4.9	1.6	3.8	3.4	2.2	3.2

can be seen, collimator trajectory optimization resulted in a small reduction in the low-dose bath to the brain. A dose distribution comparison of the same patient when compared to the clinically delivered plan is shown in Figure 4.5. While the DVH curve for normal brain does not appear to change significantly, the brain is a large organ when compared to the PTV and small differences between the curves, correspond to large volumes of unnecessarily irradiated tissue. This is quantified in Table 4.3, which shows treatment planning indices between the four methods. As can be seen for patient 3, the methods developed produced a 73 cc reduction in V5 when compared to the planner-selected static collimator method.

Both methods, static and dynamic collimator optimization, outperformed the planner-selected collimator angles in low-dose bath (V5). This is well illustrated in Figure 4.6a, which shows the mean relative improvement in V_x of the two methodologies when compared to the treatment planner-selected collimator plans. These comparisons were conducted after simulated annealing optimization step and one

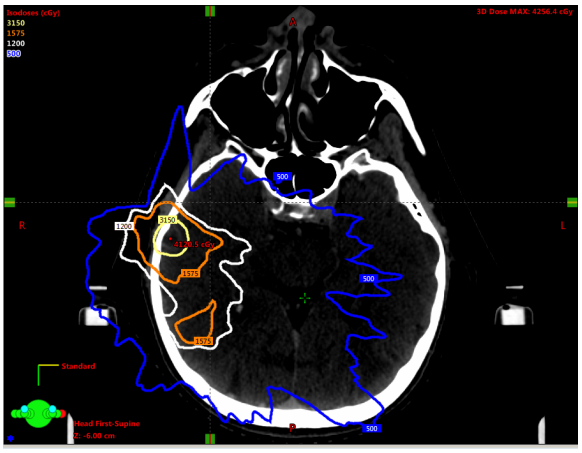

(a)

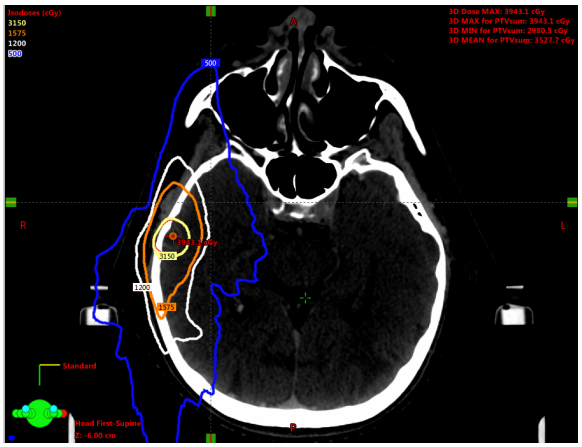

(b)

Figure 4.5: An example dose distribution comparison between the treatment planner-selected plan and the collimator trajectory optimized treatment plan. The prescription dose (3150 cGy), 50% (1575 cGy), 1200 cGy and 500 cGy contours are shown in yellow, orange, white, and blue respectively. a) The clinically delivered plan has significant dose spillage of the 5 Gy contour into the brain. b) Using the algorithms presented (both collimator angle optimization and MLC sequencing algorithms), the low-dose bath was significantly reduced.

can see a noticeable improvement of the collimator trajectory over the optimized collimator angle. Treatment beam-weights were then optimized using gradient descent with the beam shapes which were produced by the simulated annealing optimization. When this was conducted, the difference between the two methodologies disappeared, however both methods still outperformed the treatment planner-selected collimator angle (shown in Figure 4.6b). Figure 4.6b also shows the low-dose bath for plans which have the normal tissue dose blocked. This provides a good measure of the dose bath produced by the MLC either from fluence leakage through the MLC or from MLC contention issues. One can see that if these issues were mitigated, a further 15 percent improvement in low-dose bath could be achieved.

Throughout all conducted optimizations, the competing strategies were optimized with the same cost function which was derived from the clinically delivered treatment plans (as explained in Section 4.2.3). When we compared the treatments plans based on this metric, where a low cost value is seen as a "good" treatment plan, then we found that both collimator angle optimization, and collimator trajectory optimization consistently outperformed or reproduced the quality of the treatment planner-selected angle (shown in Figure 4.7).

The collimator angle optimization methods failed to improve the 7-met treatment plan (patient 1) and also made little improvement on the 6-met plan (patient 2). For these treatments, due to the large number of PTVs, it was physically impossible to find a collimator angle that removes the contention issues. This was most apparent in patient 1, where treating the patient without the open fluences produced by MLC contention, would have reduced the mean brain dose by 0.7 Gy. A DVH comparison for this patient, between the fluence blocked plan and the trajectory optimized plan is shown in Figure 4.8.

These improvements came with modest benefits on the conformity. The conformity index (mean $\pm$ one standard deviation) for the clinically recreated plans (0.80 $\pm$ 0.1) was similar to the optimized static collimator (0.80 $\pm$ 0.06) and dynamic collimator (0.84 $\pm$ 0.08) plans. The effect of optimization strategy on conformity index are summarized in Figure 4.9.

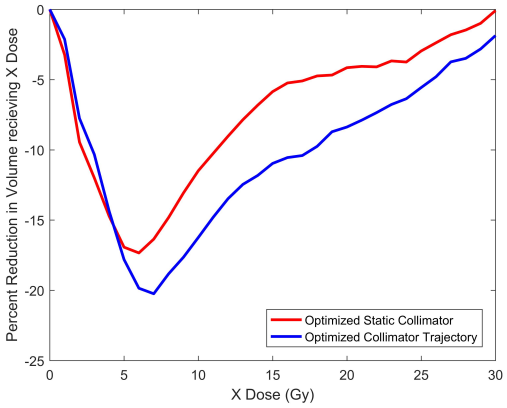

(a)

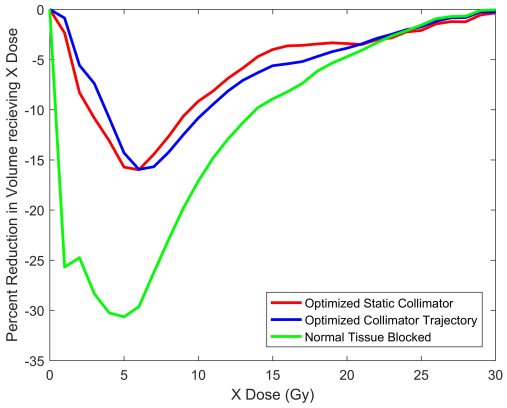

(b)

Figure 4.6: (a) The mean percent reduction in volume recieving x dose (Vx) from the implementation of collimator optimization methods when compared to the treatment planner-selected collimator angle. These results are presented after simulated annealing optimization. The optimized collimator angles (red) and collimator trajectory (blue) are compared with the treatment planner-selected collimator angle. Values are averaged for all patients considered in this study. (b) At the end of simulated annealing optimization, beam-weights were optimized using gradient descent. Treatment plans after gradient descent are shown in this graph, and one can see that the difference between the two methodologies disappears while the effect of collimator angle optimization still exists. The green line shows the affect of blocking fluences which do not overlap with PTV tissue.

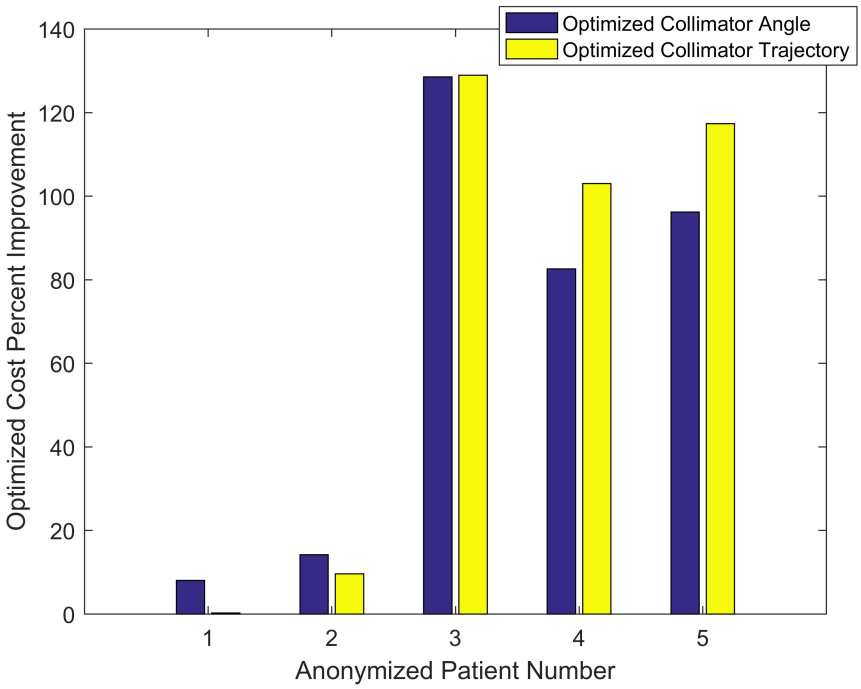

Figure 4.7: Improvement on the optimized cost for patients when compared with the clinically selected collimator angles. As can be seen, both strategies, the static algorithm optimized collimator angle and the optimized collimator trajectory, produced plans with lower cost function evaluations (i.e. higher optimization cost percent improvement).

4.3.3 Quality Assurance of Dynamic Collimator Delivery

A total of 500 images were collected while the collimator rotated dynamically over the 65 second QA test. Figure 4.10 shows the stability of the collimator rotational accuracy throughout this delivery. The three pairwise differences (mean $\pm$ 2 standard deviations) between the DICOM header recorded collimator angle (θ_{header}), trajectory log angle (θ_{log}), and calculated collimator angle (θ_{calc}) were 0.04 $\pm$ 0.06 degrees ($\theta_{calc} - \theta_{header}$), 0 $\pm$ 0.04 degrees ($\theta_{log} - \theta_{header}$), and 0.04 $\pm$ 0.06 degrees ($\theta_{calc} - \theta_{log}$). The maximum lateral displacement introduced by the collimator rotation was 0.1 mm, which is not likely to significantly affect the treatment dosimetry. These results suggest three things. First, the Varian Truebeam linac on

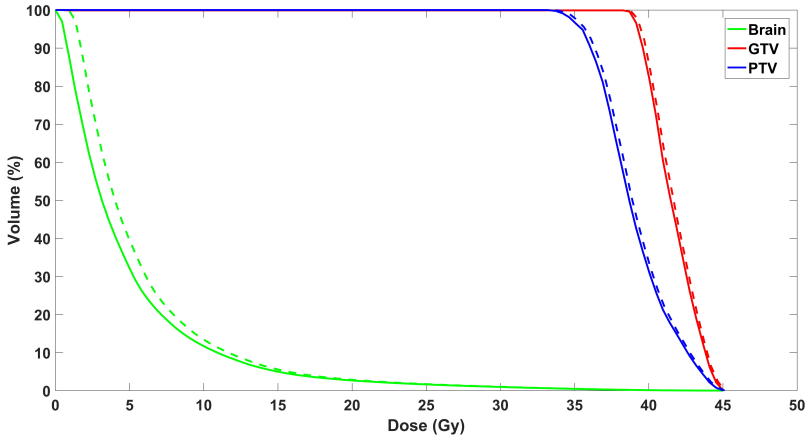

Figure 4.8: DVH comparison between the trajectory optimized collimator angle (shown as dashed lines) and the normal tissue blocked beams (shown as solid lines) for patient 3. The brain dose was higher in the trajectory optimized collimator plans.

which this test was performed can accurately rotate the collimator intra-treatment. Second, the trajectory logs' recorded collimator angle is accurate, and can be used in patient-specific QA. Third, machine-specific collimator QA can be deployed in a test that takes less than 2 minutes.

4.4 Discussion

DAO-VMAT has been shown to be a clinically viable treatment planning approach. It has been well adapted at many centres and can be used to create clinically equivalent plans for many treatment sites. If DAO-VMAT is to remain a standard of care, then methods should be implemented to ensure the unnecessary treatment of normal tissue is minimized by selecting the best collimator angle. In this work, we reproduced the results of Wu et al. [98] and show that manual selection of collimator angles can lead to enhanced MLC contention issues. Additionally, we showed that an algorithm-based approach for collimator angle selection can produce noticeable improvements, most of which comes from optimizing the static collimator angle. The equivalence between the static and trajectory optimized collimator an-

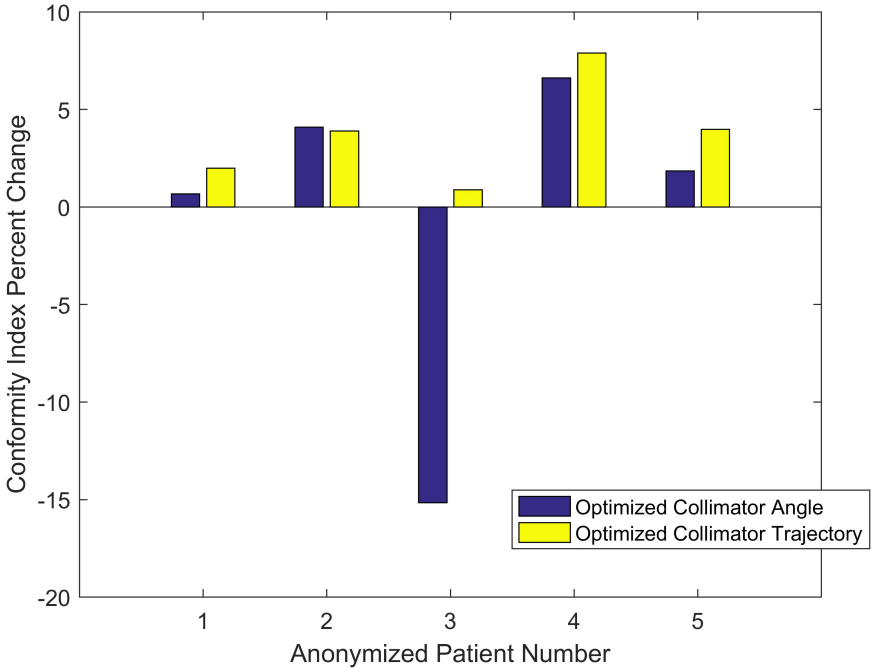

Figure 4.9: Comparison of the CI % change produced by the optimization strategies when compared with the CI of the treatment planner-selected collimator angle.

gles was most apparent after beam-weight optimization with a gradient method, and we believe this is because the gradient method was able to remove delivered dose from inefficient apertures which result from MLC contention issues.

We have shown that our current clinical hardware could safely deliver these trajectories. It is still unclear whether the modest improvement of collimator trajectory optimized treatments over static optimized collimator angle will exist in a fully-developed treatment planning optimization software. We expect that it will have a diminished importance, as we hope that the clinical software is more robust at avoiding local minima as the treatment planning system vendors have more resources to invest in perfecting whichever optimization strategy they choose to offer. Additionally, collimator trajectory delivery will put further burden on clinics in the form of extra quality assurance. Conversely, an algorithm selected static col-

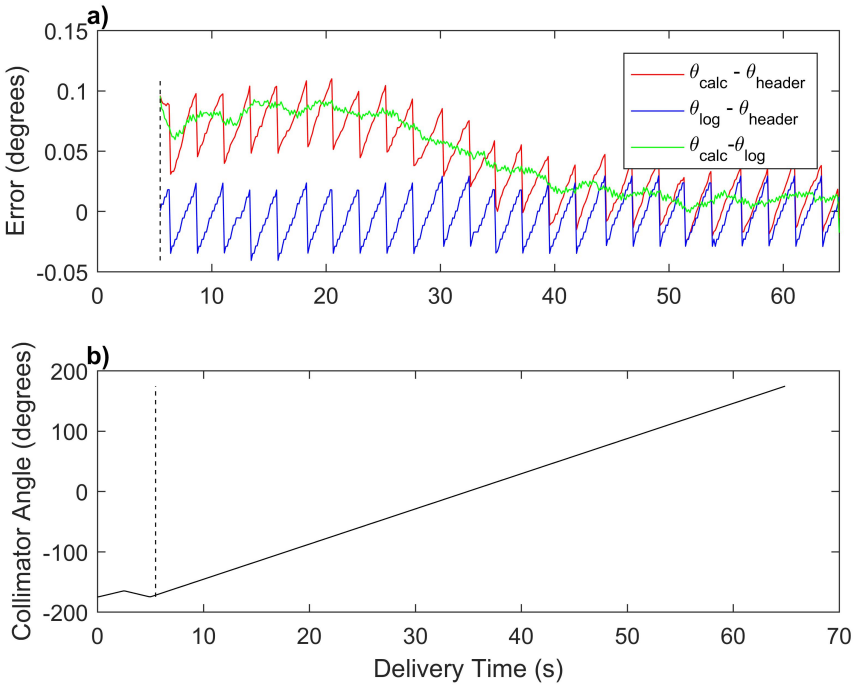

Figure 4.10: a)As the collimator rotated for its whole extent [-175 degrees, 175 degrees], the angle was measured using the EPID imager. Collimator angle was measured from three sources: the DICOM image header (θ_{header}), the trajectory log (θ_{log}), and by analysing the EPID images (θ_{calc}). b) The first 5 seconds of the QA test (to the left of the dotted line) involved a clockwise and then counterclockwise movement of the collimator to provide a unique movement to align the trajectory log and EPID images in the time axis. The remainder 60 seconds of the QA test is where the measurements were acquired.

limator angle would ease the treatment planning process, as it could be automated if properly integrated into the treatment planning system. It is unclear to us which of these two methods will best serve the needs of the radiotherapy community.

This work showed that DAO-VMAT fails to robustly approach the global minimum when the cost function contains penalties for low-dose bath to normal tissues. This weakness can be mitigated by the use of collimator angle optimization strategies. DAO-VMAT with the assistance of collimator optimization, can find

solutions that have lower dose bath when compared to human selected collimator angles. However, even with the assistance of collimator angle optimization, there were still unnecessarily opened fluences that contributed to the low-dose bath. This comes from two main sources. First, the progressive sampling algorithm fails to converge to the optimal solution when there are MLC contention issues: it produces openings that should not exist in an optimal solution. Second, the MLC has small, but non negligible radiation leakage (around 1-2% depending on MLC model). The naive solution to this problem is to separate the PTVs into groups that do not produce MLC contention issues and then treat the groups separately. However, this approach will produce an increase in the dose from radiation leakage through the MLC. Finding the optimal strategy under these considerations is complex and likely requires further investigation.

4.5 Conclusion

In this work, we showed the feasibility of dynamic collimator rotation during VMAT delivery. However, the majority of treatment improvement can be achieved using algorithm-based static collimator selection. Future work will test whether these results can be reproduced on clinical systems. The improvement made by static collimator optimization was already shown by Wu et al. [98] to improve treatment planning results on Varian Eclipse. We cannot perform a similar treatment planning system comparison of trajectory collimator optimization without access to the base code of clinical software and incorporating site-specific clinical expertise at planning with each method. Future work could compare algorithm selected collimator angle DAO-VMAT with fluence-based VMAT on clinical software.

Chapter 5

Conclusion

5.1 The Effect of Couch Rotations in SRS Deliveries

At the onset of this work, there were several gaps in knowledge on the effect of couch angle optimization on SRS deliveries. In particular, while there were studies that investigated the effect of couch angle optimization on forward planning methods such as DCA, the effect on inverse planning methods was unknown as VMAT for SRS was still in its infancy. This work found a very modest improvement on treatment quality when highly non-coplanar treatments were implemented over single arc VMAT treatments. A single VMAT arc delivers dose from a wide selection of beam directions. Multiple non-coplanar arc VMAT for SRS delivers dose from even more directions and for this reason there is a modest improvement when multiple-arc VMAT is used over single arc VMAT.

Whether trajectory optimization improves treatment plan quality depends on the optimization method being used. Many groups have created heuristic algorithms predicated on the benefit of avoiding critical OAR. These methods will improve dosimetric indices of most forward planning algorithms. However, modern linacs have the ability to completely shut off the beam using beam weight modulation and this feature can be leveraged to remove beams with less optimal direction from the beam trajectory. Furthermore, beam weight optimization is a relatively simple optimization problem as the only constraint on the system is that the beam weights remain positive. Therefore the dosimetric benefit of trajectory optimiza-

tion in forward planning methods can be reproduced by a dense sampling of the phase space during initial optimization and then using beam weight modulation to remove non-optimal beam directions. This is the basis for the methods developed in this work, as well as the methods by Langhans et al. [50] and the 4 π method [24].

There are trade offs between the optimization strategies of the work presented here and that of the heuristic couch-gantry optimization presented by other groups (e.g. the work in [59, 86, 99] as a non-exhaustive list). The theoretical analogue between the two methods is whether doses to normal tissue should be accounted for in the cost function, or as a constraint of the optimization. By avoiding certain couch-gantry angles, the optimization software of other groups is effectively forcing a hard constraint on dose from certain directions. There are a few benefits to this approach enumerated in the following paragraphs.

First, it can be difficult to represent the desires of the treatment plan in the cost function, and dose reductions may be missed because they are unknowingly left unrepresented in the optimization process. This aspect is very well illustrated in some of the clinical plans that were re-optimized in this thesis. The clinical treatment plans used a normal tissue constraint that was not configured optimally or weighted highly enough. This resulted in unnecessary over-dosage to the normal tissue. These aspects may be overcome by patient specific dose QA, termed as knowledge based planning by some groups [85]. However, these methods are not widely adopted yet, and may not catch the errors. Furthermore, these methods are enacted very close to the final delivery and are seen as a reactive (instead of a proactive) approach to quality.

Second, enforcing a hard constraint on the trajectory makes the method generalizable to any treatment optimization processes. This is important for a multitude of reasons, the most important of which is in regards to patient safety. The VMAT optimizations used in the clinic are produced by technology that is developed by vendors, and implemented by practitioners. Furthermore, these practitioners do not fully know the inner workings of the optimization software. By implementing an approach that is method-generalizable, it can be robust to changes between software upgrades, under-education of staff and changes of providers. This aspect was also well represented in the clinically delivered optimizations. The practi-

tioners that optimized the VMAT plans thought that the beam weight optimization was well accounted for in the Varian Eclipse optimizations. This functionality was enabled, and the beam weights varried only between 60% and 100% of maximal output instead of the expect 0% to 100%. This misunderstanding is not specific to our clinic, as it is not discussed in prominent publications [90].

While there is no dosimetric benefit of optimized couch-gantry trajectories over a dense sampling of the couch-gantry phase space, couch-gantry trajectory optimization can create treatments that have faster deliveries. Delivering many non-coplanar arcs can present a burden to patients and clinics. In this work, a method that variably samples the delivery phase space in a time efficient manner is presented. The dosimetric delivery quality was gauged for each phase space sampling and the sampling was increased until the delivery quality plateaued. This method ensures that deliveries leverage as many beam angles as is necessary for dosimetric performance, while being time efficient. However, this time saving benefit is modest, and with Varian's HyperArc framework of arc delivery [83], it may only amount to 1-2 minutes of treatment time saving benefit. The importance of which depends on staffing and resources of a particular centre. Other groups propose methods that deliver dose from only the most optimal angles [50], and these methods may reduce the treatment time by a further 30 seconds. However, it should be noted that for SRS deliveries, dose per fraction are high, so dose delivery rate and fluence delivery efficiency of the beam apertures set limits on the delivery time. This work did not considered FFF deliveries even though it is currently the clinical standard and will likely have the greatest effect on treatment delivery time. For SRS dose fractionation, there is no expected clinically relevant improvement on treatment time over the methods that are currently developed (either in this thesis or by other trajectory optimization groups that use inverse planning).

5.2 The Effect of Collimator-Gantry Trajectory Optimization

This work explored how collimator rotation affects VMAT deliveries by allowing more efficient MLC apertures. Efficient and robust treatment optimization is still an active area of study, and there are still many questions that need to be answered.

DAO-VMAT is particularly well suited for SRS deliveries, as targets are usually small and spherical in geometry. For these shapes, conformal treatments present an MLC sequence that is very close to the best possible treatment, as they allow as much fluence delivered as possible per beam, while naturally producing spherical dose patterns from the arc trajectory delivery. However, multiple metastases increase the complexity of this optimization, which can make DAO-VMAT not ideal for these indications. This work showed that collimator optimization can partially mitigate the shortcomings of DAO-VMAT by rotating the collimator to minimize MLC contention issues. Static collimator optimization had similar dosimetric improvement when compared to the dynamic collimator method, and this is likely due to dose rate modulation: the beam could be turned off when there were configurations that had significant contention issues.

There are other approaches which could be interesting to test in future work. In particular, fluence-based VMAT may not be hindered by the same shortfalls as DAO-VMAT. Depending on how the optimization algorithm is set up, it may be able to intelligently select which PTVs to deliver dose to when choosing between competing MLC configurations to avoid MLC contention issues. Another strategy that could be explored is delivering dose to only a subset of the PTVs when there are MLC contention issues, and then delivering dose to the untreated PTVs on a subsequent arc. This strategy is currently commercially implemented [92]. There are two short-comings to this strategy, in particular, it increases the treatment time by a factor of two. Additionally, it may not improve the treatment plan quality: if there is more leakage through the MLC than is produced by MLC contention issues, then having two arc passes would degrade the treatment quality. Future work could explore these trade-offs and identify candidate patients which would benefit from this strategy.

5.3 Delivery Capabilities of Modern Linacs

This work explored the capabilities of the Varian TrueBeam linac. In short summary, the TrueBeam linac tested in this work was found to be highly capable of moving the collimator, gantry, couch, and MLC intra-treatment with a high degree of accuracy. In this work, patient specific and machine specific measures

were developed to ensure the delivery accuracy of the linac for dynamic couch and collimator deliveries. These methods (or process-optimized versions of the same measure) would need to be integrated into linac QA procedures if dynamic delivery methods are to be implemented in the clinic. It is still an open question whether the dosimetric and delivery efficiency benefits extolled in this thesis will be offset by the clinically incurred costs of extra patient-specific and machine-specific QA.

5.4 Future Directions

There may be future work exploring the interplay between even more aspects of the treatment, such as moving the isocentre intra-treatment or exploring the interplay of couch-collimator-gantry trajectories. There is still much work to be conducted on collimator-gantry-MLC optimization for certain clinical optimization software. The Varian TrueBeam algorithm fails to robustly reduce the dose bath, and this shortfall should be rectified. It is still undetermined whether these inadequacies will exist in fluence-based optimization strategies implemented by Raystation and Pinnacle. Future work could explore this question.

This work is limited by our current understanding of the biological effect of radiation on the brain. In this work, we explored methods which would reduce the exposure of healthy brain tissue to radiation. It is important to investigate whether this is a suitable goal. Historically, there have been three strategies for the radiotherapy treatment of brain metastasis: WBRT alone, SRS alone, and SRS with adjuvant WBRT. The intention of adding adjuvant WBRT was for the prophylactic reduction of tumour burden. This reduction is measurable: results of a phase III clinical trial have shown that SRS alone had a shorter time to intra-cranial failure when compared to SRS with WBRT[13]. However, this was coupled with significant decreases in cognitive function and quality of life. Therefore, it is difficult to explore the cost-benefit of delivering radiation to healthy brain tissue. In order to find the best trade off, one would need a more in depth understanding of radiobiology.

Finally, there are many non-radiotherapy interventions which can be used to treat patients with brain metastasis. The intervention varies widely based on the primary tumour site. Future research could provide scientific support for investi-

gating radiation therapy with concurrent, adjuvant or pre-operative chemotherapy. Figuring out the effect of different interventions on radiotherapy would be an interesting question. Also, modern interventions are allowing some patients to live longer. These patients would benefit with more dose sparing for a multitude of reasons. First,low dose bath may be associated with toxicities which have not been identified due to the currently poor patient outcomes (i.e. late representing toxicities). Second, re-treatment is easier when there is a low dose bath and as patients survive longer, this re-treatment becomes more likely. Conversely, patients with short expected survival may be better suited for palliative care instead of radiotherapy. Demarcating these treatment groups would greatly advance the quality of care and decrease resource usage.

Bibliography

[1] *TrueBeam Developer Mode User's Manual*. → page 42

[2] A. Agnew, C. Agnew, M. Grattan, A. Hounsell, and C. McGarry. Monitoring daily mlc positional errors using trajectory log files and epid measurements for imrt and vmat deliveries. *Physics in medicine and biology*, 59(9):N49, 2014. → pages 71, 85

[3] P. R. Almond, P. J. Biggs, B. M. Coursey, W. Hanson, M. S. Huq, R. Nath, and D. Rogers. Aapm's tg-51 protocol for clinical reference dosimetry of high-energy photon and electron beams. *Medical physics*, 26(9): 1847–1870, 1999. → page 2

[4] H. Aoyama, H. Shirato, M. Tago, K. Nakagawa, T. Toyoda, K. Hatano, M. Kenjyo, N. Oya, S. Hirota, H. Shioura, et al. Stereotactic radiosurgery plus whole-brain radiation therapy vs stereotactic radiosurgery alone for treatment of brain metastases: a randomized controlled trial. *Jama*, 295 (21):2483–2491, 2006. → page 1

[5] L. Armijo. Minimization of functions having lipschitz continuous first partial derivatives. *Pacific Journal of mathematics*, 16(1):1–3, 1966. → page 30

[6] J. Bayouth, D. Wendt, and S. Morrill. Mlc quality assurance techniques for imrt applications. *Medical physics*, 30(5):743–750, 2003. → page 24

[7] J. L. Bedford. Treatment planning for volumetric modulated arc therapy. *Medical physics*, 36(11):5128–5138, 2009. → page 38

[8] S. M. Bentzen and V. Gregoire. Molecular imaging–based dose painting: A novel paradigm for radiation therapy prescription. In *Seminars in radiation oncology*, volume 21, pages 101–110. Elsevier, 2011. → pages 18, 36

[9] S. M. Bentzen, L. S. Constine, J. O. Deasy, A. Eisbruch, A. Jackson, L. B. Marks, R. K. Ten Haken, and E. D. Yorke. Quantitative analyses of normal tissue effects in the clinic (quantec): an introduction to the scientific issues. *International Journal of Radiation Oncology* Biology* Physics*, 76(3): S3–S9, 2010. → pages xi, 16, 57, 90

[10] M. Berger, J. Hubbell, S. Seltzer, J. Chang, J. Coursey, R. Sukumar, D. Zucker, and K. Olsen. Nist standard reference database 8 (xgam). *XCOM: Photon Cross Sections Database*, 2008. → pages xiii, 4

[11] T. Bortfeld. Optimized planning using physical objectives and constraints. In *Seminars in Radiation Oncology*, volume 9, pages 20–34. Elsevier, 1999. → page 36

[12] T. Bortfeld, W. Schlegel, and B. Rhein. Decomposition of pencil beam kernels for fast dose calculations in three-dimensional treatment planning. *Medical physics*, 20(2):311–318, 1993. → page 14

[13] P. D. Brown, K. Jaeckle, K. V. Ballman, E. Farace, J. H. Cerhan, S. K. Anderson, X. W. Carrero, F. G. Barker, R. Deming, S. H. Burri, et al. Effect of radiosurgery alone vs radiosurgery with whole brain radiation therapy on cognitive function in patients with 1 to 3 brain metastases: a randomized clinical trial. *Jama*, 316(4):401–409, 2016. → pages 88, 111

[14] K. Bzdusek, H. Friberger, K. Eriksson, B. Hårdemark, D. Robinson, and M. Kaus. Development and evaluation of an efficient approach to volumetric arc therapy planning. *Medical physics*, 36(6Part1):2328–2339, 2009. → page 38

[15] X. Y. Cedric and G. Tang. Intensity-modulated arc therapy: principles, technologies and clinical implementation. *Physics in Medicine & Biology*, 56(5):R31, 2011. → page 37

[16] G. M. Clark, R. A. Popple, P. E. Young, and J. B. Fiveash. Feasibility of single-isocenter volumetric modulated arc radiosurgery for treatment of multiple brain metastases. *International Journal of Radiation Oncology Biology Physics*, 76(1):296–302, 2010. → pages 41, 45, 70

[17] G. M. Clark, R. A. Popple, B. M. Prendergast, S. A. Spencer, E. M. Thomas, J. G. Stewart, B. L. Guthrie, J. M. Markert, and J. B. Fiveash. Plan quality and treatment planning technique for single isocenter cranial radiosurgery with volumetric modulated arc therapy. *Practical radiation oncology*, 2(4):306–313, 2012. → page 70

[18] I. E. Commission et al. Iec 61217 radiotherapy equipmentco-ordinates, movements and scales. *International Electrotechnical Commission*, 2011. → page 49

[19] A. R. T. Committee, A. Boyer, et al. *Basic applications of multileaf collimators*. American Association of Physicists in Medicine Madison, 2001. → page 8

[20] A. H. Compton. A quantum theory of the scattering of x-rays by light elements. *Physical review*, 21(5):483, 1923. → page 2

[21] J. Croker, B. Chua, A. Bernard, M. Allon, and M. Foote. Treatment of brain oligometastases with hypofractionated stereotactic radiotherapy utilising volumetric modulated arc therapy. *Clinical & experimental metastasis*, pages 1–8, 2015. → page 47

[22] T. Depuydt, A. Van Esch, and D. P. Huyskens. A quantitative evaluation of imrt dose distributions: refinement and clinical assessment of the gamma evaluation. *Radiotherapy and oncology*, 62(3):309–319, 2002. → page 94

[23] T. Depuydt, R. Penne, D. Verellen, J. Hrbacek, S. Lang, K. Leysen, I. Vandevondel, K. Poels, T. Reynders, T. Gevaert, M. Duchateau, K. Tournel, M. Boussaer, D. Cosentino, C. Garibaldi, T. Solberg, and M. D. Ridder. Computer-aided analysis of star shot films for high-accuracy radiation therapy treatment units. *Physics in Medicine and Biology*, 57(10): 2997, 2012. URL http://stacks.iop.org/0031-9155/57/i=10/a=2997. → pages 71, 77

[24] P. Dong, T. Long, D. Ruan, P. Lee, D. Romeijn, D. Low, P. Kupelian, and K. Sheng. 4pi radiation therapy for liver sbrt. *International Journal of Radiation Oncology* Biology* Physics*, 84(3):S202, 2012. → page 108

[25] A. Edwards, E. Keggin, and P. Plowman. The developing role for intensity-modulated radiation therapy (imrt) in the non-surgical treatment of brain metastases. *The British journal of radiology*, 83(986):133–136, 2010. → page 19

[26] B. Fahimian, V. Yu, K. Horst, L. Xing, and D. Hristov. Trajectory modulated prone breast irradiation: A linac-based technique combining intensity modulated delivery and motion of the couch. *Radiotherapy and Oncology*, 109(3):475–481, 2013. → page 70

[27] G. B. Fogarty, A. Hong, V. Gondi, B. Burmeister, K. Jacobsen, S. Lo, E. Paton, B. Shivalingam, and J. F. Thompson. Debate: adjuvant whole brain radiotherapy or not? more data is the wiser choice. *BMC cancer*, 16 (1):372, 2016. → page 90

[28] P. Francescon, S. Cora, and C. Cavedon. Total scatter factors of small beams: a multidetector and monte carlo study. *Medical physics*, 35(2): 504–513, 2008. → page 20

[29] M. Fuss, E. Sturtewagen, C. De Wagter, and D. Georg. Dosimetric characterization of gafchromic ebt film and its implication on film dosimetry quality assurance. *Physics in Medicine & Biology*, 52(14):4211, 2007. → page 21

[30] E. Gete, B. Wilson, and R. Lee. Su-e-t-53: A new method for characterizing the stability of the treatment couch isocentre. *Medical Physics*, 42(6), 2015. → page 56

[31] A. Gonzlez, I. Castro, and J. A. Martinez. A procedure to determine the radiation isocenter size in a linear accelerator. *Medical Physics*, 31(6), 2004. → page 71

[32] R. T. O. Group et al. Rtog/eortc late radiation morbidity scoring schema, 1999. → page 15

[33] X. Gu, U. Jelen, J. Li, X. Jia, and S. B. Jiang. A gpu-based finite-size pencil beam algorithm with 3d-density correction for radiotherapy dose calculation. *Physics in Medicine & Biology*, 56(11):3337, 2011. → page 14

[34] D. Hanahan and R. A. Weinberg. The hallmarks of cancer. *cell*, 100(1): 57–70, 2000. → page 2

[35] D. Hanahan and R. A. Weinberg. Hallmarks of cancer: the next generation. *cell*, 144(5):646–674, 2011. → page 2

[36] N. Hodapp. The icru report 83: prescribing, recording and reporting photon-beam intensity-modulated radiation therapy (imrt). *Strahlentherapie und Onkologie: Organ der Deutschen Rontgengesellschaft...[et al]*, 188(1):97–99, 2012. → page 36

[37] F. Hsu, H. Carolan, A. Nichol, F. Cao, N. Nuraney, R. Lee, E. Gete, F. Wong, M. Schmuland, M. Heran, et al. Whole brain radiotherapy with hippocampal avoidance and simultaneous integrated boost for 1–3 brain

metastases: a feasibility study using volumetric modulated arc therapy. *International Journal of Radiation Oncology Biology Physics*, 76(5): 1480–1485, 2010. → pages 41, 45

[38] Y. Huang, K. Chin, J. R. Robbins, J. Kim, H. Li, H. Amro, I. J. Chetty, J. Gordon, and S. Ryu. Radiosurgery of multiple brain metastases with single-isocenter dynamic conformal arcs (sidca). *Radiotherapy and Oncology*, 112(1):128–132, 2014. → page 70

[39] M. S. Huq, B. A. Fraass, P. B. Dunscombe, J. P. Gibbons, G. S. Ibbott, A. J. Mundt, S. Mutic, J. R. Palta, F. Rath, B. R. Thomadsen, et al. The report of task group 100 of the aapm: Application of risk analysis methods to radiation therapy quality management. *Medical physics*, 43(7):4209–4262, 2016. → page 23

[40] Y. Iwai, S. Ozawa, T. Ageishi, R. Pellegrini, and K. Yoda. Feasibility of single-isocenter, multi-arc non-coplanar volumetric modulated arc therapy for multiple brain tumors using a linear accelerator with a 160-leaf multileaf collimator: a phantom study. *Journal of radiation research*, page rru042, 2014. → page 70

[41] D. Jones. Icru report 50prescribing, recording and reporting photon beam therapy. *Medical physics*, 21(6):833–834, 1994. → pages 14, 36

[42] G. Kalantzis and A. Apte. A novel reduced-order prioritized optimization method for radiation therapy treatment planning. *Biomedical Engineering, IEEE Transactions on*, 61(4):1062–1070, 2014. → page 53

[43] J. Kao, B. Darakchiev, L. Conboy, S. Ogurek, N. Sharma, X. Ren, and J. Pettit. Tumor directed, scalp sparing intensity modulated whole brain radiotherapy for brain metastases. *Technology in cancer research & treatment*, 14(5):547–555, 2015. → page 47

[44] T. Kataria, K. Sharma, V. Subramani, K. Karrthick, and S. S. Bisht. Homogeneity index: An objective tool for assessment of conformal radiation treatments. *Journal of medical physics/Association of Medical Physicists of India*, 37(4):207, 2012. → page 17

[45] J. P. Kirkpatrick, Z. Wang, J. H. Sampson, F. McSherry, J. E. Herndon, K. J. Allen, E. Duffy, J. K. Hoang, Z. Chang, D. S. Yoo, et al. Defining the optimal planning target volume in image-guided stereotactic radiosurgery of brain metastases: results of a randomized trial. *International Journal of Radiation Oncology* Biology* Physics*, 91(1):100–108, 2015. → page 14

[46] S. Kirkpatrick, C. D. Gelatt, and M. P. Vecchi. Optimization by simulated annealing. *science*, 220(4598):671–680, 1983. → page 32

[47] E. E. Klein, J. Hanley, J. Bayouth, F.-F. Yin, W. Simon, S. Dresser, C. Serago, F. Aguirre, L. Ma, B. Arjomandy, C. Liu, C. Sandin, and T. Holmes. Task group 142 report: Quality assurance of medical acceleratorsa). *Medical Physics*, 36(9):11, 2009. doi:http://dx.doi.org/10.1118/1.3190392. URL http://scitation.aip.org/content/aapm/journal/medphys/36/9/10.1118/1.3190392. → page 70

[48] E. E. Klein, J. Hanley, J. Bayouth, F.-F. Yin, W. Simon, S. Dresser, C. Serago, F. Aguirre, L. Ma, B. Arjomandy, et al. Task group 142 report: quality assurance of medical accelerators. *Medical physics*, 36(9Part1): 4197–4212, 2009. → pages xi, 24, 25

[49] O. Klein and Y. Nishina. Über die streuung von strahlung durch freie elektronen nach der neuen relativistischen quantendynamik von dirac. *Zeitschrift für Physik*, 52(11-12):853–868, 1929. → page 5

[50] M. Langhans, J. Unkelbach, T. Bortfeld, and D. Craft. Optimizing highly noncoplanar vmat trajectories: the novo method. *Physics in Medicine & Biology*, 63(2):025023, 2018. → pages 43, 108, 109

[51] S. K. Lau, K. Zakeri, X. Zhao, R. Carmona, E. Knipprath, D. R. Simpson, S. K. Nath, G.-Y. Kim, P. Sanghvi, J. A. Hattangadi-Gluth, et al. Single-isocenter frameless volumetric modulated arc radiosurgery for multiple intracranial metastases. *Neurosurgery*, 77(2):233–240, 2015. → page 41

[52] D. Lewis, A. Micke, and X. Yu. New performance standard: Multi-channel and one-scan radiochromic film dosimetry, 2012. → page 21

[53] J. Liang, T. Atwood, R. von Eyben, B. Fahimian, E. Chin, K. Horst, K. Otto, and D. Hristov. Trajectory modulated arc therapy: A fully dynamic delivery with synchronized couch and gantry motion significantly improves dosimetric indices correlated with poor cosmesis in accelerated partial breast irradiation. *International Journal of Radiation Oncology* Biology* Physics*, 92(5):1148–1156, 2015. → pages 42, 85, 86

[54] C. C. Ling, P. Zhang, Y. Archambault, J. Bocanek, G. Tang, and T. LoSasso. Commissioning and quality assurance of rapidarc radiotherapy delivery system. *International Journal of Radiation Oncology Biology Physics*, 72(2):575–581, 2008. → page 24

[55] C. B. Locke and K. K. Bush. Trajectory optimization in radiotherapy using sectioning (torus). *Medical Physics*, 2017. → pages 44, 88, 91

[56] D. A. Low, W. B. Harms, S. Mutic, and J. A. Purdy. A technique for the quantitative evaluation of dose distributions. *Medical Physics*, 25(5), 1998. → page 56

[57] D. A. Low, W. B. Harms, S. Mutic, and J. A. Purdy. A technique for the quantitative evaluation of dose distributions. *Medical physics*, 25(5): 656–661, 1998. → page 27

[58] W. Lutz, K. R. Winston, and N. Maleki. A system for stereotactic radiosurgery with a linear accelerator. *International Journal of Radiation Oncology* Biology* Physics*, 14(2):373–381, 1988. → pages 26, 40, 47, 71

[59] R. L. MacDonald and C. G. Thomas. Dynamic trajectory-based couch motion for improvement of radiation therapy trajectories in cranial srt. *Medical physics*, 42(5):2317–2325, 2015. → pages 42, 48, 70, 85, 86, 108

[60] R. L. MacDonald, C. G. Thomas, and A. Syme. Dynamic collimator trajectory algorithm for multiple metastases dynamic conformal arc treatment planning. *Medical physics*, 2018. → pages 45, 88

[61] L. B. Marks, E. D. Yorke, A. Jackson, R. K. Ten Haken, L. S. Constine, A. Eisbruch, S. M. Bentzen, J. Nam, and J. O. Deasy. Use of normal tissue complication probability models in the clinic. *International Journal of Radiation Oncology* Biology* Physics*, 76(3):S10–S19, 2010. → page 16

[62] P. M. McCowan, D. W. Rickey, P. Rowshanfarzad, P. B. Greer, W. Ansbacher, and B. M. McCurdy. An investigation of gantry angle data accuracy for cine-mode epid images acquired during arc imrt. *Journal of applied clinical medical physics*, 15(1), 2014. → page 85

[63] C. McIntosh, M. Welch, A. McNiven, D. A. Jaffray, and T. G. Purdie. Fully automated treatment planning for head and neck radiotherapy using a voxel-based dose prediction and dose mimicking method. *Physics in Medicine & Biology*, 62(15):5926, 2017. → page 35

[64] V. Medical. Truebeam stx system: Specification. Technical report, Varian Medical Systems, 08 2008. → page 10

[65] M.-P. Milette and K. Otto. Maximizing the potential of direct aperture optimization through collimator rotation. *Medical physics*, 34(4): 1431–1438, 2007. → page 44

[66] E. Mladenov, S. Magin, A. Soni, and G. Iliakis. Dna double-strand break repair as determinant of cellular radiosensitivity to killing and target in radiation therapy. *Frontiers in oncology*, 3:113, 2013. → page 2

[67] S. Morgan-Fletcher. Prescribing, recording and reporting photon beam therapy (supplement to icru report 50), icru report 62, 2001. → page 14

[68] D. Nguyen, J.-C. M. Rwigema, Y. Y. Victoria, T. Kaprealian, P. Kupelian, M. Selch, P. Lee, D. A. Low, and K. Sheng. Feasibility of extreme dose escalation for glioblastoma multiforme using 4π radiotherapy. *Radiation Oncology*, 9(1):1, 2014. → page 42

[69] A. Nichol, R. Ma, F. Hsu, L. Gondara, H. Carolan, R. Olson, D. Schellenberg, F. Germain, A. Cheung, M. Peacock, et al. Volumetric radiosurgery for 1 to 10 brain metastases: A multicenter, single-arm, phase 2 study. *International Journal of Radiation Oncology* Biology* Physics*, 94(2):312–321, 2016. → pages 68, 70

[70] N. I. of Standardards and Technology. Xcom: Photon cross section database, 2009. URL https://www.nist.gov/pml/xcom-photon-cross-sections-database. → pages xiii, 4

[71] K. Otto. Volumetric modulated arc therapy: Imrt in a single gantry arc. *Medical physics*, 35(1):310–317, 2008. → pages xvi, 38, 39, 51, 88, 92

[72] K. Otto and B. G. Clark. Enhancement of imrt delivery through mlc rotation. *Physics in Medicine & Biology*, 47(22):3997, 2002. → page 44

[73] I. Paddick. A simple scoring ratio to index the conformity of radiosurgical treatment plans: technical note. *Journal of neurosurgery*, 93(Supplement 3):219–222, 2000. → pages 17, 52

[74] I. Paddick and B. Lippitz. A simple dose gradient measurement tool to complement the conformity index. *Special Supplements*, 105(7):194–201, 2006. → page 53

[75] E. B. Podgorsak, A. Olivier, M. Pla, P.-Y. Lefebvre, and J. Hazel. Dynamic stereotactic radiosurgery. *International Journal of Radiation Oncology* Biology* Physics*, 14(1):115–126, 1988. → pages 42, 48, 52, 61, 62

[76] C. C. Popescu, W. A. Beckham, V. V. Patenaude, I. A. Olivotto, and M. T. Vlachaki. Simultaneous couch and gantry dynamic arc rotation (cg-darc) in

the treatment of breast cancer with accelerated partial breast irradiation (apbi): a feasibility study. *Journal of Applied Clinical Medical Physics*, 14 (1), 2013. → pages 70, 85, 86

[77] J. Posner. Management of brain metastases. *Revue neurologique*, 148(6-7): 477–487, 1992. → page 1

[78] E. M. Quan, X. Li, Y. Li, X. Wang, R. J. Kudchadker, J. L. Johnson, D. A. Kuban, A. K. Lee, and X. Zhang. A comprehensive comparison of imrt and vmat plan quality for prostate cancer treatment. *International Journal of Radiation Oncology Biology Physics*, 83(4):1169–1178, 2012. → page 88

[79] N. Ramakrishna, F. Rosca, S. Friesen, E. Tezcanli, P. Zygmanszki, and F. Hacker. A clinical comparison of patient setup and intra-fraction motion using frame-based radiosurgery versus a frameless image-guided radiosurgery system for intracranial lesions. *Radiotherapy and Oncology*, 95(1):109–115, 2010. → page 22

[80] D. Rogers, B. Faddegon, G. Ding, C.-M. Ma, J. We, and T. Mackie. Beam: a monte carlo code to simulate radiotherapy treatment units. *Medical physics*, 22(5):503–524, 1995. → page 11

[81] J. Roper, V. Chanyavanich, G. Betzel, J. Switchenko, and A. Dhabaan. Single-isocenter multiple-target stereotactic radiosurgery: Risk of compromised coverage. *International Journal of Radiation Oncology* Biology* Physics*, 93(3):540–546, 2015. → pages 68, 86

[82] P. Rowshanfarzad, M. Sabet, D. J. O Connor, and P. B. Greer. Verification of the linac isocenter for stereotactic radiosurgery using cine-epid imaging and arc delivery. *Medical Physics*, 38(7), 2011. → page 27

[83] R. Ruggieri, S. Naccarato, R. Mazzola, F. Ricchetti, S. Corradini, A. Fiorentino, and F. Alongi. Linac-based vmat radiosurgery for multiple brain lesions: comparison between a conventional multi-isocenter approach and a new dedicated mono-isocenter technique. *Radiation Oncology*, 13 (1):38, 2018. → page 109

[84] S. F. Shaitelman, L. H. Kim, D. Yan, A. A. Martinez, F. A. Vicini, and I. S. Grills. Continuous arc rotation of the couch therapy for the delivery of accelerated partial breast irradiation: a treatment planning analysis. *International Journal of Radiation Oncology* Biology* Physics*, 80(3): 771–778, 2011. → page 42

[85] S. Shiraishi, J. Tan, L. A. Olsen, and K. L. Moore. Knowledge-based prediction of plan quality metrics in intracranial stereotactic radiosurgery. *Medical physics*, 42(2):908–917, 2015. → page 108

[86] G. Smyth, J. C. Bamber, P. M. Evans, and J. L. Bedford. Trajectory optimization for dynamic couch rotation during volumetric modulated arc radiotherapy. *Physics in medicine and biology*, 58(22):8163, 2013. → pages 42, 48, 70, 85, 86, 108

[87] T. D. Solberg, K. L. Boedeker, R. Fogg, M. T. Selch, and A. A. DeSalles. Dynamic arc radiosurgery field shaping: a comparison with static field conformal and noncoplanar circular arcs. *International Journal of Radiation Oncology Biology Physics*, 49(5):1481–1491, 2001. → pages 19, 41, 47

[88] B. Sun, D. Rangaraj, G. Palaniswaamy, S. Yaddanapudi, O. Wooten, D. Yang, S. Mutic, and L. Santanam. Initial experience with truebeam trajectory log files for radiation therapy delivery verification. *Practical radiation oncology*, 3(4):e199–e208, 2013. → page 71

[89] E. M. Thomas, R. A. Popple, X. Wu, G. M. Clark, J. M. Markert, B. L. Guthrie, Y. Yuan, M. C. Dobelbower, S. A. Spencer, and J. B. Fiveash. Comparison of plan quality and delivery time between volumetric arc therapy (rapidarc) and gamma knife radiosurgery for multiple cranial metastases. *Neurosurgery*, 75(4):40917; discussion 4178, October 2014. ISSN 0148-396X. doi:10.1227/neu.0000000000000448. URL http://europepmc.org/articles/PMC4203364. → page 70

[90] E. M. Thomas, R. A. Popple, X. Wu, G. M. Clark, J. M. Markert, B. L. Guthrie, Y. Yuan, M. C. Dobelbower, S. A. Spencer, and J. B. Fiveash. Comparison of plan quality and delivery time between volumetric arc therapy (rapidarc) and gamma knife radiosurgery for multiple cranial metastases. *Neurosurgery*, 75(4):409–17, 2014. → pages 19, 41, 47, 54, 109

[91] D. I. Thwaites and J. B. Tuohy. Back to the future: the history and development of the clinical linear accelerator. *Physics in Medicine & Biology*, 51(13):R343, 2006. → page 6

[92] E. Verrecchia, M. Chea, K. Cristina, A. Halley, E. Clausse, M. Cuttat, and C. Jenny. 16. single isocenter dynamic conformationnal arctherapy of multiple brain metastases: Treatment planning and dosimetric comparison

with the gammaknife. *Physica Medica: European Journal of Medical Physics*, 44:8–9, 2017. → page 110

[93] Y. Y. Victoria, B. P. Fahimian, L. Xing, and D. H. Hristov. Quality control procedures for dynamic treatment delivery techniques involving couch motion. *Medical physics*, 41(8):081712, 2014. → pages 42, 43

[94] S. Webb. Does the option to rotate the elekta beam modulator mlc during vmat imrt delivery confer advantage?a study of parked gaps. *Physics in Medicine & Biology*, 55(11):N303, 2010. → page 44

[95] B. Wilson, T. Teke, C. Duzenli, and E. Gete. Scisat am: Stereo05: The development of quality assurance methods for trajectory based cranial srs treatments. *Medical Physics*, 41(8):29–29, 2014. → page 42

[96] B. Wilson, K. Otto, and E. Gete. A simple and robust trajectory-based stereotactic radiosurgery treatment. *Medical Physics*, 44(1):240–248, 2017. ISSN 2473-4209. doi:10.1002/mp.12036. URL http://dx.doi.org/10.1002/mp.12036. → pages 70, 85

[97] Q. Wu and R. Mohan. Multiple local minima in imrt optimization based on dose–volume criteria. *Medical physics*, 29(7):1514–1527, 2002. → page 37

[98] Q. Wu, K. C. Snyder, C. Liu, Y. Huang, B. Zhao, I. J. Chetty, and N. Wen. Optimization of treatment geometry to reduce normal brain dose in radiosurgery of multiple brain metastases with single–isocenter volumetric modulated arc therapy. *Scientific reports*, 6:34511, 2016. → pages 45, 46, 88, 92, 103, 106

[99] Y. Yang, P. Zhang, L. Happersett, J. Xiong, J. Yang, M. Chan, K. Beal, G. Mageras, and M. Hunt. Choreographing couch and collimator in volumetric modulated arc therapy. *International Journal of Radiation Oncology* Biology* Physics*, 80(4):1238–1247, 2011. → pages 42, 44, 48, 70, 85, 86, 108

[100] C. X. Yu. Intensity-modulated arc therapy with dynamic multileaf collimation: an alternative to tomotherapy. *Physics in Medicine & Biology*, 40(9):1435, 1995. → page 37

[101] V. Y. Yu, B. P. Fahimian, L. Xing, and D. H. Hristov. Quality control procedures for dynamic treatment delivery techniques involving couch motion. *Medical Physics*, 41(8):081712, 2014. doi:http://dx.doi.org/10.1118/1.4886757. URL http://scitation.aip.org/content/aapm/journal/medphys/41/8/10.1118/1.4886757. → pages 24, 56

[102] P. Zhang, L. Happersett, Y. Yang, Y. Yamada, G. Mageras, and M. Hunt. Optimization of collimator trajectory in volumetric modulated arc therapy: development and evaluation for paraspinal sbrt. *International Journal of Radiation Oncology Biology Physics*, 77(2):591–599, 2010. → pages 42, 44